Alma Mater Studiorum · University of Bologna

School of Science
Department of Physics and Astronomy
Master Degree in Physics

Experimental study of the antideuteron source in p-p collisions at LHC energies.

Supervisor:
Prof. Francesca Bellini

Submitted by:
Sofia Tomassini

Academic Year 2022/2023

Abstract

This thesis presents a first analysis of the correlation function for (anti)proton and (anti)deuteron based on a sample of pp collisions data collected in 2022 at $\sqrt{s} = 13.6$ TeV by the ALICE experiment at CERN. The study of momentum correlations among particles is employed in constraining light antinuclei formation mechanisms and validating models of coalescence of antinucleons into light antinuclei. This is motivated by the fact that a deeper understanding of the origin of cosmic light antinuclei opens the possibility of searching for them as indirect dark matter signals, having the capability to predict the expected signal and background rates.

In this work, the femtoscopy technique is applied to measure the correlation functions for proton−proton (p−p) and proton−deuteron (p−d) pairs. The obtained p−p correlation is fitted with the Argonne ν_{18} plus the Coulomb potentials to extract a preliminary measurement of the proton source radius in minimum bias pp collisions, resulting equal to $r_0 = 1.069 \pm 0.014$ fm. The obtained p−d correlation function is discussed in comparison with the measurement in pp collisions at $\sqrt{s} = 13$ TeV. The analysis is based on a new framework developed to meet the goals of this thesis. The optimization of the particle identification selection criteria and the pair-building procedure is achieved in this work. The promising result motivates the extensions of the analysis to the complete pp dataset available from the ongoing LHC Run 3.

Contents

Introduction

For almost a century, astronomers have made compelling observations demonstrating that the visible and baryonic matter that we can describe with the Standard Model of particle physics is only the 5% of the Universe. The remaining significant portion of the Universe is made of non-visible and non-baryonic matter, called dark matter, and a still unknown energy component called dark energy. Among various theory hypotheses, a new class of particles called Weakly Interacting Massive Particles has been proposed to match the dark matter properties, which is expected to annihilate producing Standard Model particles, as lepton-antilepton or hadron-antihadron pairs. These final states are the subject of indirect searches with space-based particle detectors, like AMS-02, for which a major challenge is the estimate of the astrophysical background due to the cosmic ray flux. Cosmic light antinuclei, like antideuteron and antihelium-3, have been proposed as dark matter smoking guns, because they can be produced from WIMPs annihilation, and their signal is expected to be almost background-free at low energy. On the other hand, hadronic collisions of primary cosmic rays with the interstellar medium, mainly composed of protons and helium, could also produce light antinuclei that would constitute the main background sources for antinuclei from dark matter.
To predict the expected signal and background rates for cosmic antinuclei, models of coalescence are typically employed to describe the fusion of antinucleons into light antinuclei due to the binding strong interaction. Despite having been employed for many years already, only recently it has been pointed out that colaescence models can be constrained by studying momentum correlations among particle pairs with dedicated measurements in controlled conditions at particle accelerators. At the Large Hadron Collider (LHC) at CERN, protons collide at a centre-of-mass energy of 0.9 to 13.6 TeV, producing rare light antinuclei, among other particles. The availability of large samples of proton-proton collision data offers an important opportunity to investigate their production mechanism also by measuring momentum correlations among particle pairs involving protons and light nuclei.

This thesis presents an experimental study of proton−proton and proton−deuteron momentum correlations, using data from proton-proton (pp) collisions collected by A Large Ion Collider Experiment (ALICE) in 2022. Among the experiments at the LHC, the ALICE detector is uniquely equipped to measure low momentum particles and light

antinuclei due to its tracking and particle identification capabilities.
A technique called femtoscopy is used to measure the correlation function and access spatial information about the nucleon emitting region, called the source. In particular, the goal is to measure the source radius. This parameter enters directly in coalescence models because the coalescence probability explicitly depends on it.

The analysis requires the identification of a pure sample of protons and deuterons that are subsequently coupled in pairs to compute the experimental correlation function from the pair distribution in relative momentum. To this end, I developed a new analysis software inside the official analysis framework for ALICE that optimizes the particle identification for protons and deuterons.

The thesis is organized into five chapters. In the first chapter, the physical motivations for this study are discussed, and antinuclei are introduced as promising dark matter signals. Coalescence models are explained in this context, also motivating the connection with femtoscopy: the study of particle correlations gives access to information about the interaction among the particles of interest and can be used to validate models of the nucleon-nucleon strong potential. These latter as well as, the strong interaction and quantum chromodynamics (QCD) are introduced in the second chapter.
After describing the femtoscopy technique and the ALICE experiment briefly in chapters three and four, the last chapter is dedicated to the analysis of the proton−proton and proton−deuteron correlations measured in pp collisions at $\sqrt{s} = 13.6$ TeV with ALICE, and to the discussion of the results of this thesis, which set the bases for the analysis with the full LHC Run 3 dataset.

Chapter 1

Cosmic antinuclei

The study of cosmic radiation has always been challenging since its discovery, continuously opening new fronts in high-energy physics. The first positron, observed in cosmic rays by Anderson in 1932, was the first antimatter particle to ever been discovered and the first experimental proof of Dirac's theory. Since then, cosmic rays have been investigated as probes of new physical events. In 1955, the antiproton was observed at Bevatron at the Lawrence Berkeley National Laboratory, and the antineutron was later discovered. At that point is seemed natural to expect that antiprotons antineutrons could bound into antinuclei, as protons and neutrons do in matter. The strong nuclear interaction between nucleons and antinucleons is assumed to be the same by the CPT invariance, which has been experimentally confirmed with high precision in the sector of light nuclei [1]. The first observation of an antinucleus was in 1965, with the discovery of the first antideuteron, a bound state of an antiproton and an antineutron. Light antinuclei are searched for in cosmic rays as rare events but are still not observed. Their origin and their formation mechanisms are not yet fully understood but, according to cosmic ray models of formation, light antinuclei can be produced in hadronic collisions between primary cosmic rays, mainly composed of protons, with the interstellar medium, mainly composed of hydrogen (thus protons) and helium. However, the possibility of having primary light antinuclei is also explored, stemming from the hypothesis that they could be signals of dark matter. In order to detect light antinuclei such as antideuteron and antihelium and identify them as dark matter signals, it is necessary to know the expected flux for the background produced by cosmic rays.

1.1 Dark matter

Dark matter is a yet unknown component of the universe. It constitutes almost the 80% of the whole matter, and is distinguished from the ordinary matter described by the standard model of particle physics because it does not emit or couple with electro-

magnetic radiation.
The existence of dark matter was postulated by Fritz Zwicky in 1933, to explain the velocity dispersion of galaxies in the Coma cluster, also considering Doppler shifts in galactic spectra [2, 3].
Nowadays, the existence of this invisible matter is supported by many strong proofs, including astronomical observations and cosmological studies [4, 5].
Among many astronomical proofs of dark matter existence is the observation of anomalies in the rotational velocity curve of spiral galaxies that, instead of decreasing as $1/r$, where r is the distance from the galactic center, is flat. This behavior can be explained assuming that the galaxy is immersed in a dark matter halo [6].
Among all the astronomical observations, the so-called Bullet Cluster represents the strongest one. The Bullet Cluster, in figure 1.1, results from a collision between a subcluster and the larger galaxy cluster 1E 0657-56. A galaxy cluster is composed of galaxies (for 2%) and mainly of hot gas (for 5-15%). During the collision, the galaxies pass by each other without interacting, while the gas is compressed and shock-heated, emitting a huge amount of X-ray radiation. The location of this radiation (pink regions in figure 1.1) indicates the majority of the radiating mass distribution in the cluster, while the mapping of gravitational lensing [7] gives information about the location of the majority of the cluster's total mass (blue regions in figure 1.1). In the Bullet Cluster, we can see that most of mass is weakly interacting and non-radiating, consistent with the presence of dark matter [8].

The presence of dark matter is not just a hypothetical solution to the problem of missing matter, but it is a necessary element for the Big Bang theory and to prove the accuracy of the most solid cosmological model ΛCDM, where Λ is the cosmological constant representing the dark energy, and CDM stays for Cold (*i.e.* non-relativistic) Dark Matter.

If dark matter is composed of particle (or has a particle nature) the most probable hypothesis is that it is composed of particles that do not belong to the standard model of particle physics, electrical and color neutral, stable, and massive. Since none of the known particles can satisfy all the requirements simultaneously, a new class of particles, the Weakly Interacting Massive Particles (WIMPs), has been theorized to be a possible dark matter candidates. Because of the peculiar proprieties of the WIMPs, one of the most challenging problems in physics is their detection, to prove the microscopic origin of dark matter and validate the WIMP hypothesis.

1.1.1 Indirect detection of dark matter

Dark matter detection is one of the main challenges in experimental physics and is carried on following three main approaches, as represented in figure 1.2: production, direct and indirect detection.

Dark matter production can take place in high-energy collisions between baryonic mat-

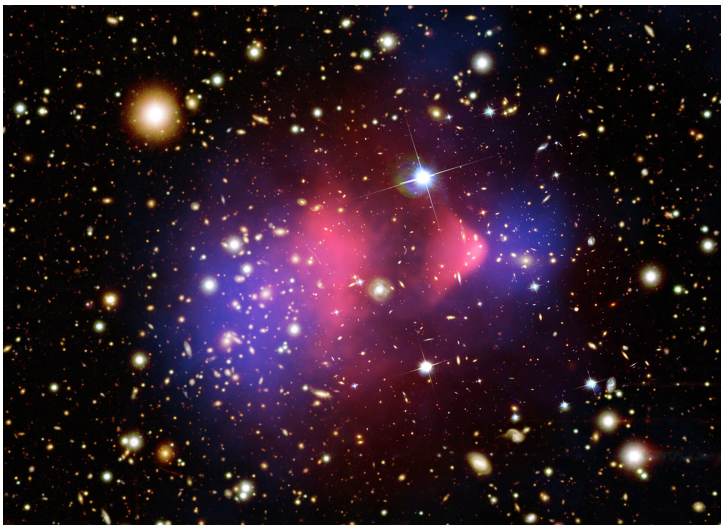

Figure 1.1: Composite image of the Bullet Cluster. Hot gases detected by the Chandra X-ray images are colored in pink, while Dark Matter distribution, inferred by gravitational lensing is colored in blue. (Credits: X-ray: NASA/CXC/CfA/M. Markevitch, Optical and lensing map: NASA/STScI, Magellan/U.Arizona/D. Clowe, Lensing map: ESO WFI) [9].

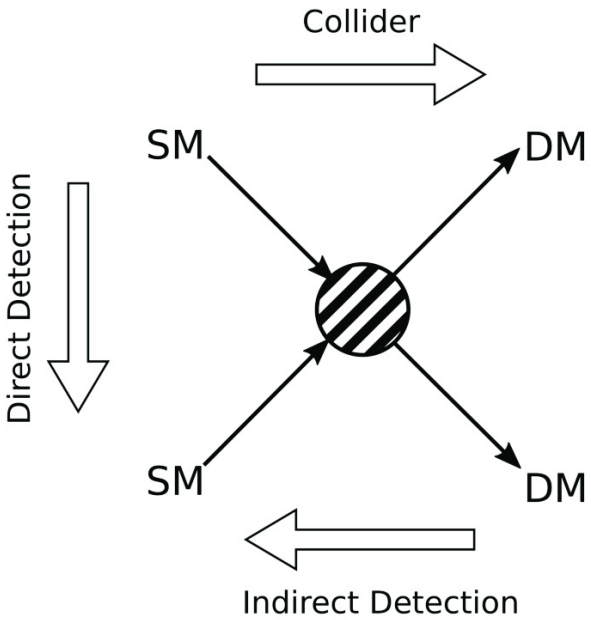

Figure 1.2: Dark matter WIMPs detection channels, using possible interactions between dark matter particles and baryonic matter particles [10].

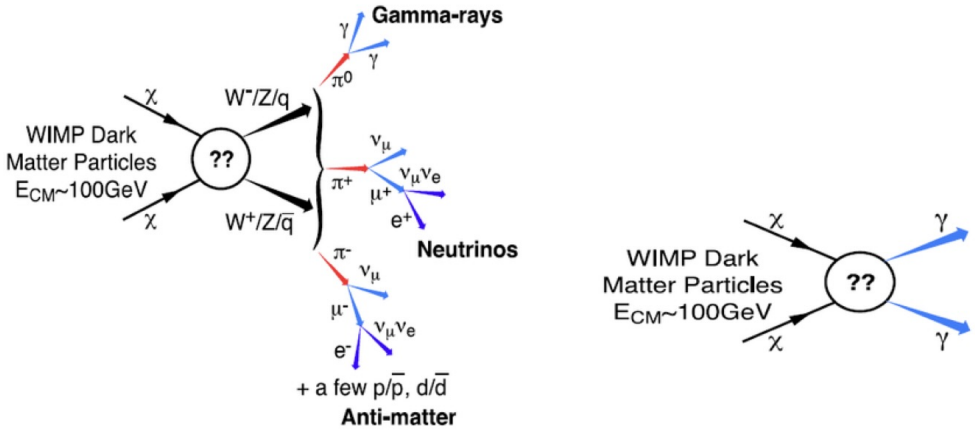

Figure 1.3: Possible annihilation channels of dark matter WIMPs into standard model particles and gamma ray photons [11].

ter particles, like hadronic collisions at the LHC, while the direct detection channel aims at observing the interaction of a WIMP with baryonic matter using huge-volume underground experiments as target material.
The indirect detection channel looks for anomalies with respect to the expected background of cosmic rays. Indeed, dark matter WIMPs are predicted to annihilate or decay into ordinary detectable particles, producing many different final states, like pairs of photons or particle-antiparticle pairs, as shown in figure 1.3. Light antinuclei as antideuterons and antihelium nuclei have been proposed as a promising indirect signal in the search for dark matter since they can be produced by antinucleons formed in WIMPs' annihilation or decay [12]. The dark matter indirect detection is focused on looking for these annihilation products coming from the center of galaxies or clusters of galaxies, where the density of dark matter particles should be higher.
One of the dedicated space-born experiments that look at cosmic radiation is the Alpha Magnetic Spectrometer-02 (AMS-02) experiment [13], located on the International Space Station (ISS). AMS-02 has collected data since 2011 and has measured the ratio of the electron-positron fluxes, which exhibits an increasing trend with the energy above 10 GeV, giving an excess over the predicted flux in cosmic rays propagation models, as in figure 1.4: this result can be interpreted in terms of electrons and positrons produced in WIMPs' annihilation [13]. However, the dark matter hypothesis is not the only possible to explain this observation. The excess in positron flux at energies greater than 10 GeV can also be explained by the presence of pulsars or other still unknown astrophysical sources. Pulsars, in particular, can produce positron-electron pairs from high-energy photons emitted from charged particles that are accelerated by the strong magnetic field of the pulsar. Astrophysical observations have recently shown that the Geminga and B0656+14 pulsars produce noteworthy emissions of extremely high-energy

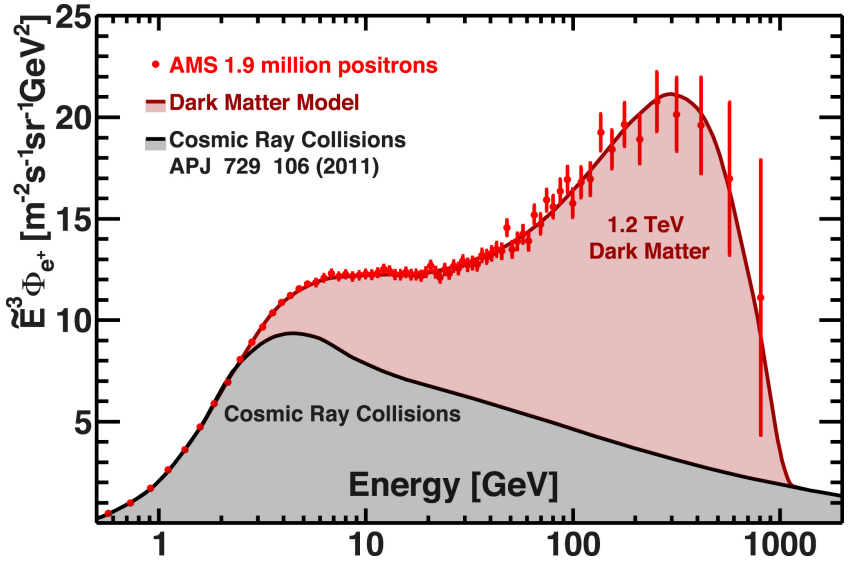

Figure 1.4: Comparison of the AMS-02 data for positron flux (red data points) with predictions of a dark matter model with mass equal to 1.2 TeV (brown curve) and predictions of cosmic ray collisions [13].

electrons [14]. AMS-02 reported also the detection of possible signals of antihelium-3 and antihelium-4, that are however still to be confirmed [15].

1.2 Cosmic antinuclei

Light antinuclei ($\overline{d}$, $\overline{^3He}$) from WIMPs are particularly promising signals because they are predicted to be almost background-free at kinetic energy per nucleon between 0.1 and 1 GeV. The astrophysical background comes from light antinuclei produced in the interaction between primary cosmic rays, mainly protons, and the interstellar medium, composed mainly of hydrogen and helium. This background peaks at higher kinetic energies (at $\sim$ 10 GeV/n) than the signal from WIMPs' annihilation or decay, expected at kinetic energy E $< O$(1GeV) (see section 3.4 in [16], or [17]). The production of light antinuclei in hadronic collisions induced by cosmic rays has a low probability since it can happen only if the energy reached in the collision is greater than the energy threshold for the nucleus-antinucleus pair production: for deuteron, for instance, the production in hadronic collision the energy threshold is 17 GeV [18, 19]. The predicted flux for antideuteron is shown in figure 1.5, where the very low background for deuteron signals from dark matter WIMPs annihilation at low energies is highlighted, and also the high separation of almost seven orders of magnitude between the fluxes of antiprotons ($\Phi_{\bar{p}} \sim 10^{-2}$ [m^{2}s·sr·GV]$^{-1}$) and of antideuteron ($\Phi_{\bar{d}} \sim 10^{-9}$ [m^{2}s·sr·GV]$^{-1}$) is shown.

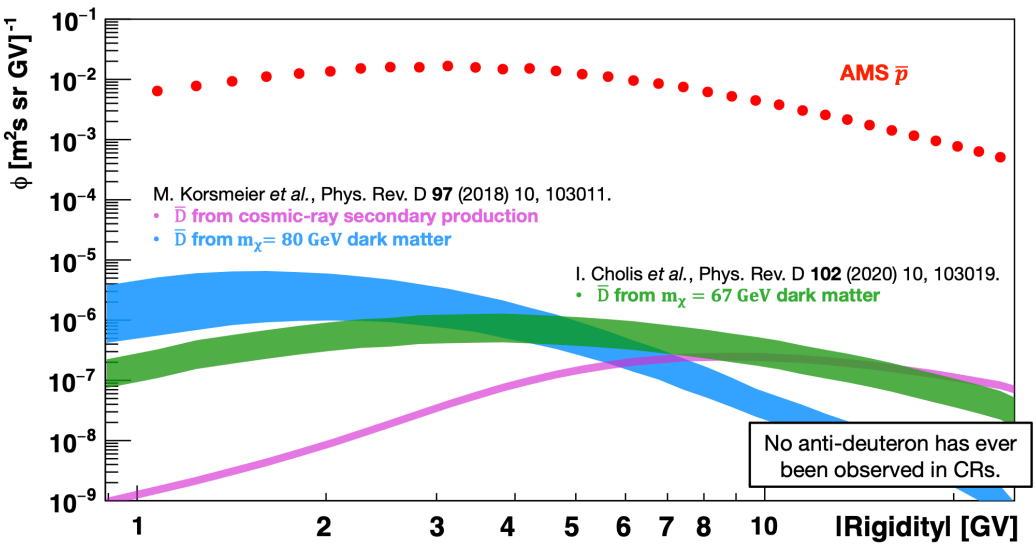

Figure 1.5: Expected signal in AMS-02 for antideuteron coming from dark matter annihilation compared with astrophysical background from antideuteron produced in interactions with interstellar medium. The error bands illustrate uncertainties in the coalescence momentum, but also include propagation uncertainties [15].

In figure 1.6, the predicted flux for antihelium-3 compared with the astrophysical background is represented according to many different dark matter models. At low energies, the signal for antihelium-3 coming from dark matter is almost background-free: the predicted flux from the secondaries antihelium nuclei forming the background is $\Phi_{^3\bar{H}e}^{background} \sim 10^{-12}$ [m^{2}s·sr·GV/n]$^{-1}$, while for antihelium produced by dark matter is greater by more than three orders of magnitude ($\Phi_{^3\bar{H}e}^{DM} > 10^{-9}$ [m^{2}s·sr·GV/n]$^{-1}$). The antihelium-3 is much rarer in cosmic radiation because of its higher production threshold energy.

A key ingredient to predict the expected signal and background rates for dark matter antinuclei searches is therefore a detailed understanding of the dynamical mechanism of the formation of light antinuclei in hadronic collisions. High-energy hadronic collisions produced at particle colliders can be used to study and validate formation models.

1.3 Light nuclei and antinuclei production models

In high-energy proton-proton (pp), proton-nucleus (pA), and nucleus-nucleus (AA) collisions, the production of light nuclei and antinuclei, like deuteron (made of a proton and a neutron), triton (made of a proton and two neutrons), and helium-3 (made of two protons and a neutron) is observed. Properties of the mentioned light antinuclei are

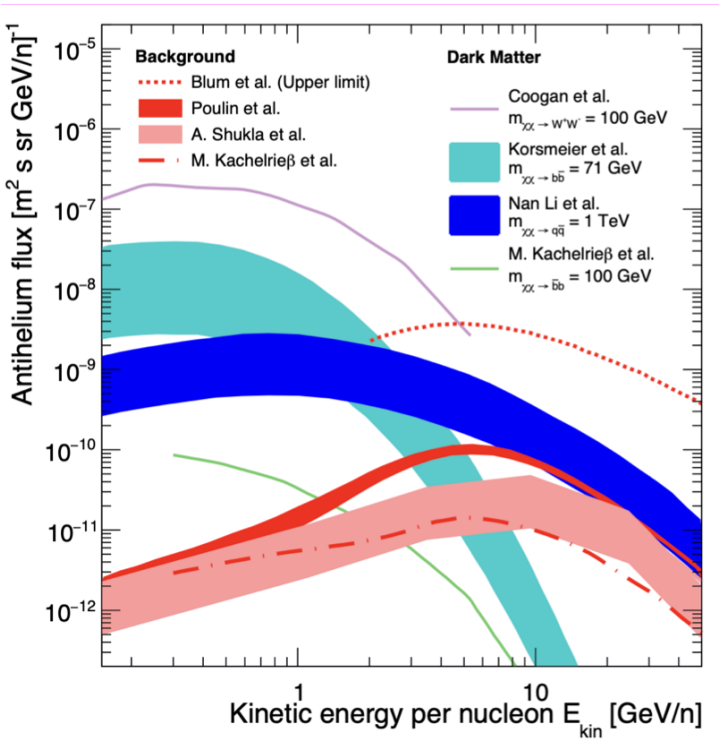

Figure 1.6: Expected flux for antihelium-3 coming from dark matter annihilation (each curve uses a different hypothesis for dark matter source and decay) compared with astrophysical background from antihelium-3 nuclei produced in interactions of primary cosmic rays with the interstellar medium. The error bands illustrate uncertainties in the coalescence momentum, but also include propagation uncertainties [20].

Nucleus	Composition	Mass (MeV/c^2)	B$_E$ (MeV)	rms radius (fm)	r$_A$ (fm)
Deuteron	pn	1875.6	2.224575 (9)	2.1413 ± 0.0025	3.2
Triton	pnn	2808.9	8.4817986 (20)	1.755 ± 0.086	2.15
Helium-3	ppn	2809.4	7.7180428 (23)	1.959 ± 0.030	2.48

Table 1.1: Properties of light nuclei: B_E is the binding energy in MeV and the size of the nucleus is given in terms of the (charge) rms radius. The parameter r_A is the size parameter of the wave-function of the harmonic oscillator potential [22].

summarized in table 1.1.
At the LHC, for instance, nuclei production models can be validated using data from proton-proton and heavy-ions high-energy collisions at the ALICE experiment [21], which is particularly well equipped to measure nuclei and identify them down to low momentum (O(GeV)).

Nowadays, the production mechanism of (anti)nuclei in high energies interactions is still not fully understood: this means to understand deeply how the strong interaction binds (anti)nucleons into (anti)nuclei and also how the internal nuclear structure can be characterized.
Two phenomenological models can be used to describe their production: the Statistical Hadronization Model (SHM) and the coalescence model. The SHM [23] adopts a macroscopic approach, and according to it, the yield of light nuclei depends on temperature, volume, and baryochemical potential [1], assuming a non-interacting quantum hadron and resonance gas in chemical equilibrium. A slight variation in temperature leads to a significant variation in production yields of light (anti)nuclei, and the greater the mass of the final state, the lower the number of produced states. The system is modeled as a grand-canonical ensemble to reproduce the light flavor hadron yields in central heavy ions collisions (like Pb-Pb) [24]. Instead, for small collision systems like p-p and p-Pb, the canonical ensemble is used, by imposing the conservation of the electric charge, baryon number, strangeness, and heavy-flavor quantum numbers [23]. In both cases, the main idea is that the (anti)nucleus is formed in a one-stage process from the interaction and then the binding of quarks and anti-quarks in a cluster. In the hadronization process, thermal droplets of quark matter are produced, such as compact and colorless objects with the quantum numbers of the final state.
Predictions from SHM can correctly reproduce ALICE data, as in reference [25], however the SHM does not provide a "microscopical" detailed mechanism of production.

[1]The baryochemical potential μ_B is the difference in number of baryons and antibaryons

1.3.1 Coalescence model

The coalescence model [26] has a microscopic point of view to describe the formation of composite objects, modeling the formation of final states in two steps: first, the formation of (anti)nucleons (n, $\bar{n}$, p, and $\bar{p}$), and then the production of (anti)nuclei. The final state is formed by the coalescence, *i.e.* the fusion, of two or more (anti)nucleons that are close in phase space at the stage of the system evolution when all the collisions stop, called the kinetic freeze-out. This means that to fuse, two nucleons must have low relative momentum and must be close enough in space.
If these conditions are met, nucleons combine into nuclei that travel in a vacuum to eventually reach the detector.
To estimate the particle yield according to coalescence, the coalescence probability, quantified by the parameter B_A, is defined as the probability of finding two or more nucleons at small relative momenta.
According to the coalescence model, the momentum distribution for a nucleus with mass number A, depends on the nucleon distributions and on B_A:

$$E_A \frac{d^3N_A}{dp_A^3} = B_A \left(E_p \frac{d^3N_p}{dp_p^3} \right)^Z \left(E_n \frac{d^3N_n}{dp_n^3} \right)^N \tag{1.1}$$

where E_A indicates the nucleus energy and p_A is the momentum of the nuclei with the mass number $A = N + Z$, while E_p (E_n) and p_p (p_n) are the energy and momentum for the proton (neutron).
Assuming an equal distribution in energy for protons and neutrons ($p_n = p_p = \frac{p_A}{A}$), equation 1.1 becomes:

$$E_A \cdot \frac{d^3N_A}{d^3P_A} = B_A \cdot \left(E_{p,n} \frac{d^3N_{p,n}}{d^3p_{p,n}} \right)^A \tag{1.2}$$

The assumption $p_n = p_p = \frac{p_A}{A}$ is well motivated in high energy collisions, where the number of produced protons and neutrons at midrapidity, as well as their momentum distributions are expected to be equal. Equation 1.2 is used to determine experimentally the coalescence parameter because in this case, it is not necessary to consider neutrons, usually difficultly detectable.
Figure 1.7 shows the coalescence parameter B_2 for deuteron and antideuteron as a function of the transverse momentum per nucleon p_T/A [2], from ALICE data in proton-proton collisions at the collision energies of 0.9 TeV, 2.76 TeV and 7 TeV. The dependence on the collision energy is not very strong since the coalescence parameter (on the y-axis) is compatible across the three different panels.

In figure 1.8, predictions from coalescence and statistical models are compared with the ALICE collaboration data from different collision energies and systems [28]. More

[2]The traverse momentum $p_T = \sqrt{p_x^2 + p_y^2}$, where p_x and p_y are the components of the momentum p respectively along the x and y axis.

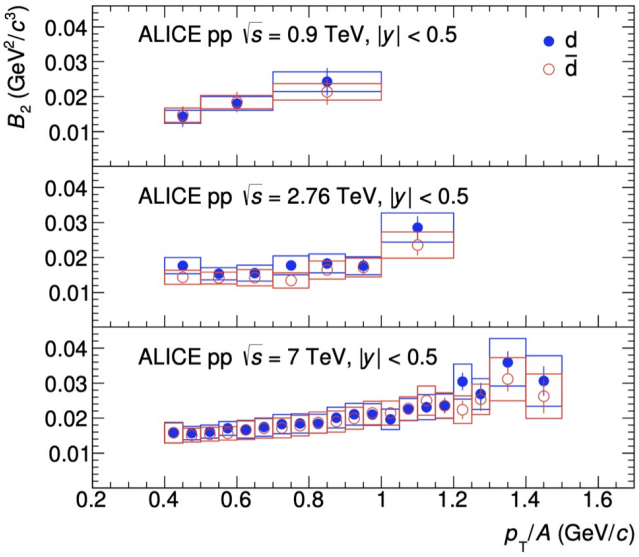

Figure 1.7: Coalescence parameter for deuteron (blue) and antideuteron (red) as a function of p_T/A for different collision energies in pp collisions at the LHC measured by the ALICE experiment [27]. The coalescence probability seems almost independent of the transverse momentum and of energy.

specifically, the coalescence parameter is strongly dependent on the average charged-particle multiplicity density at central rapidity ($|y|$ <0.5) $\langle dN/d\eta \rangle$, for a given value of p_T/A. The multiplicity density $\langle dN/d\eta \rangle$ is proportional to the volume, and thus to the cube of the source radius. The B_A parameter exhibits a strong dependence on the volume of the particle emitting region, called the source: the greater the volume of the particle emitting region, the greater the distance between produced nucleons, and the lower the coalescence probability. This effect is less visible in small collision systems, like pp or pPb collisions, since the size of the produced nucleus is larger than that of the emitting region (chapter 5.1 in [28]).

Some simplified coalescence models [29] do not care about the particle emitting region size. However, they are not predictive for heavy-ion collisions, and they are not able to explain the observed elliptic flow of deuteron. More comprehensive coalescence models take into account the source size R and an explicit dependence of the coalescence probability on R can be derived, following computations in [22] and [26].
Considering coalescence as a quantum-mechanical process, the Wigner formalism must be adopted to define the phase space. The coalescence probability corresponds to the overlapping probability between the nucleon pair (initial state) and the nucleus (final bound state) wave functions. For deuteron the simplest wave function used in calcula-

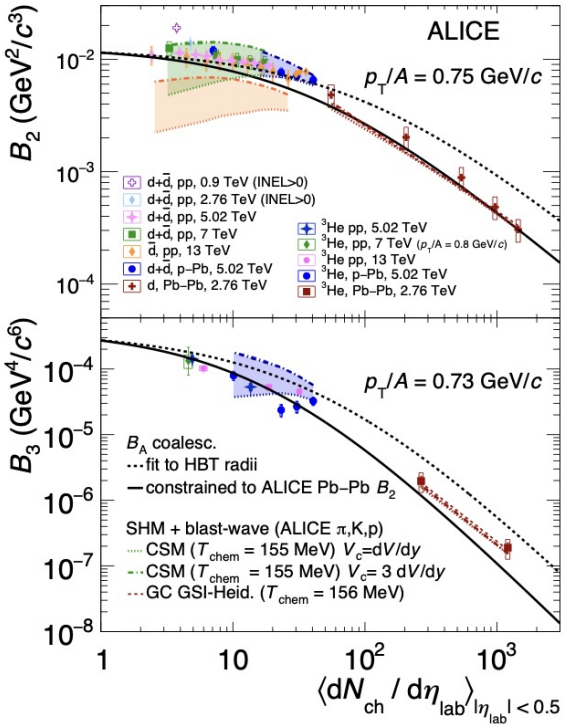

Figure 1.8: Coalescence probability for deuteron (B_2) and for helium-3 (B_3) as a function of $\langle dN/d\eta \rangle$. The multiplicity dependence of $B_{2,3}$ in different collision systems and different center-of-mass energies ($\sqrt{s}$) of the collision is shown for fixed p_A/A.

tions is Gaussian and is expressed as

$$\phi_d(\vec{r}) = \left(\pi r_d^2\right)^{-\frac{3}{4}} \exp\left(-\frac{r^2}{2r_d^2}\right) \tag{1.3}$$

where r_d is the the deuteron radius and $\vec{r}$ is the relative distance between the two nucleons inside the deuteron.
In order to consider the quantum-mechanical nature of the process, an additional correction factor must be included [26]. For deuteron, it can be written as

$$\langle C_d \rangle \approx \left[1 + \left(\frac{r_d}{2R(m_T)}\right)^2\right]^{-\frac{3}{2}} \tag{1.4}$$

but for a general nucleus of mass number A, it becomes:

$$\langle C_A \rangle = \prod_{i=1}^{3} \left[1 + \frac{r_i^2}{4R_i^2}\right]^{-\frac{1}{2}(A-1)} \tag{1.5}$$

where $\langle C_i \rangle$ is the correction factor for deuteron (if $i = d$) or for the nucleus with mass number A (if $i = A$); r_A is the radius of the nucleus and R_A is the emitting source size. In equation 1.4, m_T is the transverse mass defined as $m_T = \sqrt{k_T^2 + m^2}$ (k_T is the transverse momentum of the pair and m the average pair mass). Assuming that the three dimensions of the emitting source are equal ($R_1 \approx R_2 \approx R_3 \approx R$), the coalescence parameter for a nucleus A is expressed as a function of the total angular momentum J_A, r_A, R and m_T:

$$B_A = \frac{(2J_A + 1)}{2^A} \frac{1}{\sqrt{A}} \frac{1}{m_T^{A-1}} \left(\frac{2\pi}{R^2 + \left(\frac{r_A^2}{2}\right)^2}\right)^{3/2(A-1)} . \tag{1.6}$$

The B_A parameter is dependent on the internal structure of the considered nucleus and on the size of the produced nucleus r_A, that, as in table 1.1, is generally defined as the r.m.s. of the (charge) distribution, measured of about 2 fm for light (anti)nuclei in electron-nucleus scattering experiments.
For deuteron the expression 1.6 is simplified in:

$$B_2 = \frac{3\pi^{\frac{3}{2}} \langle C_d \rangle}{2m_T R^3(m_T)}. \tag{1.7}$$

The expression 1.6 for B_A is general, and exhibits an explicit inverse proportionality with respect to R, because the coalescence probability decreases for distant nucleons. This

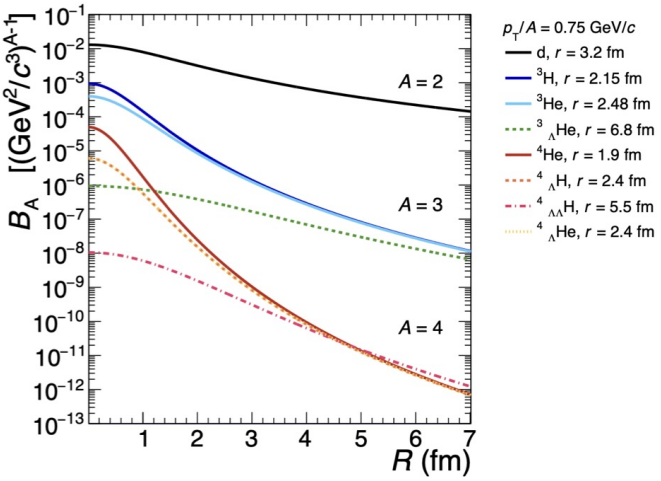

Figure 1.9: Coalescence parameter in function of the source size R for different nuclei (A= 2, 3 and 4) with different nuclear size r_A. The coalescence probability is inversely proportional to the source size, and the greater is A, the lower the coalescence probability B_A [30].

dependence on R is shown in figure 1.9 for different nuclei with A = 2, 3, and 4. For nuclei with the same mass number A, like ^3H and ^3He, the coalescence parameter is different because the nuclei size is different and the greater is r_A, the lower is B_A. The dependence on r_A is more evident in small collision systems like pp, because the source's ($R \sim 1$ fm) becomes comparable with the nucleus size or smaller ($r_A \sim 2$ fm)

1.3.2 Nucleon coalescence from correlation functions

The coalescence model can be tested and supported by studies of the momentum-space correlations of particles emitted in hadronic collisions with a technique called femtoscopy. This is further discussed in chapter 3. Using the effective quantum mechanical approach to describe the dynamics of non-relativistic particle-pairs that form the final bound state in the pair rest frame, it is possible to derive the correlation formalism, which offers the two-particle source size as a measurable quantity to test the model. The approach is fully explained in [31] and [32] and it is only summarized here.

The equation 1.6 gives the coalescence probability for a cluster with mass number A and a dimension $r_A > R$, at $p_T \approx 0$. The homogeneous source is parameterized by the correlation-source radius R, which is almost of 1 fm in pp collisions and of 5 fm in Pb-Pb collisions. Thus, the coalescence probability in pp collisions is greater than in Pb-Pb collisions (e.g. $B_3^{pp}/B_3^{PbPb} \sim 4 \cdot 10^3$). Even if the relation 1.6 is derived under many approximations and no precise model for the source, it gives results consistent with ALICE measurements [27](see figure 1.8), with an accuracy at $O(1)$ over orders of

magnitude in B_A.
The B_A can be defined from equation 1.2 as the ratio between Lorentz-invariant differential yields for the nucleus with mass number A and the for constituent nucleons (p and n):

$$B_A = \frac{E_A \frac{dN_A}{d^3P_A}}{\left(E_{p,n}\frac{dN_{p,n}}{d^3P_{p,n}}\right)^A}, \tag{1.8}$$

where numerator and denominator are calculable from quantum mechanics without any assumption, and obtaining a model-independent relation to calculate the coalescence probability.

The deuteron Lorentz-invariant yield in non-relativistic calculations is:

$$\gamma_d \frac{dN}{d^3P_d} \approx \frac{G_d}{(2\pi)^6}\int d^3q D_d(\vec{q},\vec{r}) \int d^3R \int d^3r e^{i\vec{q}\vec{r}} f_1^W(\frac{\vec{P}_d}{2},\vec{R}+\frac{\vec{r}}{2}) f_1^W(\frac{\vec{P}_d}{2},\vec{R}-\frac{\vec{r}}{2}) \tag{1.9}$$

where γ_d is the deuteron Lorentz factor, P_d is the deuteron momentum in the laboratory frame, r is the distance, and q the relative momentum between the two nucleons forming the deuteron, G_d is a dimensionless normalization factor, D_d is the Wigner density of the deuteron, and f_1^W are the density function related in the Wigner formalism to the single-particle density matrix ρ_1, which describes the high excitation state produced in hadronic collisions.
Considering two free nucleons, neglecting the final state interaction, the differential yield of the pair with respect to single-particle momentum (p_1 and p_2) for spin-symmetric (s) and spin anti-symmetric (a) configuration is:

$$\frac{dN^{s,a}}{d^3p_1 d^3p_2} = G_{s,a}^2 \left(A_2(p_1,p_2) \mp F_2(P,q)\right) \tag{1.10}$$

where $G_{s,a}$ is a dimensionless normalization factor, and,

$$\begin{aligned} F_2(P,q) &= \frac{1}{(2\pi)^6}\int d^3R \int d^3r\, e^{i\vec{q}\cdot\vec{r}}\, f_1^W\left(\vec{P},\vec{R}+\frac{\vec{r}}{2}\right) f_1^W\left(\vec{P},\vec{R}-\frac{\vec{r}}{2}\right), \\ A_2(p_1,p_2) &= \frac{1}{(2\pi)^6}\int d^3x\, f_1^W(\vec{p}_1,\vec{x}) \int d^3x\, f_1^W(\vec{p}_2,\vec{x}). \end{aligned} \tag{1.11}$$

being $\vec{x}$ the position vector of the nucleon.
The two-particle correlation function can be defined like:

$$C_2(P,q) = \frac{E_{01}E_{02}\cdot\frac{dN}{d^3p_1 d^3p_2}}{\left(E_{01}\frac{dN}{d^3p_1}\right)\cdot\left(E_{02}\frac{dN}{d^3p_2}\right)}. \tag{1.12}$$

where $E_{01,2}$ are the energies for particles 1 and 2, and $p_{1,2}$ their momenta. Equation 1.12 presents the correlation function as the ratio between the emission spectrum for two

nucleons over the single-nucleon spectra. In the non-relativistic limit ($|\vec{q}| \ll m$) in the pair rest frame (PRF), the correlation function is equal to:

$$C_2^{PRF}(P,q) = 1 - \frac{G_s^2 - G_a^2}{G_s^2 + G_a^2} \cdot \mathcal{C}_2^{\mathrm{PRF}} \tag{1.13}$$

with the function $\mathcal{C}_2^{\mathrm{PRF}}$ that comes from F_2 and A_2. The coalescence parameter in equation 1.8, can be written as:

$$B_2(p) \approx \frac{3}{2m} \int d^3q \, D_d(\vec{q}) \, \mathcal{C}_2^{\mathrm{PRF}}(\vec{p}, \vec{q}) \tag{1.14}$$

assuming $G_d = G_s^2 = 3$ and $G_a^2 = 1$ for an unpolarised isospin-symmetric excited state. Equation 1.14 is the integral relation between the coalescence parameter and the two-particle correlation function, weighted by the deuteron density probability D_d. This relation reproduces equation 1.7 assuming a Gaussian deuteron wave function, as in equation 1.3 with $r_d = 3.2$ fm (see table 1.1), and Gaussian particle density D_d. Using $\mathcal{C}_2^{\mathrm{PRF}} = \lambda e^{-R_\perp^2 q_\perp^2 - R_\parallel^2 q_\parallel^2}$, where λ is the chaoticity parameter which takes into account experimental effects, and the R (as well as the momentum q) is decomposed into the perpendicular ($R_\perp$) and parallel ($R_\parallel$) components with respect the beam axis,

$$B_2 = \frac{(3\pi)^{3/2}\lambda}{2m_T(R_\perp^2 + \frac{r_d^2}{2})\sqrt{(R_\parallel^2 + \frac{r_d^2}{2})}}. \tag{1.15}$$

The derived expression of the coalescence parameter can be generalized to a nucleus with mass number A, obtaining the expression for B_A:

$$\frac{B_A}{m^2(A^{-1})} = \lambda^{A/2} \frac{2J_A + 1}{2^A\sqrt{A}} \left[\frac{(2\pi)^{3/2}}{m^3(R_\perp^2 + \frac{r_d^2}{2})\sqrt{(R_\parallel^2 + \frac{r_d^2}{2})}} \right]^{A-1}. \tag{1.16}$$

These theoretical calculations agree with the experimental data measured with the correlation technique, and the comparison is in figure 1.10. The grey band is the theoretical prediction calculated using equations 1.15 and 1.16, while the red (blue) bands are experimental results for B_2 and B_3 in Pb-Pb collisions respectively at 0-10% (20-40%) and 0-20% (20-80%) centrality classes. In green, the pp collision result.
The success of the correlation technique to describe the two-nucleon source using a Gaussian profiile is the most successful evidence supporting the coalescence model.

Experimental data, in figure 1.11, show the source radius measured with correlation technique, as dependent on the multiplicity $\langle dN_{ch}/d\eta \rangle$. The increase of the event multiplicity corresponds to an increasing radius.
In heavy-ion collisions, this behavior may be further affected by particle composition and

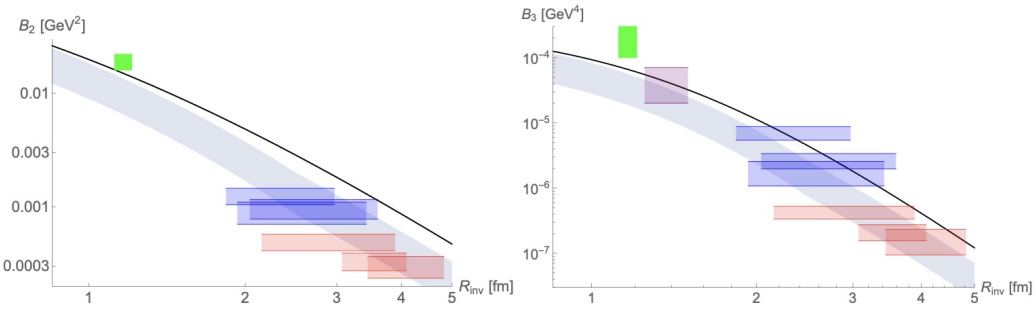

Figure 1.10: Comparison between theoretical calculations (grey band) and experimental results from correlation measurements in Pb-Pb collisions (red and blue) at different centrality classes, and in pp collisions (green) [31].

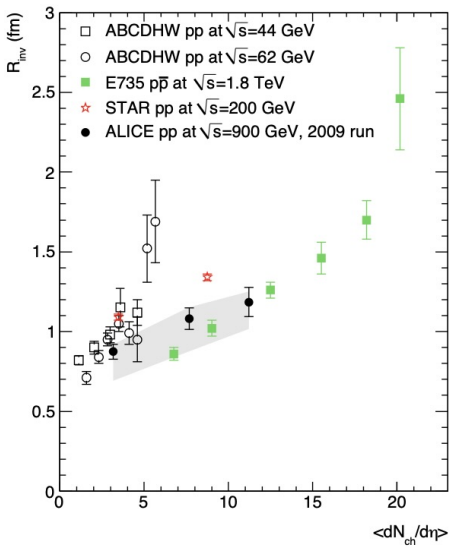

Figure 1.11: One-dimensional Gaussian source radius in pp collisions at $\sqrt{s} = 900$ GeV determined using pion pairs with k_T = 0.1-0.55 GeV/c, as a function of the charged-particle multiplicity at midrapidity. ALICE data (black dots) are compared with data from ISR (open symbols), RICH (red stars), and Tevatron (green) [33].

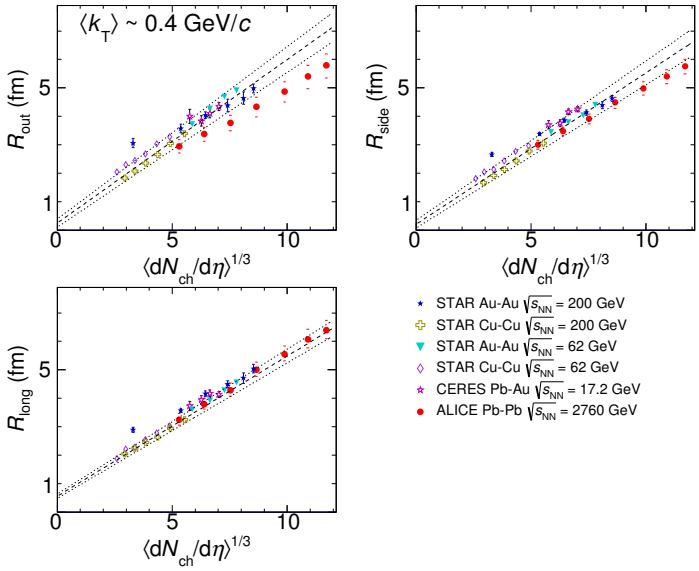

Figure 1.12: Source radii compared for different heavy-ion collision systems and energies. The radius is shown as a function of the measured charged particle multiplicity. Dashed lines show linear fits performed to heavy-ion data [34]

.

hadronic scattering in the final state system, while in high-energy pp collision systems from hard parton and hadron scattering.

As a final remark, it is worth mentioning that experimental source radius measured in different heavy-ion collisions systems, including also Pb-Pb collisions at the ALICE detector, show a shape as dependent on the event multiplicity that is consistent with the theoretical predictions.

Final note on the comparison between SHM and Coalescence

Despite being often opposed, the statistical hadronization and coalescence approaches are not incompatible, and they agree for certain choices of the parameters [23]. Overall, both models can provide quantitative predictions about particle yields calculated at certain stages in hadronic collisions. For SHM, abundances are calculated at the chemical freeze-out, *i.e.*, when inelastic processes that change the species of hadrons cease, and the hadron abundances remain constant, while in the coalescence model, the kinetic freeze-out, *i.e.* where all types of momentum-changing collisions, elastic and inelastic cease, is taken as a reference.

More precise measurements are needed to clarify the production mechanisms of light (anti)nuclei in the light of experimental data and will allow one to test configurations of these models. These studies are important also to test predictions and precision of

Quantum Chromo Dynamics, as discussed in the following chapter 2.

Chapter 2

Strong interaction

Nucleons are bound into nuclei by the strong interaction. In this relation, the study of the strong potential is a crucial ingredient in coalescence models because it strongly affects the shape of the momentum correlation among nucleon pairs. The theory of the strong interaction is one of the main components of the Standard Model of particle physics, which is a gauge theory able to quantitatively describe and predict phenomena involving elementary particles interacting through strong and electroweak forces. The strong interaction is described by Quantum ChromoDynamics (QCD) [35], and it involves quarks and gluons, being the only elementary particles that are color charged, *i.e.* strongly interacting. In this chapter, after a brief introduction on QCD, the nucleon-nucleon interaction is discussed.

2.1 Strong interaction in the Standard Model

In the Standard Model, there are six different quark flavors (up, down, charm, strange, top, bottom), and each flavor of quarks comes in three different strong charges, red, green, or blue. Each quark is a fermion with spin equal to 1/2, and it is associated with a spinorial field ψ_c^f, where f indicates the flavor and C the color. Instead, gluons are the eight gauge fields with spin equal to 1 that mediate the strong interaction.
QCD is a gauge field theory based on the non-abelian $SU(3)_c$ symmetry group. Since the group of symmetry is non-abelian, quarks are confined in hadrons, classified in mesons or baryons, that are color neutral; thus, it is not possible to observe isolated colored particles. This peculiar characteristic of the strong interaction comes from the QCD Lagrangian. The free Lagrangian for quark fields is:

$$L_o = \sum_{f=1}^{6} \sum_{C=r,g,b} \overline{\psi_c^f}(i\gamma^\mu \delta_\mu - m_0^f)\psi_c^f \tag{2.1}$$

where ψ_c^f is the spinorial field with flavor f and color C, γ^μ are the Dirac matrices, δ_μ is the derivative, and m_0^f is the rest mass of the quark with flavor f. Imposing the invariance under $SU(3)_c$ transformations and extending the global gauge symmetry to local symmetry, the resulting Lagrangian is:

$$L_o = \sum_{f=1}^{6} \sum_{C=r,g,b} \overline{\psi_c^f}(i\gamma^\mu D_\mu - m_0^f)\psi_c^f \tag{2.2}$$

where the derivative δ_μ must be replaced with the covariant derivative $D^\mu = \delta^\mu + ig_s A^\mu$ to guarantee local invariance. The g_s parameter is the coupling constant measuring the effective strength of the quark–gluon interaction, and A^μ are the eight gauge field correspondent to the eight gluonic fields. To conserve the required local invariance, the gluonic fields must transform like:

$$A^\mu \longrightarrow A^{\mu'} = U(x)A^\mu U^{-1}(x) + \frac{i}{g_s}[\delta^\mu U(x)]U^{-1}(x) \tag{2.3}$$

with U a unitary matrix representing the special unitary transformation ($U \in SU(3)_C$). In order to have propagating gluon fields, it is necessary to add dynamic terms in equation 2.2. In particular we can define the tensor $F_{\mu\nu}$ as:

$$[D_\mu; D_\nu] = ig_s F_{\mu\nu}, \tag{2.4}$$

which is used to describe the propagation of the gauge fields. The final QCD Lagrangian results in:

$$L_{QCD} = \sum_{f=1}^{6} \sum_{C=r,g,b} \overline{\psi_c^f}(i\gamma^\mu D_\mu - m_0^f)\psi_c^f - \frac{1}{4}\sum_{a=1}^{8} F^{a\mu\nu}F^a_{\mu\nu} \tag{2.5}$$

where the index a represents the gluonic field. In the Lagrangian, terms corresponding to quark-gluon and gluon-gluon vertices are included. That means that, in QCD, the self-interaction of gluonic fields is allowed, as illustrated in figure 2.1.

The possibility of having gluonic loops can explain the quark confinement and the variation of the strength of the strong coupling constant with the energy scale. In fact, a free quark polarizes the vacuum around it, and the color charge appears surrounded by quark loops, which create a screening effect, and gluonic loops, which create an anti-screening effect. The result is that at large distances from the charge, the strong field is increased due to the anti-screening effect; on the other hand, approaching the charge, at even smaller distances, the strong field is reduced, becoming negligible, and thus, quarks are free and do not interact strongly anymore. This feature is called "asymptotic freedom" [36].

The behavior of the strong field, for the energy scale of the process, is described by the running of the strong coupling constant $\alpha_s = \frac{g_s^2}{4\pi}$, as in figure 2.2. This does not have a

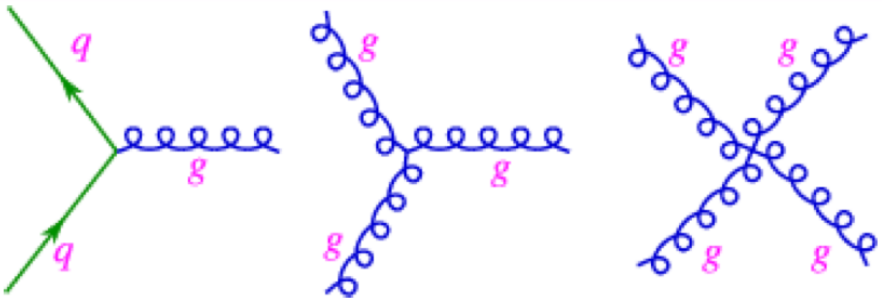

Figure 2.1: The basic QCD Feynman vertices.

constant value but depends on the transferred momentum Q or the distance from the color charge.
At small Q, $\alpha_s \approx 1$ making the contribution of the higher-order vertices stronger and forbidding the use of perturbation theory to model the interaction. In such an energy regime, *lattice* QCD is used: an approach based on the discretization of space-time (modeled as a lattice), making possible analytical and numerical calculations in a non-perturbative regime.
Instead, at higher Q, the QCD can be treated perturbatively (pQCD): this consists in a possible expansion of a physical quantity to higher orders in α_s, with only lower order terms contributing significantly, to describe the effects of the strong interaction among particles. In the high energy regime (E > 100 GeV), we expect a weaker coupling constant that allows quarks and gluons to be almost free in a deconfined state of matter [37].

The $SU(3)_c$ invariance results in the conservation of the color charge; moreover, the invariance of the Lagrangian for the strong interaction with respect to U(1) (describing phase transformations in the space of Dirac spinors) and SU(2) (describing transformations of wave fields between quarks up and down) symmetry groups are reflected respectively into the conservation of the fermionic number and of the strong isospin (limited to up and down states).

2.2 Nucleon−Nucleon interaction

Quarks are the elementary components of nucleons, *i.e.*, protons (correspondent to quark combination up-up-down) and neutrons (correspondent to quark combination up-down-down). However, to derive the nuclear force in terms of quarks and gluons is a very complex problem that can be only solved using computational power. The nuclear force, which is the interactions among nucleons, is a residual of the color interaction among quarks, thus it is studied by QCD at low energy, where the theory is non-perturbative and it hence requires lattice QCD.

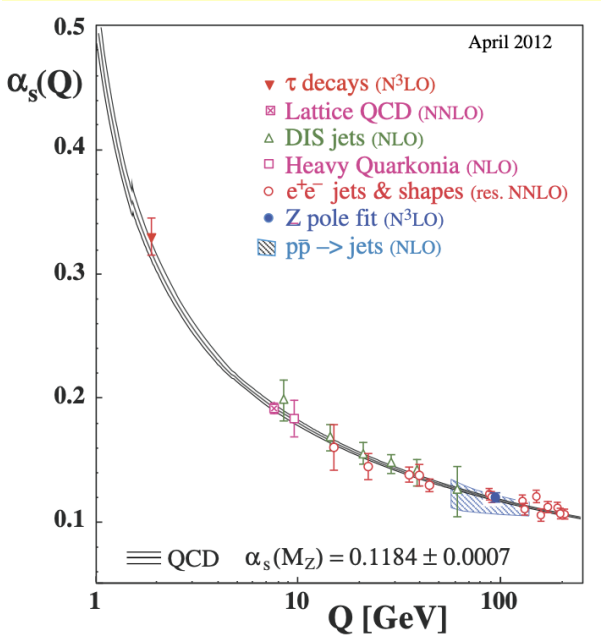

Figure 2.2: The strong coupling α_s as a function of the energy scale Q. The value is calculated at the energy equivalent to the Z boson mass [38].

The understanding of Nucleon-Nucleon (N−N) interaction is described in nuclear physics by the following proprieties:

- At short distances, the strong interaction is stronger than the Coulomb force: the Coulomb repulsion between protons in the same nucleus is overcome by the strong interaction between nucleons.
- The strong interaction is short-range: at a large distance (on the order of the atomic size), the nuclear force is negligible, and only the Coulomb force is relevant.
- Some particles, like electrons, do not feel strong force because they are colorless particles.
- The N−N force is independent of the type of nucleon (proton or neutron).
- The N−N force depends on the spin of nucleons involved (triplet or singlet state).
- A repulsive term in the strong potential must be included at very short distances to keep the nucleons at a specific average separation. This term must be non-central to ensure the non-conservation of the orbital angular momentum.

These proprieties must be included in the Hamiltonian and in the Schrödinger equation when describing a nucleus.

2.2.1 The deuteron

The simplest two-nucleon problem that is analytically solvable in quantum mechanics is the one of the deuteron (d or ^{2}H), formed by one proton and one neutron that interact strongly but do not feel either the Coulomb interaction or the Pauli blocking. Comparing model predictions with experimental results, the modeled characteristics of the nuclear force can be verified.
In first approximation, the interacting potential can be described by a square-well potential with depth equal to V_0 and range R, as in figure 2.3. To have a bound state of two nucleons, the potential depth, V_0, must be greater than the kinetic energy of the pair, E_{kin}. Assuming $R \approx 2.1$ fm for the charge radius measured for deuteron (table 1.1), and μ for the reduced mass of neutron and proton, the condition becomes:

$$V_0 > E_{kin} = \frac{\hbar^2 \pi^2}{8\mu c^2 R} = 23.1 \text{ MeV}. \tag{2.6}$$

The binding energy for the deuteron at the ground level has been calculated as:

$$E_{BE} = E_{kin} - V_0 = \text{-}2.2 \text{ MeV}. \tag{2.7}$$

This result is very close to the very precise measurement carried out in [39] using the mass difference between neutron (n) plus proton (p), and deuteron (d):

$$E_{BE} = [m(p) + m(n) - m(d)] \approx 2.22463 \pm 0.00004 \,\text{MeV} \tag{2.8}$$

The potential can be written as:

$$\begin{cases} V(r) = -V_0 & r < R \\ V(r) = 0 & r > R \end{cases} \tag{2.9}$$

where r is the relative distance between the two interacting nucleons.
The Schrödinger equation can be written as:

$$\left(\frac{\hbar^2}{2\mu} \frac{1}{r^2} \frac{\partial}{\partial r} \left(r^2 \frac{\partial}{\partial r} \right) + \frac{\hat{L}^2}{2\mu r^2} + V_{\text{nucl}}(r) \right) \Psi_{n,l,m}(r, \theta, \phi) = E_n \Psi_{n,l,m}(r, \theta, \phi) \tag{2.10}$$

where $\hbar = 1.05$ x 10^{-34} $J \cdot s$ is the reduced Plank's constant, $\mu = \frac{m_p m_n}{m_p + m_n}$ is the p$-$n reduced mass, $\hat{L}^2$ is the angular momentum operator, $V_{\text{nucl}}(r)$ is the nuclear potential as in equation 2.9 and E_n is the energy eigenvalue, while $\Psi_{n,l,m}(r, \theta, \phi)$ is the two-body wave function for the energy level defined by quantum numbers n, l and m as a function of the spatial spherical coordinates (r, θ and ϕ).
The ground state for deuteron is for orbital angular momentum $l = 0$, and no deuteron excited states have been observed because the bound state would split between a free

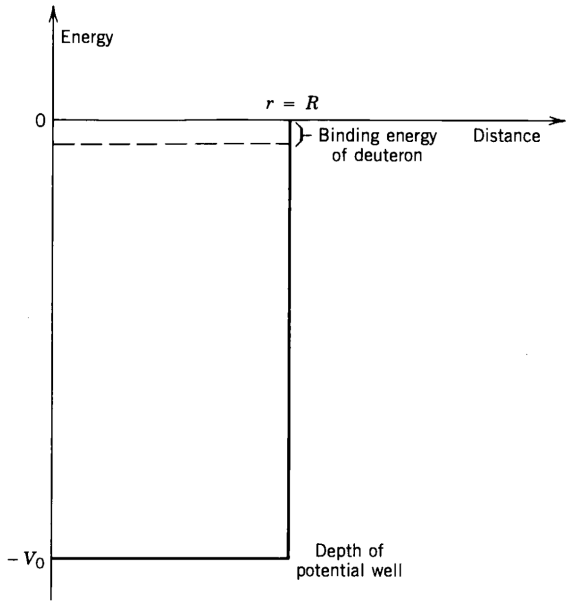

Figure 2.3: The square-well potential, used to model the strong N−N interaction in first approximation. For deuteron, the depth $V_0 \approx 25$ MeV and $R \approx 2.1$ fm. The binding energy $E \approx 2.2$ MeV (chapter 4, [39]).

proton and a free neutron if excited.
A central problem can be split into a radial and an angular problem. The solutions for the angular problem are the spherical harmonics $Y_l^m(\theta, \phi)$:

$$\hat{L}^2 Y_l^m(\theta, \phi) = \hbar^2 l(l+1) Y_l^m(\theta, \phi) \tag{2.11}$$

The radial problem for $l = 0$ can be written as:

$$\left[-\frac{\hbar^2}{2\mu} \frac{1}{r} \frac{\partial^2}{\partial r^2} + V_{nucl}(r) \right] u_0(r) = E_0 u_0(r) \tag{2.12}$$

and the solutions $u_0(r)$ are:

$$\begin{aligned} u_0(r) &= A \sin(k_1 r) + B \cos(k_1 r), & 0 < r < R \\ u_0(r) &= C e^{-k_2 r} + D e^{k_2 r}, & r > R \end{aligned}$$

where $k_1 = \sqrt{2m(V_0 + E)/\hbar^2}$ and $k_2 = \sqrt{-2mE/\hbar^2}$. The A, B, C, and D parameters could be found by applying the boundary conditions and imposing the continuity of $u(r)$ and its first spatial derivative $\frac{\partial u(r)}{\partial r}$.

It is necessary to consider also the interaction between nucleon spins that can produce an additional spin-dependent term in the potential. The total angular momentum is:

$$\vec{I} = \vec{L} + \vec{S}_n + \vec{S}_p + \vec{LS} \tag{2.13}$$

where $\vec{S}_{n,p}$ is the spin of the neutron (proton) that is equal to 1/2, while $\vec{L}$ is equal to 0 if $l = 0$ and $\vec{LS}$ is the spin-orbit interaction term. In principle $I = 0, 1$ for singlet ($\vec{S}_n + \vec{S}_p = 0$) and triplet state ($\vec{S}_n + \vec{S}_p = 1$). The deuteron has been observed only in the triplet state configuration, meaning it has lower energy than the singlet state.

2.2.2 Nucleon−Nucleon interaction from lattice QCD

The Nucleon−Nucleon (N−N) interaction potential can be extracted from lattice QCD, which offers the possibility to derive the interaction potential among baryons and study multi-hadron systems using a method called HAL QCD [40, 41, 42]. Scattering states of hadrons with different energies are used to extract non-local hadron–hadron potential without the necessity of splitting the energy eigenstates that have a very small separation, since on the lattice scattering states at different energies are governed by the same non-local (energy independent) potential.
The HAL QCD method aims at calculating the interaction potential starting from spatial correlation from QCD on a lattice [41]. The main observed quantity is the so-called 4-point correlation function, which for two baryons (such as the nucleons) is defined as:

$$\phi(\vec{r}, t) = \frac{1}{\sqrt{Z_B Z_{B'}}} \sum_{\vec{x}} \langle 0|B(\vec{x} + \vec{r}, t)B'(\vec{x}, t)J(t_0)|0\rangle \tag{2.14}$$

where B and B' are two baryon field operators, $J(t_0)$ is the source operator that creates two baryons at time t_0, $\vec{x}$ and t are the spatial and time coordinates, while $\vec{r}$ is the distance between the two baryons on the lattice. The parameters $Z_B, Z_{B'}$ are renormalization factors.
A 4-point function corresponds to a mixture of eigenstates that are written in terms of the Nambu–Bethe–Salpeter wave functions $\psi_k(\vec{r})$ with energy W_k in eigenstate k:

$$\phi(\vec{r}, t) = \sum_k A_k \psi_k(\vec{r}) e^{-W_k(t-t_0)} \tag{2.15}$$

with amplitude normalization factor A_k. Equation 2.15 shows the relation between the 4-point correlation function, calculable from lattice QCD, and the eigenstate wave functions, containing scattering observable like the phase shift [42]. The $\psi_k(\vec{r})$ cannot be calculated practically since eigenstates have very small energy differences, making their separation results impossible. The 4-point function in equation 2.14 is calculated using wall-type source operator $J(t_0)$ and point-type baryon field operators B and B',

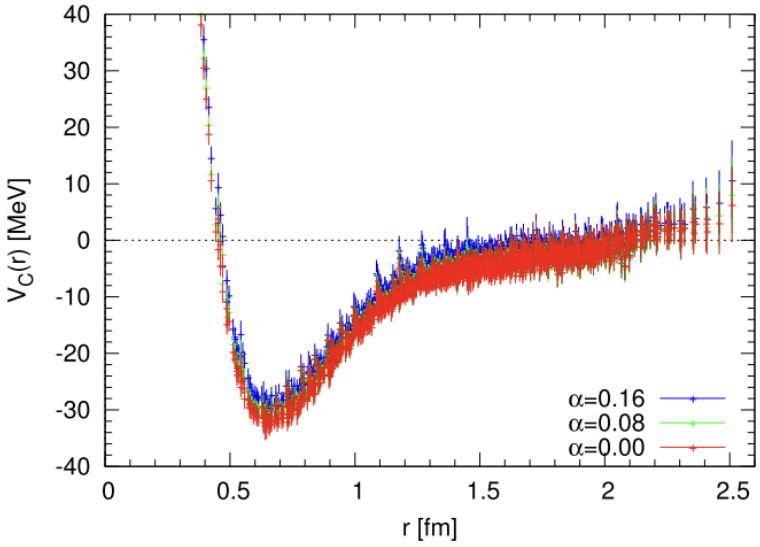

Figure 2.4: Central potentials obtained by HAL QCD method using equation 2.17 at t = 9 for three different source functions at the variation of a parameter α [42].

minimizing the non-locality of potential.
However, knowing $\phi(\vec{r},t)$, the interaction potential is derived through the time-dependent Schrödinger equation of the 4-point function, that for two nucleons (N) with mass M_N and reduced mass μ, is:

$$-\frac{\partial}{\partial t}\phi(\vec{r},t) = \left[2M_N - \frac{\nabla^2}{2\mu}\right]\phi(\vec{r},t) + \int d^3\vec{r'}U(\vec{r},\vec{r'})\phi(\vec{r},t) \tag{2.16}$$

where $U(\vec{r},\vec{r'}) = \delta^3(\vec{r}-\vec{r'})[V_C(\vec{r}) + O(\nabla)]$ is the energy independent potential used in its first-order expansion. The potential component V_C is the leading order central potential, but the same study can be performed taking higher order terms in the expansion, thus improving the precision of the final result.
Inverting equation 2.16, the leading order potential is calculated as

$$V_C(\vec{r}) = \frac{1}{2\mu}\frac{\nabla^2\phi(\vec{r},t)}{\phi(\vec{r},t)} - \frac{\frac{\partial}{\partial t}\phi(\vec{r},t)}{\phi(\vec{r},t)} - 2M_N \tag{2.17}$$

obtaining a physical N−N potential based on QCD principles.
The central final N−N potential V_C is calculated and shown in figure 2.4 for different source functions at the variation of a parameter α. From V_C, the expected scattering phase shift for each partial wave is calculated and compared with experimental N−N scattering data.
The HAL QCD method has been applied to many hadron systems, including nuclei, hypernuclei, and hyperons.

2.2.3 N−N potential from Chiral effective field theory

An efficient approach to build up the N−N potential from QCD is to use a chiral Effective Field Theory (χEFT) [43, 44]. In EFT, all the relevant conserved and broken symmetries of QCD at low energy are considered; then, the most general Lagrangian consistent with those symmetries is built, and all relevant Feynman diagrams for each dynamic process are drawn. Each dynamic process is written as expansion in terms of the ratio $\frac{Q}{\Lambda}$, *i.e.* between the soft energy scale, set at the pion mass $Q = m_\pi \approx 140$ MeV, and the hard scale (also called chiral symmetry breaking scale) set as equal to the nucleon mass $\Lambda = m_N \sim 1$ GeV.
The chiral symmetry $SU(2)_R \times SU(2)_L$ is conserved in the limit of mass-less up and down quarks, with right and left-handed components non-mixed. However, the chiral symmetry is explicitly and spontaneously broken by the quark mass term in the Lagrangian in equation 2.5. This generates a Goldstone boson identified with a triplet of pseudoscalar pions. At zero momentum transfer and in the chiral limit ($m_\pi \to 0$), the interactions of the Goldston bosons vanish, justifying the expansion in powers of $\frac{Q}{\Lambda}$.
At low energy, the effective degrees of freedom in QCD are pions and nucleons, and the effective Lagrangian is written as:

$$L_{eff} = L_{\pi\pi} + L_{\pi N} + L_{NN} + ... \tag{2.18}$$

where $L_{\pi\pi}$ describes the dynamics among pions, $L_{\pi N}$, the interaction between a pion and a nucleon, L_{NN} the two-nucleon interaction, and other non-explicit terms involve three or more nucleons and two or more nucleons interacting with one or more pions. Each term is written as an expansion of $\frac{Q}{\Lambda}$, and the theory guarantees that, at a given expansion order, only a finite number of Feynman diagrams exists, making the theory calculable. In this approach, also known as Chiral Perturbation Theory (ChPT), the two- (and three-) nucleon potential can be built.
The N−N interaction potential is composed of a long-range term and a contact term. The long-range potential is built from pion exchanges between the two nucleons:

$$V_{LR} = V_\pi = V_{1\pi} + V_{2\pi} + V_{3\pi} + ... \tag{2.19}$$

where the subscripts indicate the number of exchanged pions. The long-range N−N potential, order by order, in powers of $\frac{Q}{\Lambda}$ is:

$$V_{LO} = V_{1\pi}^{(0)} \tag{2.20}$$

$$V_{NLO} = V_{LO} + V_{1\pi}^{(2)} + V_{2\pi}^{(2)} \tag{2.21}$$

$$V_{NNLO} = V_{NLO} + V_{1\pi}^{(3)} + V_{2\pi}^{(3)} \tag{2.22}$$

$$V_{N^3LO} = V_{NNLO} + V_{1\pi}^{(4)} + V_{2\pi}^{(4)} + V_{3\pi}^{(4)} \tag{2.23}$$

$$V_{N^4LO} = V_{N^3LO} + V_{1\pi}^{(5)} + V_{2\pi}^{(5)} + V_{3\pi}^{(5)} \tag{2.24}$$

where the superscript denotes the order of the expansion, and the potential is built through five orders of chiral effective field theory from the leading order (LO) to the next-to-next-to-next-to-next-to-leading order (N^4LO). Increasing the order of expansion, more pions exchanges enter in the potential (two-pion exchange starts at NLO, three-pion at NNLO, and so on).
The short range N−N potential is described by contact potential V_{ct}, constrained by parity and other invariaces but not by chiral symmetry. Also, the potential V_{ct} is expanded, and the total potential results as the sum of long and short-range potentials.

Among the proprieties of the nuclear interaction, the charge independence is indicated as the independence on the type of involved nucleon, but experimental evidence shows that this invariance is broken. Thus, it must be taken into account. At all orders, the charge-dependence of the pion exchange due to pion-mass splitting, as well as the nucleon mass splitting, is considered using correct mass values of pions and nucleons and obtaining the various charge-dependent N−N potentials (nn, pp or pn).
The potential must be optimized to reproduce phase-shift data from N−N scattering. Therefore, the potential is employed in the fit, trying to reproduce experimental data up to $\sim$ 300 MeV and minimize the χ^2. Starting from pp potential, the np (and then nn) potential is inferred by applying charge dependence and making some adjustments to reproduce scattering phase shifts data. In figure 2.5 the chiral expansion of neutron-proton scattering is fitted to the n-p phase shift data in S, P, and D partial waves, through five expansion orders (LO, NLO...).
N−N data are reproduced at various orders of chiral EFT, and this approach allows to calculate or to improve the quality of measurement of light nuclei proprieties, like deuteron or tritium, listed in table 1.1 [45]. Moreover, knowing the potential, the shape of the deuteron wave function can be calculated with high accuracy, following the calculation discussed in section 2.2.1, giving a more realistic solution.

2.2.4 Argonne ν_{18}

Many different nucleon-nucleon interaction potentials have been built to reproduce correctly the measured scattering phase shifts. One of the most promising potentials is the Argonne ν_{18} [46], a high-quality non-relativistic N−N potential which is explicitly charge-dependent. Argonne ν_{18} is composed of a charge-independent part (the Argonne ν_{14} potential) with the addition of charge-dependent and asymmetric operators and the electromagnetic term, which is the long-range interaction part, containing Coulomb, Darwin-Foldy, vacuum polarization, and magnetic moment terms. The resulting potential is a local potential obtained without the separation in partial waves.
The Argonne ν_{18} potential was directly fitted to the Nijmegen database for np scattering, giving a $\chi^2 \sim 1$ up to 350 MeV [46]. The result of the fit performed for np, pp, and nn, compared to other potentials and phase-shift analysis, is shown in figure 2.6.

Moreover, the Argonne ν_{18} potential was used to calculate the deuteron internal wave

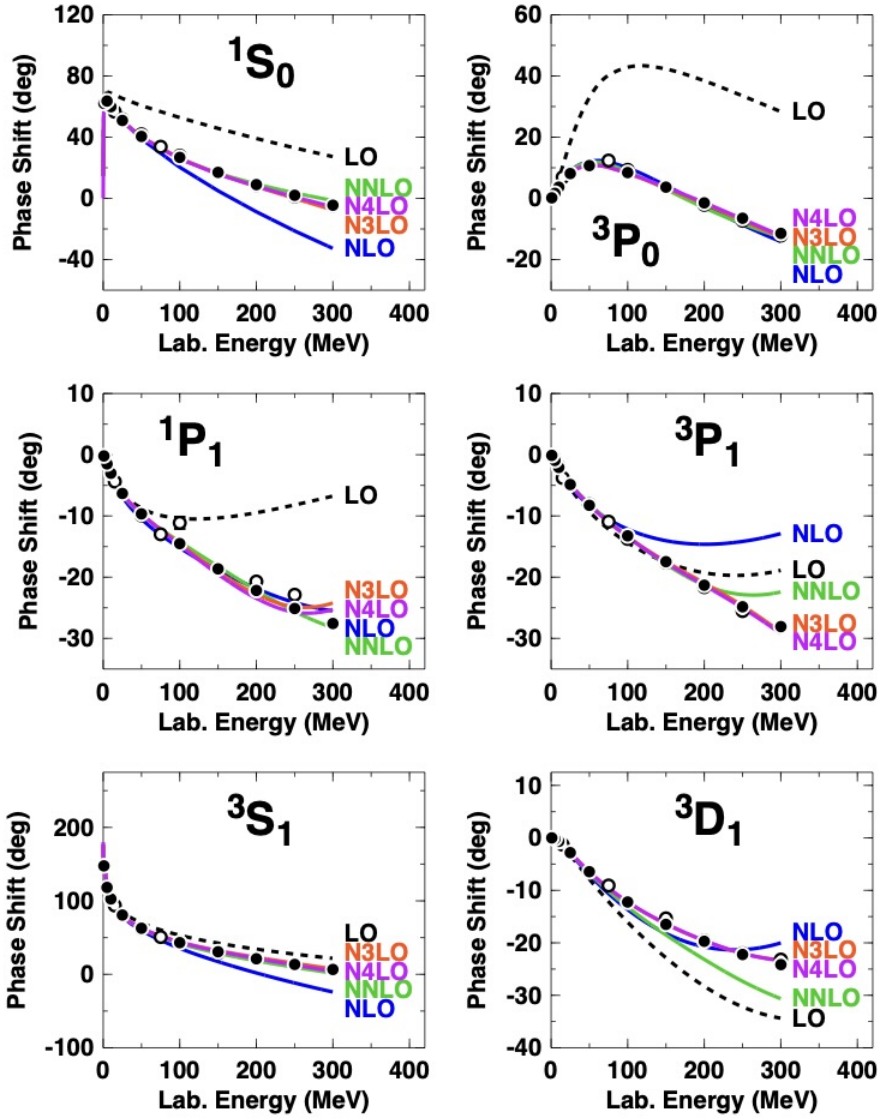

Figure 2.5: Neutron–proton phase shift parameters in S, P, and D partial waves through five orders of expansion from ChPT. The filled and open circles represent the results from the Nijmegen multi-energy np phase-shift analysis [44].

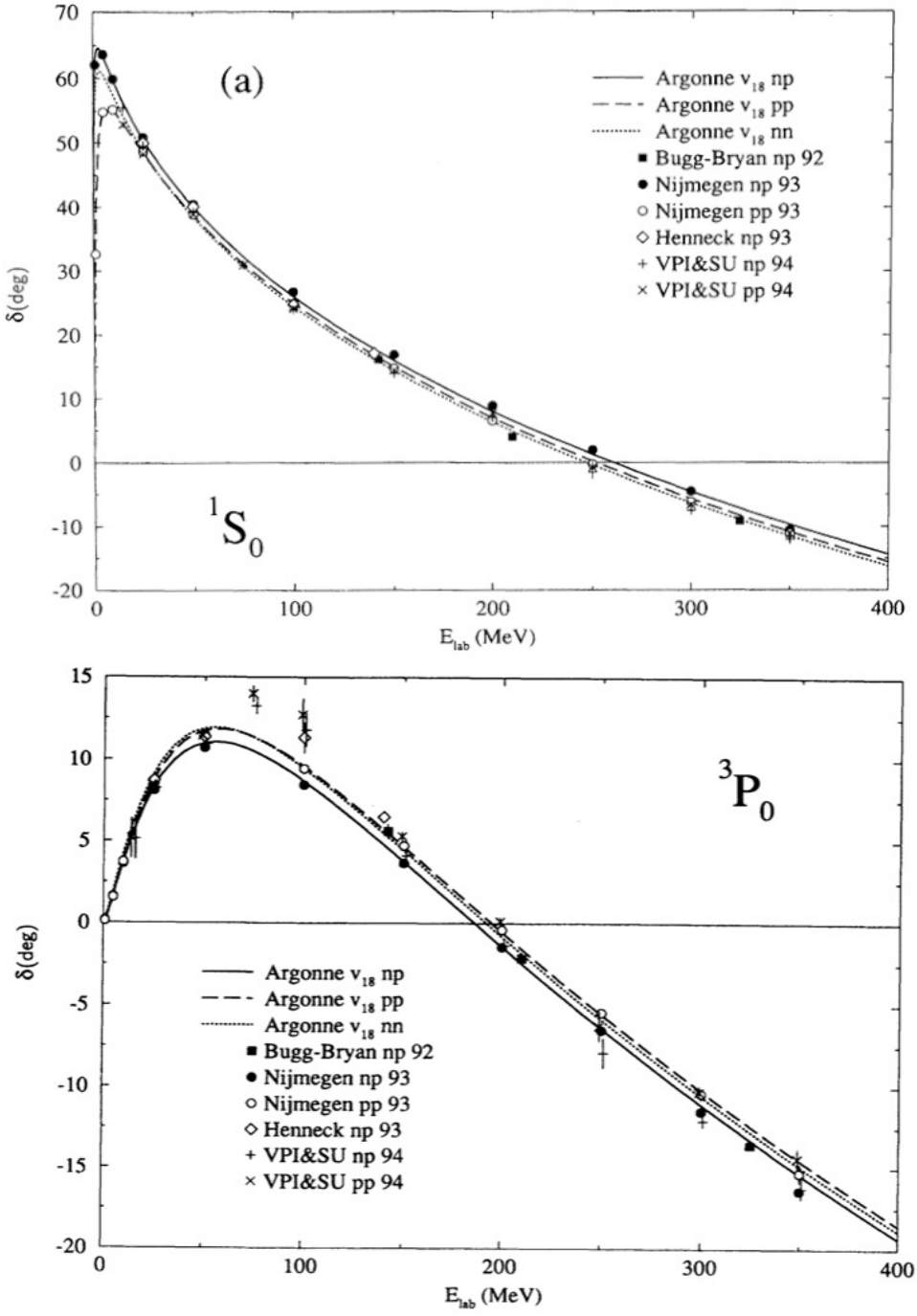

Figure 2.6: Phase shifts in ${}^1S_0$ and ${}^3P_0$ channels for np, pp and nn scattering data from Nijmegen dataset, fitted with charge-dependent Argonne ν_{18} potential [46].

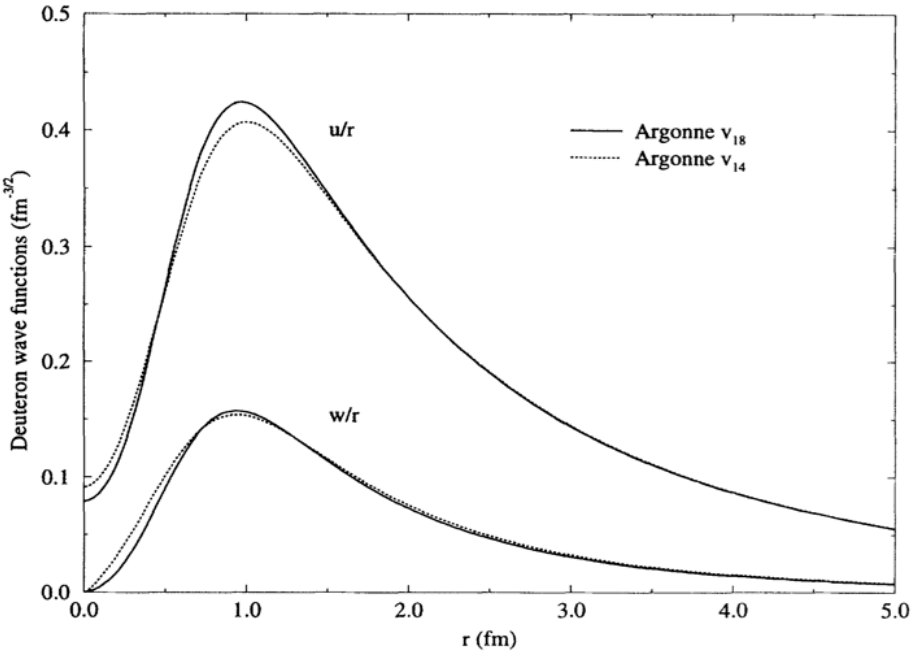

Figure 2.7: The deuteron $u(r)/r$ and $w(r)/r$ wave functions for S and D components, obtained with Argonne ν_{18} and compared to the result of charge-independent Argonne ν_{14} [46].

function for S- and D- components, named respectively $u(r)/r$ and $w(r)/r$, obtaining the result in figure 2.7. The deuteron electromagnetic proprieties have been re-calculated, giving great precision and confirming the power of the Argonne ν_{18} to model N−N interaction successfully.

Chapter 3

Femtoscopy

Femtoscopy is a technique used to access the space-time characteristics of the particle pair emitting region, called the source, by looking at the correlation in momentum between the particles in the pair. The correlation technique is used to explore the proprieties of the source in relation to the final state interaction and the interaction potential among the two particles in the final pair. Using femtoscopy, models for the interaction potential among nucleons, and hadrons in general, can be validated and tested.

The correlation technique was born in astronomy to measure the size of a light-emitting source. It was first used in the 1950s and was based on the "Hanbury-Brown and Twiss" effect (HBT) [47]. The basic idea was to use the fluctuations in the intensity of the detected light to find information about the light emitting source size, whether the source was a single star or a star cluster. This technique was implemented by splitting the light signal from the same source into two independent signals, then detected by two different telescopes. Studying the correlation between two measured intensities, the spatial distribution of the emitting source could be extracted [47]. During the 1960s and 1970s, with the development of particle physics and the realization of the first particle accelerators, the HBT technique was also used to study physics at the subatomic level, maintaining its mathematical formalism but changing its name in femtoscopy where the distances that could be probed were of O(1 fm).

Figure 3.1 is a schematic representation of the femtoscopic principle. Multiple particles are created when two particle beams collide at high energy. Supposing two (or more) of the produced particles are close enough in momentum space, they have a small relative distance $\vec{r}^*$ and small relative momentum $\vec{k}^*$. Also particles can interact, modifying the relative momentum distribution.

In proton-proton or nucleus-nucleus collisions, the source has a spatial extension. Protons (and nuclei) accelerated at high energies collide at a fundamental level resulting in parton-parton scattering. However, due to QCD effects, they hadronize, producing final particles before the detection. The basic idea of femtoscopy[1] is that by studying the

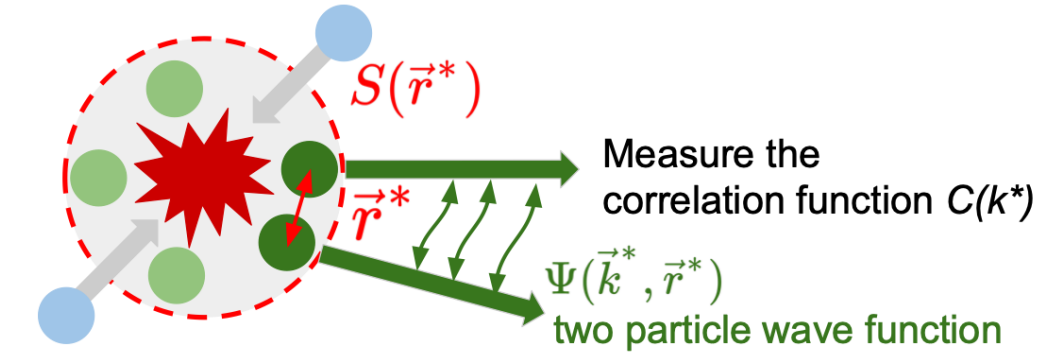

Figure 3.1: In a collision between two particle beams (blue circles), many particles are created and then emitted from the emission region described by the spatial distribution $S(r^*)$. Emitted particles with small relative momentum k^* (green circles) interact with each other in the final state at a distance r^*, resulting in the two-particle wave function [48].

interference due to the final state interaction of the emitted particles, it is possible to obtain information about the spatial distribution of final state particles and extract the size r_0 of the emission region. This technique is therefore of interest for the study in this thesis because the source size is a fundamental parameter for the correlation function and once extracted, it can be used to validate the coalescence model and thus to model the production mechanism of (anti)nuclei, as discussed in section 1.3.
In this chapter details of the femtoscopic technique are presented, with particular reference to its applications to the study of hadron-hadron interactions at the LHC energies, including to the characterization of the proton source in pp collisions.

3.1 The correlation function

The main observable in femtoscopy is the correlation function that quantifies the particle correlation in momentum.
The correlation function $C(\vec{k}^*)$ depends on the relative momentum of the particles forming a pair, defined as $\vec{k}^* = \frac{1}{2}|\vec{p_2}^* - \vec{p_1}^*|$, with $\vec{p}^*_{1,2}$ that is the particle momenta measured in the pair rest frame.
The two particle theoretical correlation function $C(\vec{k}^*)$ is rigorously defined as:

$$C(\vec{k}^*) = \int S(\vec{r}^*, r_0) \left|\Psi(\vec{r}^*, \vec{k}^*)\right|^2 \mathrm{d}^3\vec{r}^* \tag{3.1}$$

[1]Another possible approach is the so-called non-traditional femtoscopy, which aims to study the final state interaction and the interference wave function, assuming a given spatial distribution for the emitting source.

where:

- $\vec{r^*}$ and $\vec{k^*}$ are the relative distance and momentum of the particle pair measured in the pair reference frame, respectively;
- $S(\vec{r^*}, r_0)$ is the so-called source function, representing the probability density function to find two particles at a relative distance $\vec{r^*}$;
- $\Psi(\vec{r^*}, \vec{k^*})$ is the final state wave function of the pair; the modulus square in equation 3.1 is the probability of finding two particles with a relative distance $\vec{r^*}$ at a relative momentum $\vec{k^*}$.

The equation 3.1 is also called the "Koonin-Pratt" relation [49]. Being a probability density function, $S(\vec{r^*}, r_0)$ must be normalized such as:

$$\int S(\vec{r^*}, r_0)\, \mathrm{d}^3\vec{r^*} = 1. \tag{3.2}$$

It is challenging to model $S(\vec{r^*}, r_0)$ exactly because of the limited knowledge of the hadronization process and QCD effects at low $\vec{k^*}$. Assuming a source with a spherical symmetry, the simplest model for the spatial distribution is the Gaussian profile:

$$S(\vec{r^*}, r_0) = \frac{1}{(4\pi r_0^2)^{\frac{3}{2}}} \exp\left(-\frac{\vec{r^*}^2}{4r_0^2}\right) \tag{3.3}$$

with the source size r_0, being the standard deviation of the distribution.

The theoretical correlation function, defined in equation 3.1, and in particular the pair wave function $\Psi(\vec{r^*}, \vec{k^*})$, depend on the interacting potential $V(r^*)$, as illustrated in figure 3.2. The correlation function can be greater than 1 if $V(r^*)$ is attractive, lower than 1 if $V(r^*)$ is repulsive, or equal to 1 if there is no interaction among particles in the pair, as shown in the left plot of figure 3.2. At a high relative distance r^* between the particles in the pair, the interaction does not occur, and $V(r^*)$ is equal to 0 in any case. The presence of a bound state makes the amplitude squared of the wave function to increase at small distances leading to a correlation function above 1 for small r_0. On the other hand, for higher source size only the asymptotic part of the wave function is included in the correlation function, bringing it below 1.
Particles decouple quickly at high k^* without experiencing final state interaction, leading to a correlation function tending to 1, as shown in the right plot of figure 3.2. This is expressed by the condition:

$$\lim_{\vec{k^*}\to\infty} C(\vec{k^*}) = \int S(\vec{r^*}, r_0) \left|\Psi(\vec{r^*}, \vec{k^*})\right|^2 \mathrm{d}^3\vec{r^*} = 1 \tag{3.4}$$

The behavior of the correlation function when $\vec{k^*} \to \infty$ is also due to the wave function of the particle pair that, in this scenario, becomes a free wave, resulting in the correlation

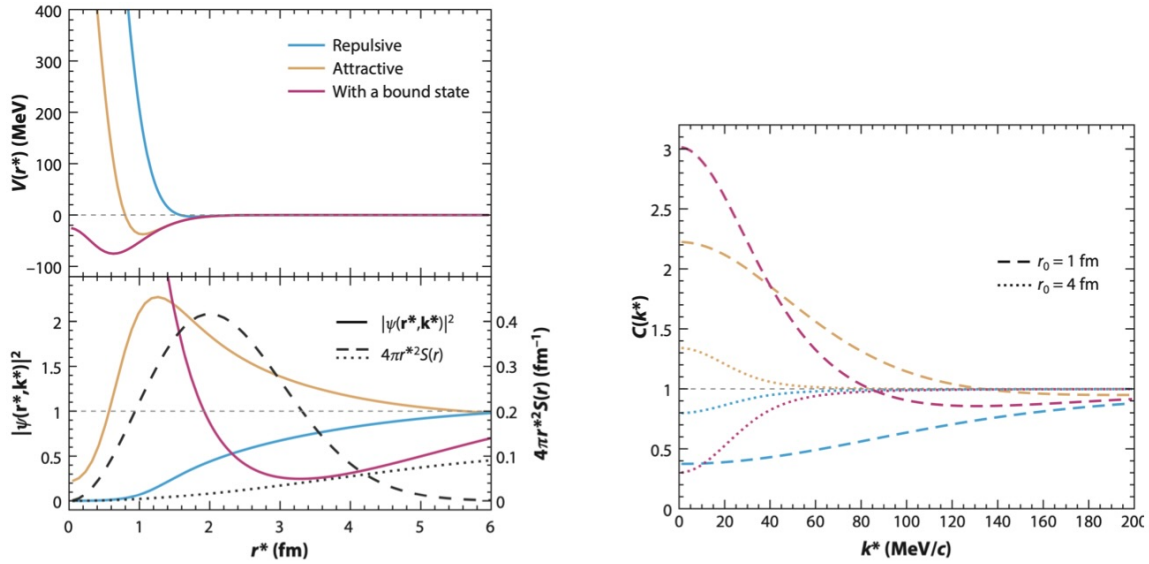

Figure 3.2: On the left up: potential $V(r^*)$ as a function of the distance between particles r^* in case of repulsive (blue) or attractive (yellow) interaction, or of a bound state (red). On the left down: squared amplitude for the final pair wave function $\left|\Psi(\vec{r^*}, \vec{k^*})\right|^2$ with respect to r^*, for the different potentials shown above and calculated solving the Schrödinger equation. The profile of the emitting source for 1 fm (dashed black line) and 4 fm (dotted black line) is drawn in the same plot. On the right: correlation function $C(k^*)$ for each potential represented on the left, and measured for two different source sizes, $r_0 = 1$ fm (dashed lines) and 4 fm (dotted lines) [50].

function approaching unity.

The correlation function has also a statistical definition:

$$C_{stat}(\vec{p}_1, \vec{p}_2) = \frac{P(\vec{p}_1, \vec{p}_2)}{P(\vec{p}_1)P(\vec{p}_2)} \tag{3.5}$$

where $P(\vec{p}_1, \vec{p}_2)$ at the numerator is the probability of detecting simultaneously particles 1 and 2 with momenta equal to $\vec{p}_1$ and $\vec{p}_2$ respectively; at the denominator, the probability $P(\vec{p}_1)$ and $P(\vec{p}_2)$ of emitting single particles with momentum $\vec{p}_1$ and $\vec{p}_2$ respectively for particle 1 and particle 2 are multiplied. The numerator and the denominator can be expressed in terms of the particle momentum distributions and energies of particle 1 and 2, $E_{1,2}$ [51] as

$$P(\vec{p}_1, \vec{p}_2) = E_1 E_2 \frac{d^6 N}{d^3\vec{p}_1 d^3\vec{p}_2} \tag{3.6}$$

$$P(\vec{p}_{1,2}) = E_{1,2} \frac{d^3 N}{d^3\vec{p}_{1,2}} \tag{3.7}$$

Experimentally, the correlation function is measured as the relative momentum-dependent ratio between the distribution of correlated pairs from the same event $SE(\vec{k}^*)$ and of uncorrelated pairs from different events $ME(\vec{k}^*)$:

$$C(\vec{k}^*) = N(\vec{k}^*) \frac{SE(\vec{k}^*)}{ME(\vec{k}^*)}. \tag{3.8}$$

Here, $SE(\vec{k}^*)$ is obtained by pairing all identified particles of interest in each event, while $ME(\vec{k}^*)$ is obtained by pairing identified particles of interest produced in different (mixed) events, and thus physically uncorrelated. The $ME(\vec{k}^*)$ acts as a reference distribution to eliminate the contribution of uncorrelated pairs accidentally included in the same event sample by the combinatorial procedure. The $N(\vec{k}^*)$, acting as a normalization factor for the ratio, considers the finite experimental resolution and corrections and is used to normalize the ratio.

In order to extract the source size r_0, the experimental correlation function, measured according to equation 3.8, must be compared to the theoretical one in equation 3.1. To compare means that the fit of the measured correlation with the theoretical function is performed, and r_0 is obtained as a fit parameter.
A key ingredient for the fit is the calculation of the pair wave function $\Psi(\vec{k}^*, \vec{r}^*)$, solving the Schrödinger equation. The solution can be obtained using numerical tools, like the Correlation Analysis Tool using the Schrödinger equation (CATS, see sec. 3.3), or analytically, by applying the Lednicky-Lyuboshits formalism [52, 53]. The Lednicky-Lyuboshits formalism provides an analytical and approximated solution to the Schrödinger equation

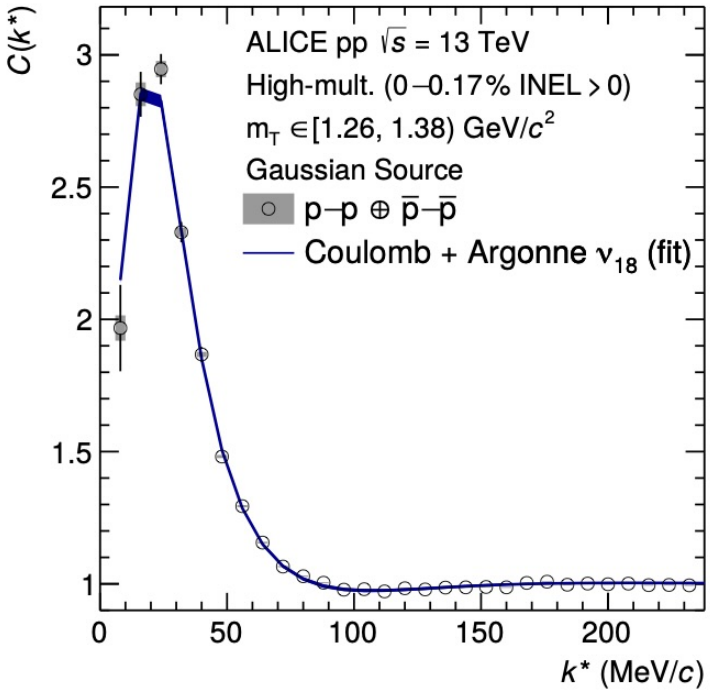

Figure 3.3: Correlation function for p−p⊕p̄−p̄ pairs measured by ALICE in pp collisions at $\sqrt{s} = 13$ TeV using Run 2 data. The band represents the fit of the correlation function performed by CATS, using the Coulomb and the Argonne ν_{18} potentials to model the interaction among (anti)proton pairs [54].

for a two-body system. The model is limited by the poor knowledge of the strong potential and the capability to compute analytical solutions for second-order differential equations. Knowing that the strong potential has short range, particles at large distances can only experience Coulomb force if charged. In the asymptotic regime, namely outside the strong potential range and far from the scattering center, a solution is analytically computed approximating the effect of the strong interaction as a phase shift in the final state wave function. Of course, this is not exact and valid only in a limited regime, as discussed in sec. 2.2.3.
The proton−proton correlation analysis has been measured using high multiplicity pp collisions at $\sqrt{s} = 13$ TeV by ALICE [54], and the source size for the proton pair extracted by CATS employing the Argonne ν_{18} and the Coulomb potentials. The source radius $r_0 \in [0.85, 1.3]$ fm for $m_T \in [1.1, 2.2]$ GeV/c^2, and the result is reported in figure 3.3.

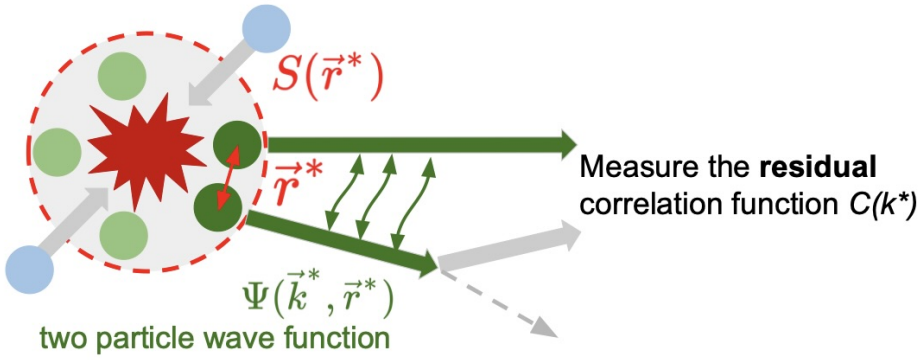

Figure 3.4: Representation of the femtoscopic technique in case of a resonance decay. The correlation function is measured for daughter particles, and the femtoscopic signal can be contaminated [48].

3.2 Residual correlation

In the experimental femtoscopic analysis, corrective factors must be included in the model to produce the final and more accurate result.
Ideally, only genuine particle and antiparticle pairs, thus composed of correctly identified particles and antiparticles produced in the primary collision, should be considered. Only in this case the correlation function $C_{\text{genuine}}(\vec{k}^*)$ corresponds to the final state interaction under study.
In every practical case of experimental analysis, the selected sample includes:

- misidentified (anti)particles,
- feed-down (anti)particles from strong decays,
- feed-down (anti)particles from weak decays,
- secondary particles produced in the detector material.

The contribution of secondaries from material affects only the particle sample, because antiparticles cannot be produced in the material, composed by matter.
In the case of feed-down from weak decays, *i.e.* particles decaying weakly into the species of interest, these non-genuine contributions produce changes in the correlation functions and in the predictive capabilities of the model because the decay point is displaced from the primary vertex, and the relevant final state interaction for correlations involves primary (anti)particles before the decay. This effect is graphically explained in figure 3.4. The decay of strong resonances with a very short lifetime ($c\tau \sim 10$ fm) distorts the effective source function, leading to a non-Gaussian tail.

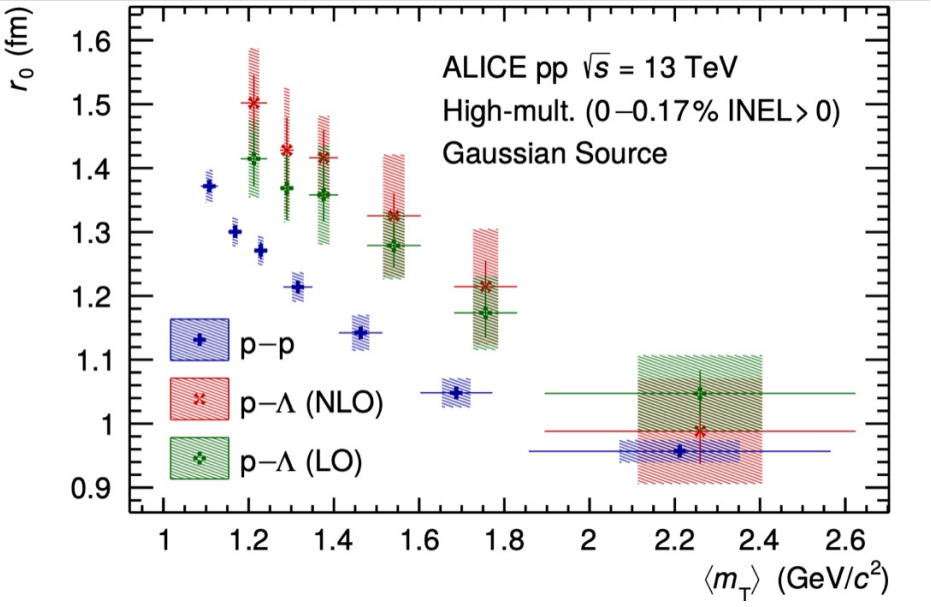

Figure 3.5: Source radius r_0 as a function of the average transverse mass $\langle m_T \rangle$ assuming a purely Gaussian source. The blue points come from the fit of the p–p correlation function with the strong Argonne ν_{18} potential. The green and red points are obtained from p-Λ correlation function fitted with strong χEFT LO and potentials [54].

If the genuine correlation is assumed to be described by a Gaussian source as in equation 3.3, the source radius r_0 is measured as a function of the average transverse mass $\langle m_T \rangle = \sqrt{k_T^2 + m^2}$, where m is the average mass of the particle pair and $k_T = |\vec{p}_{T1} + \vec{p}_{T2}|/2$, as in figure 3.5 for p−p and p−Λ correlations measured by the ALICE Collaboration in pp collisions at $\sqrt{s} = 13$ TeV.

The measurements indicate different effective sources for protons and Λ, however, the presence of strong resonance must be accounted for. Figure 3.6 describes the modification of r^*_{core} into the effective source radius accounting for delayed emission from resonances:

$$\vec{r^*} = \vec{r^*_{core}} - \vec{s^*_{res,1}} + \vec{s^*_{res,2}} \tag{3.9}$$

where $\vec{s^*_{res}}$ is the distance covered by the parent resonance before the decay.

The described effect of short-lifetime resonances is reflected in an increase of the source size and in the addition of an exponential tail to the Gaussian core given by primary emitted particles. Including the non-Gaussian halo, the effective source function profile is shown in figure 3.7. This profile is fed to the software CATS used to perform the fit of the $C(k^*)$ and to extract r_0 shown in figure 3.3.

The resulting r^*_{core} is more compact, and this is reflected in a different dependence from $\langle m_T \rangle$, as shown in figure 3.8. This result should be compared with the plot in figure 3.5. Figure 3.8 exhibits a common $\langle m_T \rangle$ scaling of the source radius for different particle

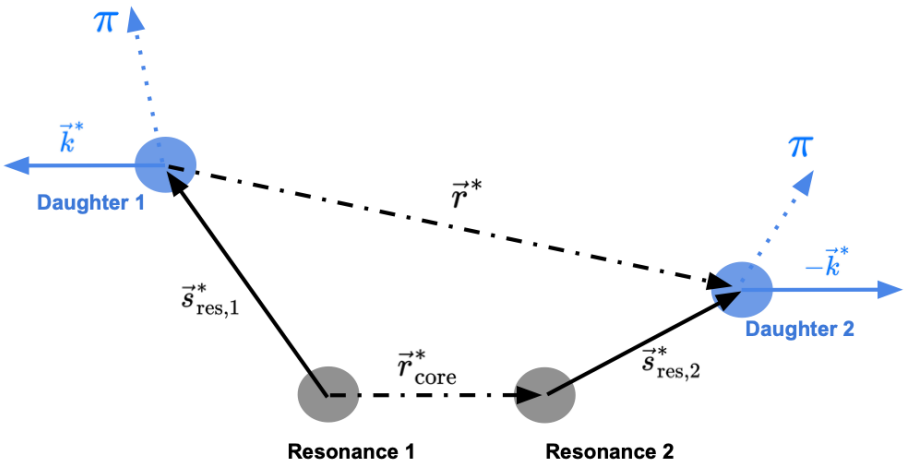

Figure 3.6: Graphical representation that shows how the presence of at least one resonance (grey disks) in the primordial state affects and modifies the r^*_{core} into the effective source radius r^*, measured in the rest frame of the decay products (blue disks) [54].

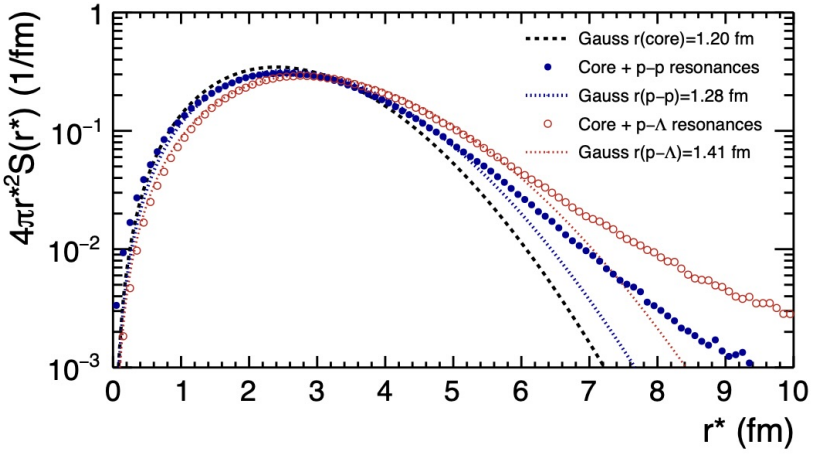

Figure 3.7: Source function profile as depending on the effective source size r^*, considering different source sizes and including strongly-decaying resonances. The profile is composed of a Gaussian core, plus a non-Gaussian halo due to resonances [54].

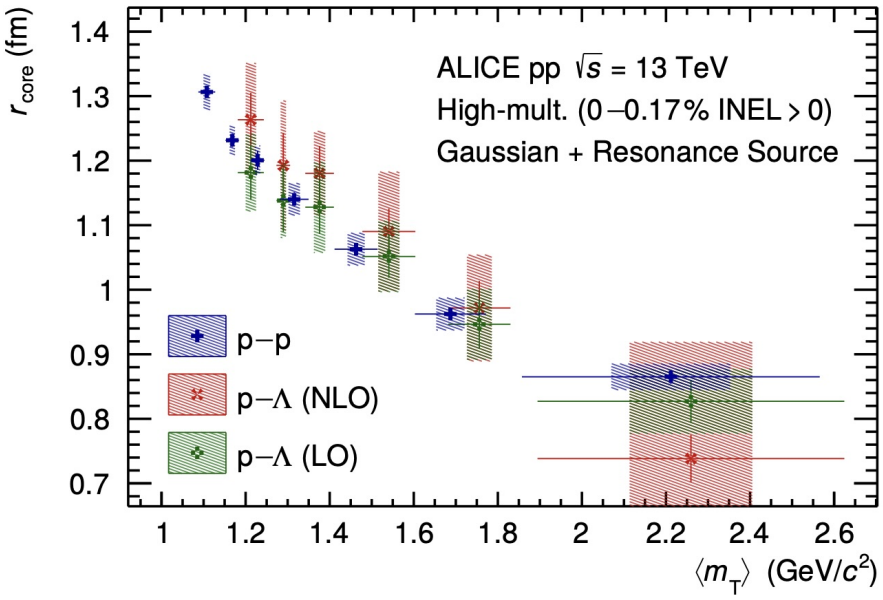

Figure 3.8: Source radius r_0 as a function of the average transverse mass $\langle m_T \rangle$ assuming a Gaussian source and including the effect of resonance decay. The blue points come from the fit of the p–p correlation function with the strong Argonne ν_{18} potential. The green and red points are obtained from p-Λ correlation function fitted with strong χEFT LO and potentials [54].

pairs. This feature demonstrates the existence of a common baryon source for p, $\bar{p}$, Λ, and $\bar{\Lambda}$ [54].
In order to consider all the discussed effects, the model correlation function is composed of genuine and non-genuine contributions, each weighted by a λ parameter as:

$$C(k^*) = 1 + \lambda_{\text{genuine}} \cdot (C_{\text{genuine}}(k^*) - 1) + \sum_{ij} \lambda_{ij} \cdot (C_{ij}(k^*) - 1) \tag{3.10}$$

where i and j denote all possible impurities and feed-down contributions. Correlation functions C_{ij} are relative to each contribution and are calculated separately. λ_{ij} is evaluated in equation 3.11 knowing single particle purity $\mathcal{P}_{i,j}$ and the fraction $\mathcal{F}_{i,j}$ of feed-down particles as

$$\lambda_{ij} = \mathcal{P}_i \times \mathcal{F}_i \otimes \mathcal{P}_j \times \mathcal{F}_j. \tag{3.11}$$

3.3 CATS

CATS [55] is the short name of a new standalone analysis framework called "Correlation Analysis Tool using the Schrödinger equation". CATS computes an exact and

numerical solution of the full Schrödinger equation and evaluates the two-body correlation function, corresponding to a given choice of the interaction potential. Then, the analysis framework performs the fit of the obtained theoretical correlation function to the measured data, extracting the source size as a fit parameter.
In order to evaluate the final state wave function and the theoretical correlation function, CATS uses a local real potential for two strongly interacting charged hadrons.
The solved Schrödinger equation is the time-independent equation in the presence of a central potential $V(r)$, and the problem is reduced to solve the radial equation 2.12, according to the calculations discussed in section 2.2.

For p−p correlations, Argonne ν_{18} (see sec. 2.2.4) is the most realistic potential to model the strong interaction among two nucleons. The total p−p interaction is made of the Argonne ν_{18} plus a repulsive Coulomb potential (the charge is the same in p−p and $\bar{\text{p}} - \bar{\text{p}}$).
The source employed in CATS is parameterized using a Gaussian distribution.
The correlation function used in the fit is not the theoretical one, but it appears:

$$C_{fit}(k^*) = C_{model}(k^*) \cdot C_{non-femto}(k^*) \tag{3.12}$$

therefore as the product of $C_{model}(k^*)$, which involves the theoretical-genuine correlation function for the particle pair, the contributions of feed-down particles, secondaries produced by the material, impurities, and non-Gaussian corrections, as defined in equation 3.10, and of $C_{non-femto}(k^*)$, which incorporates non-femtoscopic effects at high k^*, such as jets in the high momentum region able to modify the experimental correlation function profile. In CATS, the non-femtoscopic effects are described as the linear function $C_{non-femto}(k^*) = b \cdot (1 + ak^*)$. The slope a and the normalization b are evaluated as free fit parameters. The fit quality is measured through the χ^2 parameter, divided by the number of degrees of freedom (ndf). In CATS, the $\lambda_{genuine}$, defined in equation 3.10 as the fraction of genuine p−p pairs, is a fixed parameter that must be set before the fit. As an example, in the analysis of p−p correlations using pp collision data at $\sqrt{s} = 13$ TeV by the ALICE experiment [54], $\lambda^{pp}_{genuine}$ have been estimated at the ∼70% while in p-d correlation $\lambda^{pd}_{genuine}$ ∼83% [56] as the average of particle $\lambda^{xy}_{genuine}$ and antiparticle $\lambda^{\bar{x}\bar{y}}_{genuine}$ parameters. In the same analysis secondary feed-down protons are for the 70,7% p_Λ and for the 29.3% p_{Σ^+} generated respectively in Λ or Σ^+ baryons weak decays. In addition, protons can also be produced in the interaction of a primary particle with the material of a detector producing secondary particles (protons), or impurities can be misidentified with true protons.

For this thesis work and prior to approaching the analysis of the proton−deuteron correlation, CATS was used to fit the p−p correlation function in pp collisions at $\sqrt{s} = 13$ TeV, and reproduce the measurement of the radius of the proton pair source, to acquire familiarity with the framework. The result, obtained employing the Argonne

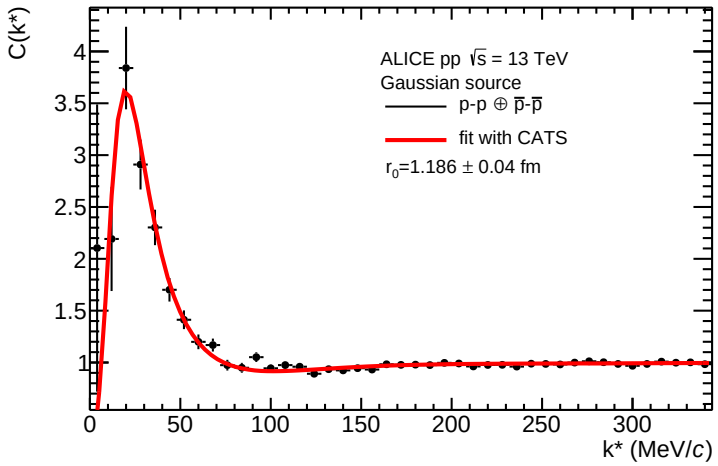

Figure 3.9: Proton−proton correlation function calculated using ALICE data of pp collisions in Run2. Experimental data are fitted with CATS, and the source radius is calculated under the Gaussian source assumption and using Argonne ν_{18} plus Coulomb potential.

ν_{18} plus the Coulomb potential to model the interaction among the particles, is shown in figure 3.9. In the fit $\lambda_{genuine}$ is set at 82.5%. The differences between the analysis presented here and in [54] are due to the different data sets used, the corrections on the purity and on the momentum resolution, which are not fully included in my analysis. The extracted source size measures $r_0 = 1.19 \pm 0.04$ fm, with a $\chi^2/\text{ndf} = 32.04/41 = 0.78$, with 41 degrees of freedom. The fit gives the slope $a = 1.431 \cdot 10^{-4} \pm 6.007 \cdot 10^{-5}$ 1/MeV and the normalization $b = 0.958 \pm 0.014$, and the range of the fit is $0 < k^*(MeV/c) < 350$. This result is consistent with the published one in figure 3.3, which is obtained using CATS as well with the strong Argonne ν_{18} potential. In the published analysis the $\lambda_{genuine} = 66.7\%$. This value is different from the one used to reproduce the analysis because corrections in momentum resolutions are not applied, and contributions from misidentified particles are not considered.

Chapter 4

ALICE

A Large Ion Collider Experiment, also known by the acronym ALICE, is the Large Hadron Collider (LHC) experiment dedicated to heavy-ion collisions, located 56 m underground at the collision point 2 of the LHC.
It has been proposed to study the properties of the strong interaction and characterize the Quark-Gluon Plasma (QGP), a very hot and dense state of matter composed of deconfined quarks and gluons. The QGP is produced in heavy-ion collisions at high energy, and it has been suggested to exist in the first moments of the universe.
The ALICE physics program is not only devoted to studying heavy-ion collisions, like between lead nuclei (Pb-Pb), but also includes proton-proton (p-p) collisions.
Due to its broad physics program and specific goal, ALICE is the unique experiment at the LHC equipped with a complex particle identification system, an excellent tracking system down to very low momenta, that can work in a high multiplicity environment.

ALICE has been operating since 2009 when the LHC Run 1 (2009-2013) started with p-p collisions at the energy of the center of mass $\sqrt{s} = 0.9$ TeV. During Run 1, p-p collisions at $\sqrt{s} = 2.76$ TeV, 7 TeV, and 8 TeV took place. ALICE collected data during Run 2 (2015–2018) and Run 3 (2022-2025) with p-p collisions at $\sqrt{s} = 5.02$ TeV and 13 TeV in Run 2 and $\sqrt{s} = 13.6$ TeV in Run 3. Also Pb-Pb data was collected in 2010 and 2011 at the energy of the center of mass in Nucleus-Nucleus collisions $\sqrt{s_{NN}} = 2.76$ TeV, and in 2015 and 2018 at $\sqrt{s_{NN}} = 5.02$ TeV; during Run 3 Pb-Pb collisions at $\sqrt{s_{NN}} = 5.36$ TeV are scheduled by the end of 2023. Other collision systems, such as p-Pb collisions, were studied in 2013 and 2016 at $\sqrt{s_{NN}} = 5.02$ and 8.16 TeV, respectively.

The details of the ALICE detector, hereafter called ALICE1, are in ref. [57]. During the Long Shutdown 2 (2019-2021), the detector was upgraded, and the new ALICE for Run 3, hereafter called ALICE2, is shown in figure 4.1.
For Run 3 and Run 4, the ALICE collaboration aims to measure hadrons with heavy-flavor quarks (as charm and bottom) and the thermal radiation emitted by QGP by studying dielectron pairs. Moreover, the ALICE upgrade enables new high-precision measurements in jet quenching phenomena, production of light (anti)nuclei, momentum

correlation between hadrons, and the characterization of collective effects in high multiplicity p-p collisions.

The ALICE detector weighs 10 000 tonnes, is 26 m long, 16 m high, and 16 m wide. It is built with a central symmetry around the beam pipes (red horizontal line in figure 4.1). The beam axis corresponds to the z-axis in the detector reference frame, and the transverse plane is the xy-plane.
The detector is composed of many sub-detectors able to characterize the main properties of an event.
A central barrel, a forward Muon Spectrometer, and other smaller detectors compose the ALICE detector. The central barrel is inside a solenoidal magnet providing a uniform field of B = 0.5 T along the beam direction; the magnet (in red in figure 4.1), inherited from the former LEP experiment L3, surrounds the whole apparatus that includes:

- Inner Tracking System (ITS) (see section 4.1);
- Time Projection Chamber (TPC) (see section 4.2);
- Time of Flight (TOF) (see section 4.3);
- Transition Radiation Detector (TRD), used in track reconstruction and momentum determination of charged particles in $|\eta| < 0.9$; it supports event trigger, and it is also able to identify electrons and suppress pion background;
- Electromagnetic Calorimeter (EMCal), used to detect electrons and photons produced in heavy-flavor hadron decays or neutral mesons; it also provides some trigger levels;
- Photon Spectrometer (PHOS), a precise electromagnetic calorimeter with high energy and spatial resolution for photons;
- High Momentum Particle Identification Detector (HMPID), a ring-imaging Čherenkov detector used to identify hadrons at large transverse momentum over a limited acceptance.

In the forward region, there is the Muon Spectrometer: it includes an absorber to filter the background, tracking chambers located before, inside, and after a dipole magnet and trigger chambers. The system, within the acceptancy region, $-3.6 < \eta < -2.45$, can identify muons produced in hadronic decays with high pointing resolution (~ 100 μm) using silicon pixel sensors.
Finally, the Zero Degree calorimeters (ZDC) are used to determine the centrality of the collisions, and the Fast Interaction Trigger (FIT), a scintillator-based system, is used as interaction trigger, online luminometer, initial indicator of the vertex position, and

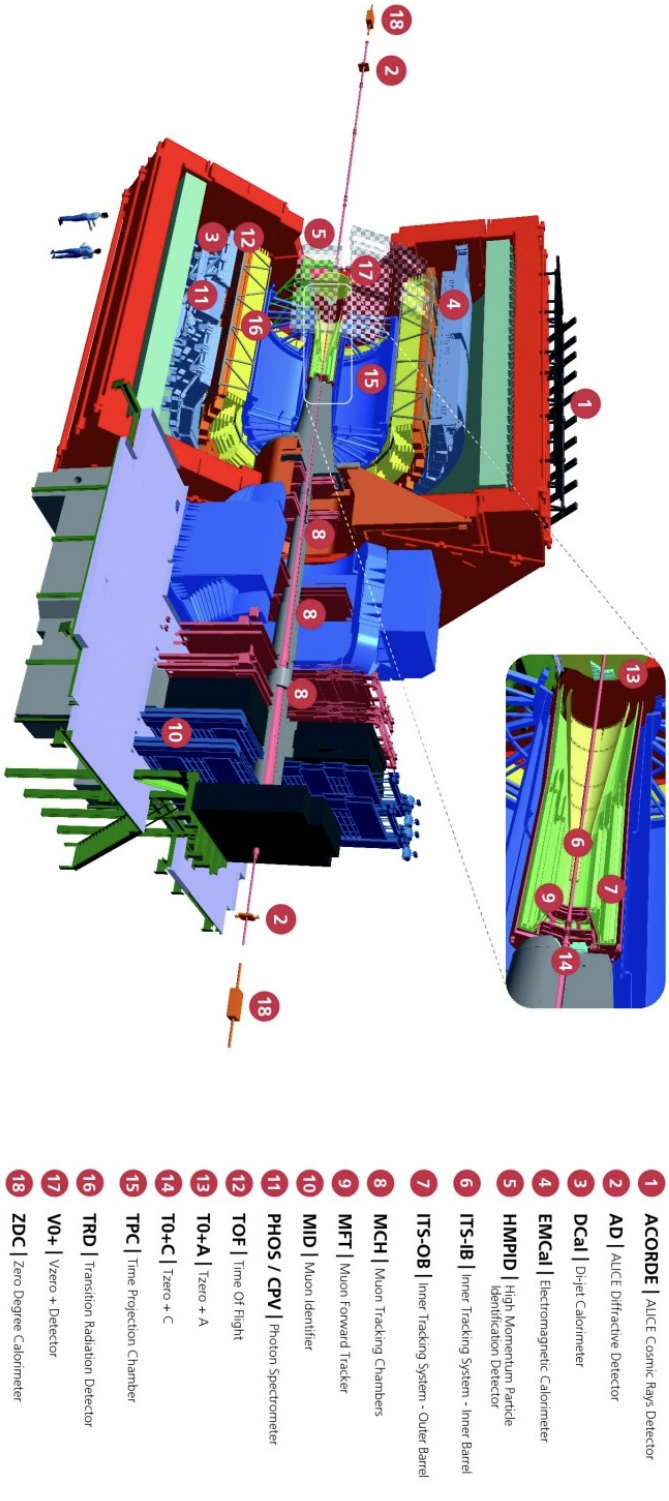

Figure 4.1: The ALICE detector during Run 3.

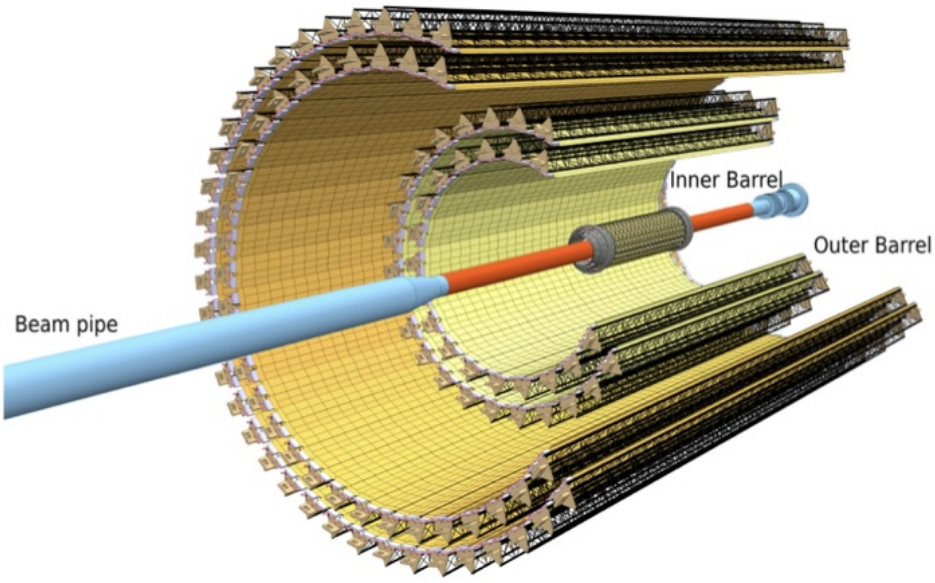

Figure 4.2: Schematic view of the Inner Tracking System during Run 3.

forward multiplicity counter. The FIT detector consists of two Cherenkov radiators, FT0-A and FT0-C, placed on opposite sides at almost 3.3 m from the collision point.
A complete overview of sub-detectors in ALICE and their upgrade can be found in the upgrade letter of intent [58] and in [59], while in this thesis, I focus on the main detectors relevant for my analysis work.

4.1 Inner Tracking System

The Inner Tracking System (ITS) [60] is the first detector crossed by a particle produced in the collision vertex. The ITS is located in the central barrel, covering the pseudorapidity range of $|\eta| < 1.3$, and is the closest detector to the interaction point. The main goal is to reconstruct the primary vertex of the collision, track and identify low momentum particles, and reconstruct secondary vertices due to the weak decays of primary particles (typically with a lifetime $\tau \sim$ cm/c).
The upgraded ITS (ITS2), in figure 4.2, is thinner and lighter than the previous ITS1, and a brief comparison between ITS1 and ITS2 is in table 4.1. ITS2 is composed of seven concentric layers subdivided into the Inner Barrel, composed of the three innermost layers, and the Outer Barrel, composed of the four outermost layers.
All the layers are equipped with silicon ALPIDE Monolithic Active Pixel Sensors (MAPS) (chapter 2.3 of ref. [59]). The total area instrumented with silicon pixels is extended for

	ITS1	ITS2
Technology	Hybrid pixel, strip, drift	MAPS ALPIDE
Readout Rate	1 kHz	50 kHz (Pb-Pb)
		400 kHz (p-p)
No. of layers	6	7
Radius of innermost layer	39 mm	22.4 mm
Pointing resolution	∼240 μm (z)	∼50 μm (z)
(pT = 500 MeV/c)	∼120 μm (rϕ)	∼40 μm (rϕ)
Material budget	1.1% X_0	0.36% X_0 (Inner Barrel)
		1.1% X_0(Outer Barrel)

Table 4.1: Comparison between the main proprieties of ITS1 and ITS2 [60].

about 10 m^2, making the ITS2 the largest MAPS silicon tracker ever built for a high-energy physics experiment.
Using fast digital pixel sensors allows for an increase of the readout rate by about 100 times with respect to ITS1, reaching a readout rate greater than 50 kHz in Pb–Pb collisions and 400 kHz in p-p collisions. Increasing the readout rate improves the statistical precision of measurements, allowing for background reduction.
Almost 12.5 billion ALPIDE pixels with a size of 27 $\times$ 29 μm^2 are used in the ITS2, and the small dimensions result in an increased granularity and segmentation.
The material budget and the multiple scattering effects are reduced to 0.36% X_0 and to 1.10% X_0 in the innermost and outermost layer, respectively, by making use of pixels instead of strip detectors.
The upgrade's main goal for the ITS was to improve the resolution of the impact parameter and the collision vertex position. This goal was realized by reducing the distance of the first layer of the Inner Barrel from the beam axis to only 22.4 mm (instead of 39 mm in ITS1). The resulting spatial resolution on the impact parameter was reduced to 5 μm $\times$ 5 μm (z $\times$ rϕ), as shown in figure 4.3, while the comparison between impact parameter resolutions of ITS1 and ITS2 is in figure 4.4.

The ITS2 design improves the tracking efficiency from 60% to 90% and the transverse momentum resolution for low momenta, reaching excellent tracking capabilities down to $p_T \sim$ 120 MeV/c (chapter 3.2 in ref. [59]).

4.2 Time Projection Chamber

The Time Projection Chamber (TPC) [61], in figure 4.5, is a gas detector used in ALICE for tracking and particle identification. The main goal of the TPC is to measure the energy lost by a charged particle in the detector; knowing the energy loss, the mo-

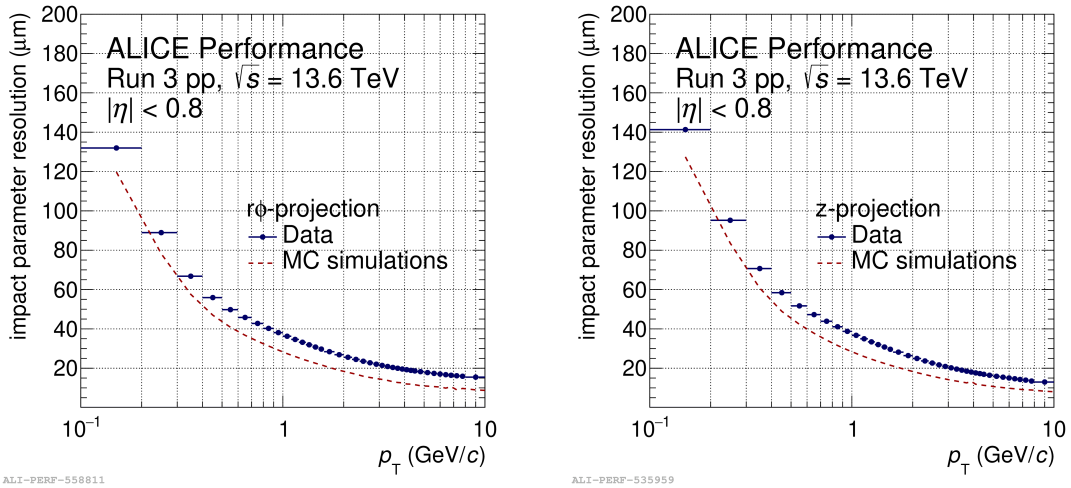

Figure 4.3: Resolution on the impact parameter as a function of the transverse momentum, in transverse rϕ (left panel) and longitudinal z (right panel) planes, measured in pp collisions at $\sqrt{s}$=13.6 TeV. Data (in blue) are compared with Monte Carlo simulations (in red).

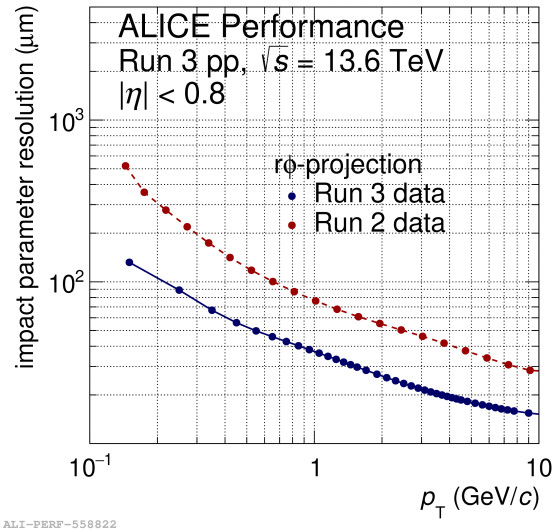

Figure 4.4: Impact parameter resolution in $r\phi$ vs. p_T comparison between data from pp collisions at $\sqrt{s}$=13.6 TeV in Run 3 data (blu) and $\sqrt{s}$=13 TeV from Run 2 data (red).

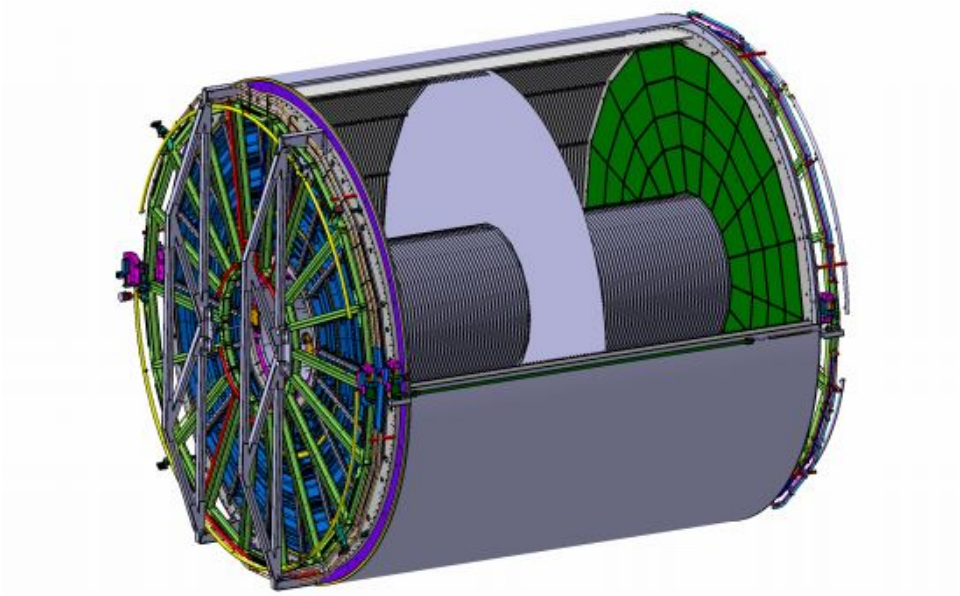

Figure 4.5: The Time Projection Chamber in ALICE during Run 3 (chapter 3.4 in ref. [59]).

mentum, and the charge of the particle can be inferred, contributing to charged particle identification.

Indeed, the measured energy loss is parameterized by the Bethe-Bloch formula:

$$-\langle\frac{dE}{dx}\rangle = Kz^2\frac{Z}{A}\frac{1}{\beta^2}\left[\frac{1}{2}\ln\frac{2m_ec^2\beta^2\gamma^2T_{\max}}{I^2} - \beta^2 - \frac{\delta(\beta\gamma)}{2}\right] \tag{4.1}$$

where the variables are:

- $\frac{dE}{dx}$: Stopping power, rate of energy loss per unit path.
- K : Constant depending on the material.
- z : Charge of the incident particle.
- Z : Atomic number of the material.
- A : Atomic mass of the material.
- β : Velocity of the incident particle relative to the speed of light ($\beta = \frac{v}{c}$).
- γ : Lorentz factor of the incident particle ($\gamma = \frac{1}{\sqrt{1-\beta^2}}$).

- m_e : Rest mass of the electron.
- c : Speed of light in vacuum.
- $T_{\max}$: Maximum kinetic energy that can be transferred to atomic electrons.
- I : Mean excitation energy of the material.
- $\delta(\beta\gamma)$: Density effect correction, accounting for the polarization of the material by the incident particle.

The particle identification in the TPC is possible because particles lose energy differently depending on their charge and mass. At the same fixed velocity, the higher the charge of the ionizing particle is, the higher the energy loss. For instance, it is possible to distinguish $z = 1$ particles (like protons p, deuterons d, tritons t, kaons K, pions π, electrons e, and muons μ) from $z = 2$ (like helium-3 nuclei). Equally charged particles can be identified since they have different masses, thus different velocities β, and at the same fixed momentum, a more massive particle loses more energy than a lighter one: particle spectra are shifted with respect to each other, and electrons, muons, pions, kaons, protons, and deuteron spectra are distinguishable as in figure 4.6.
Due to the Bethe-Bloch shape, at high momenta ($p_T/|z| \sim 1$ GeV/c), the signal is overlapped for all the particles and the identification is no longer possible.
The TPC is an 88 m^3 cylindrical volume filled with a gas mixture of Ne-CO_2-N_2 (90-10-5). The TPC covers the pseudorapidity region $|\eta|$ <0.9 and full azimuth. The cathode divides its volume into two halves, while the two end plates are kept at a positive potential. When a charged particle crosses the volume, it ionizes the gas, producing electrons and positive ions that are quickly separated and drift in opposite directions inside the gas. During the drift to the anode, constantly accelerated electrons produce secondary ionization and electrons, then collected in the positive electrode. The end plates are radially subdivided into 18 azimuthal sectors, and each of them is segmented into an Inner ReadOut Chamber (IROC) and an Outer ReadOut Chamber (OROC), consisting of a total amount of 159 pads in each radial direction.
The upgrade of the TPC for Run 3 allows for a triggerless and continuous readout of all collision events. To reach this goal, the old readout system based on Multi Wire Proportional Chambers (MWPCs) was substituted with a new one based on Gaseous Electron Multipliers (GEMs).
Using MWPC, an active ion grid was necessary to collect ions, avoiding ion back-flow and space charge effects in the drift region. However, this technology could sustain a limited readout rate, leading to the use of GEMs.
GEMs [63] are gaseous detectors and allow for continuous readout at almost 100 times higher rate than using MWPC, significantly reducing the intrinsic dead time and ion back-flow imposed by an active ion-gating.

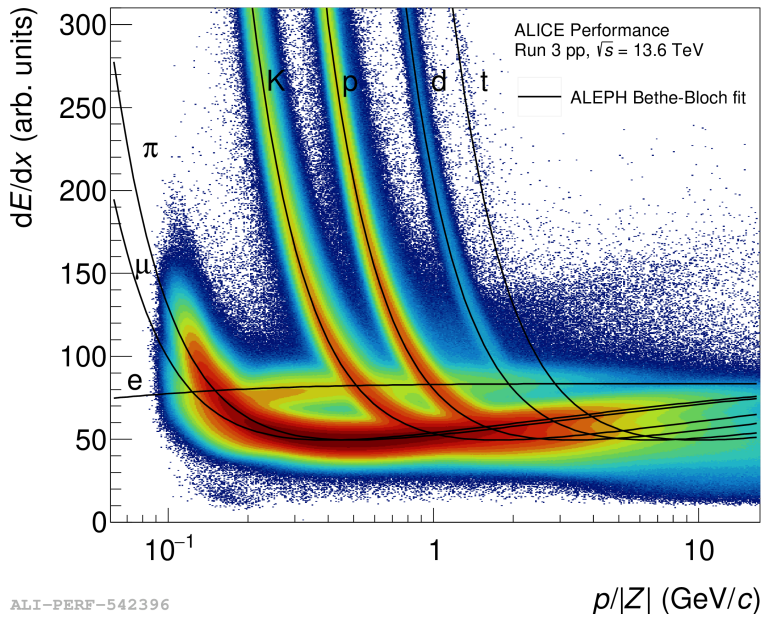

Figure 4.6: ALICE TPC dE/dx measured in pp collisions at $\sqrt{s} = 13.6$ TeV during Run 3. The energy loss of each particle species is fitted with ALEPH Bethe-Bloch parameterization [62], making the particle identification possible.

The new readout chambers used in the ALICE TPC are based on stacks of four GEM foils, as shown in figure 4.7. Each gap between foils is kept at a specific difference in voltage-producing transfer electric fields of 3500 V/cm in GEM1-GEM2 (E_{T1}) and GEM2-GEM3 (E_{T2}) gaps, while in GEM3-GEM4 it is of 100 V/cm (E_{T3}); the induced electric field between GEM4 and the pad plane is of 3500 V/cm. GEM foils have holes with alternating diameter sizes (standard holes of 140 μm and large holes of 280 μm), and the accidental alignment of holes in subsequent layers is avoided.
When the electron crosses the gas in the GEM, it produces ionization. The strong electric field accelerate secondary electrons to the anode producing an avalanche and the multiplication of the signal. While the electrons are drifted to the anode and the pad plane through the holes, positive ions are quickly collected by the near foil. In this way, the drift region is detached from the avalanche and readout ones, and the effective gain is increased.
With the new readout, the back-flow is intrinsically reduced to the 1%.
The new TPC has a resolution on the energy loss of 5-10%. It can also measure the momentum of the track by looking at the curvature in the magnetic field, with a resolution of the $\sim$ 1%. The TPC momentum resolution is shown in figure 4.8, where GEM and MWPC resolutions are compared.

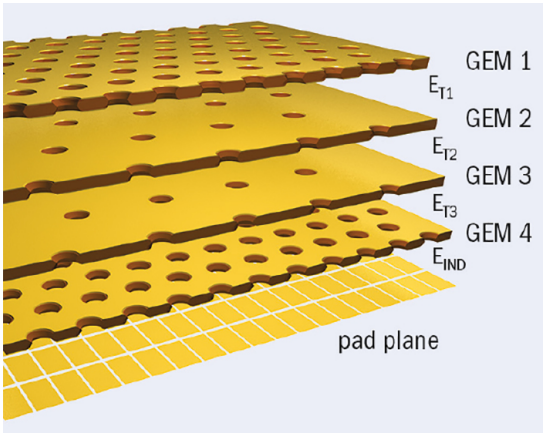

Figure 4.7: Four GEM foils used in TPC readout Chambers

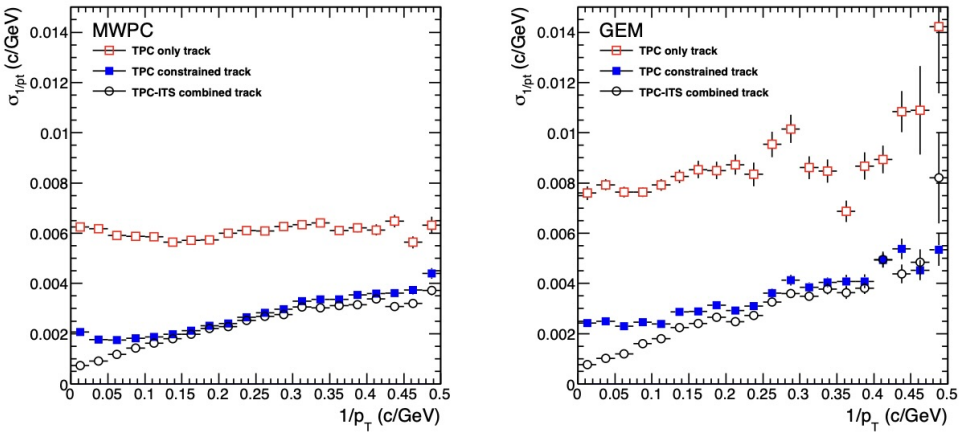

Figure 4.8: Momentum resolution as a function of $1/p_T$ measured in the ALICE TPC. The resolution obtained with the GEM (right panel) detectors used in Run 3 is compared to the resolution with MWPC (left panel) used in Run 2 [64].

4.3 Time of Flight

The Time of Flight (TOF) detector measures the time a particle takes to travel from the collision vertex to the detector layer, located at a distance of 3.7 m from the beam axis.
ALICE TOF is a cylindrical array of ~ 141 m^2 active area of Multi-gap Resistive Plane Chambers (MRPC) strip detectors with a 120×7.4 cm^2 active area, placed perpendicularly to the tracks and arranged to minimize the dead zone. The TOF, in figure 4.9, is organized into 18 azimuthal sectors, each one with ~ 90 MRPC, for a total amount of 1593 strips. To reduce the detector occupancy, each MRPC strip is segmented into 96 pads, with an area of 3.5×2.5 cm^2 each.
The readout is performed through 152928 channels.

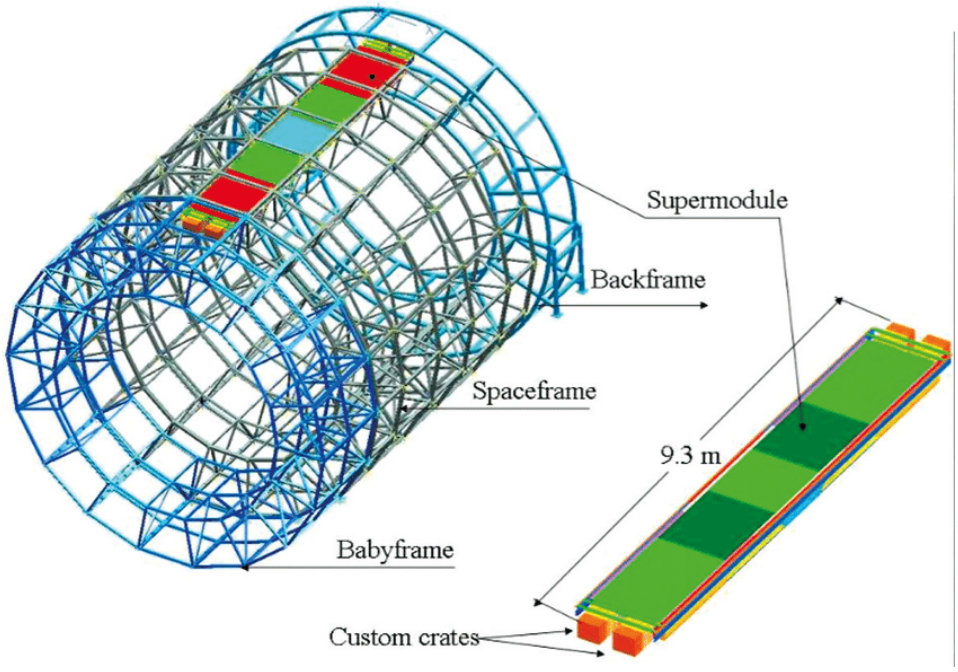

Figure 4.9: The Time of Flight detector in ALICE. It is divided into 18 azimuthal stacks [65].

MRPC are gaseous detectors formed by two resistive plates kept at high voltage difference, while the gap between them is filled with a gas and is subdivided into smaller gaps by floating voltage resistive plates. When the charged particle crosses the gas gap, it produces gas ionization, and the electron avalanche is created along the drift through the higher electric field region. The separation of the volume into five gaps with a width of 250 μm each produces five independent mini-avalanches, reducing the signal collection

time. The MRPCs reach an intrinsic time resolution $\sigma_{MRPC} = 50$ ps.
With this technology, the TOF can measure the time of flight with a global resolution σ_{TOF} resulting from:

$$\sigma_{TOF} = \sqrt{\sigma^2_{MRPC} + \sigma^2_{t_0} + \sigma^2_p + \sigma^2_{electronics}} \tag{4.2}$$

being σ_{t_0} the resolution on the collision time determined by the FIT detector, σ_p the resolution on the track momentum given by TPC, and $\sigma_{electronics}$ is due to read out electronics. The resolution is σ_{TOF} = 60-80 ps measured during calibration, which is shown in figure 4.10. For Run 3, the readout electronics of the TOF were upgraded to have continuous readout (chapter 3.8 in ref. [59]).

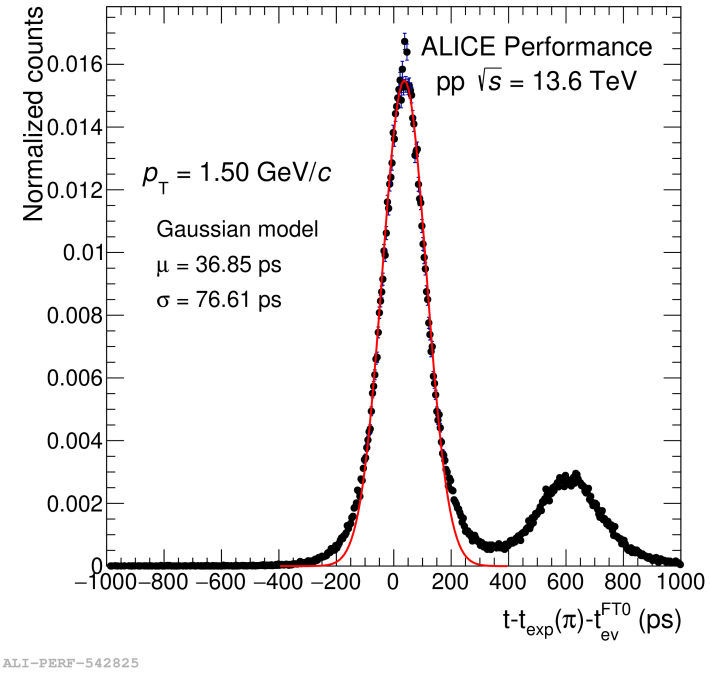

Figure 4.10: ALICE TOF resolution extracted under the pion hypothesis for particles with p_T 1.5 GeV/c in pp collisions at $\sqrt{s} = 13.6$ TeV during Run 3.

The TOF signal is used for particle identification: by measuring the time of flight Δt, it is possible to infer the mass m of the particle using the relation:

$$m = p\sqrt{\left(\frac{\Delta t}{l}\right)^2 - 1} \tag{4.3}$$

knowing the particle momentum p measured from the TPC and the track length l measured step by step along the track reconstruction procedure.

The particle identification is carried out in TOF because particles with different masses have different velocities β at the same momentum p; thus, the more massive the particle is, the greater the measured time of flight Δt is. Looking at the β measured by the TOF with respect to the momentum, in figure 4.11, electrons e, pions π, kaons K, protons p, and deuterons d are identified thanks to their mass difference. In figure 4.11, electrons e seem to have a super-luminal velocity due to calibration and resolution effects.

The particle mass is then inferred through equation 4.3, and the result is shown in

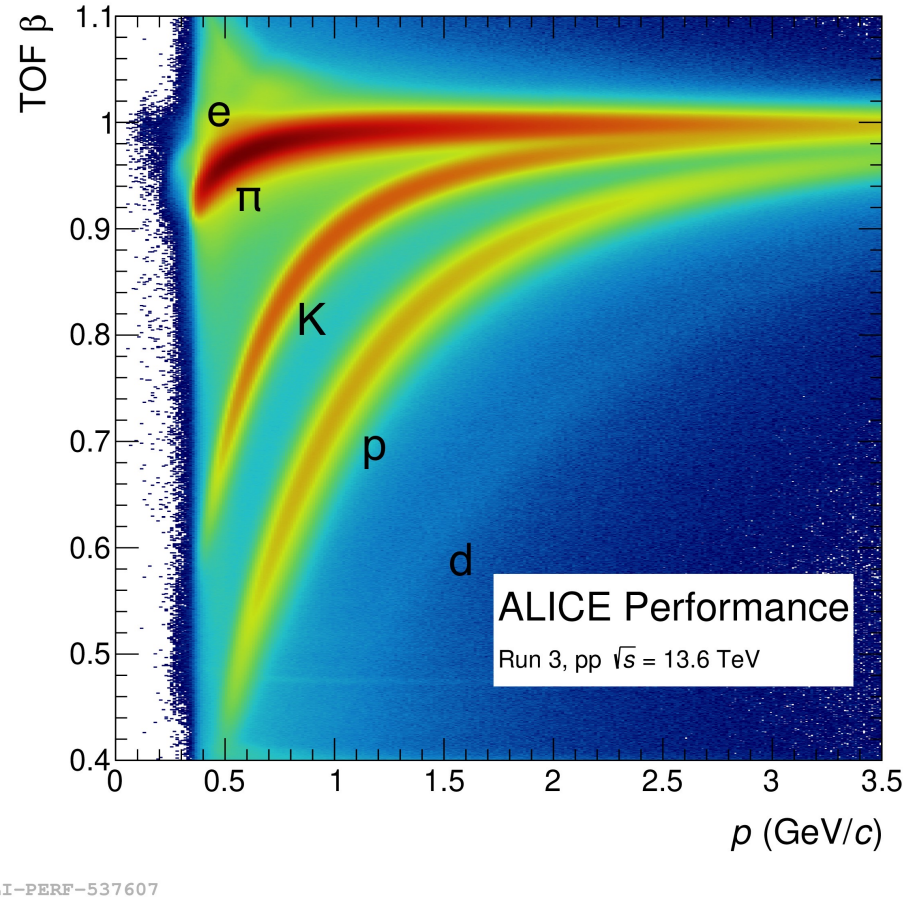

Figure 4.11: ALICE TOF Beta vs Momentum performance for pp collisions at $\sqrt{s}$ = 13.6 TeV during Run 3.

figure 4.12.

The ALICE TOF covers the full azimuth and the $|\eta| < 0.9$ region in pseudorapidity, but being far from the interaction point, only tracks with momentum $p \geq 0.3$ GeV/c can reach the TOF and only $\sim 60\%$ of protons produced in the primary collision vertex is seen by the TOF.

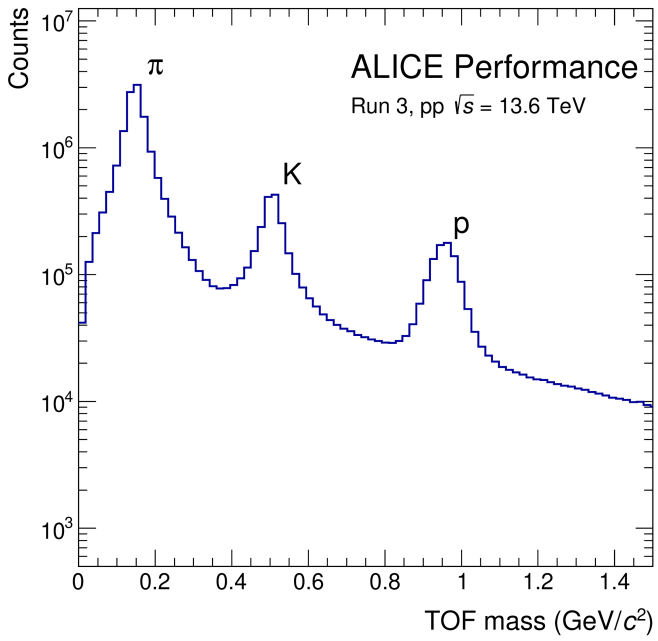

Figure 4.12: ALICE TOF mass measurement performance for pp collisions at $\sqrt{s} = 13.6$ TeV during Run 3.

Information from TPC and TOF are combined to carry out the particle identification in a wide range of momenta, up to several GeV/c. The fraction of tracks that gives a signal simultaneously in both the TPC and the TOF, over the total number of tracks producing a signal in TPC only, is called matching efficiency.
The greater particle identification power for the TOF is reached in the momentum range between 1 and 3 GeV/c. At very high momenta, all the particles are ultra-relativistic and have $\beta \sim 1$ becoming no longer distinguishable.

4.4 O^2: the new ALICE analysis framework for Run 3

As part of the Long Shutdown 2, a data acquisition and processing system was developed to achieve the goals for Run 3 and Run 4. The proposed measurements for Run 3 and 4 have a low signal-to-background ratio, which makes the triggering technique ineffective due to the large background. Instead, a trigger-less acquisition method and significant statistics would be required. During Run 3, the integrated luminosity is expected to be 200 pb^{-1} in pp collision [66], with in an interaction rate equal to 50 kHz in Pb-Pb collisions and 500 kHz in p-p collisions and producing a huge amount of data collected in continuous readout by the detector (1 TB/s in Pb-Pb collisions).

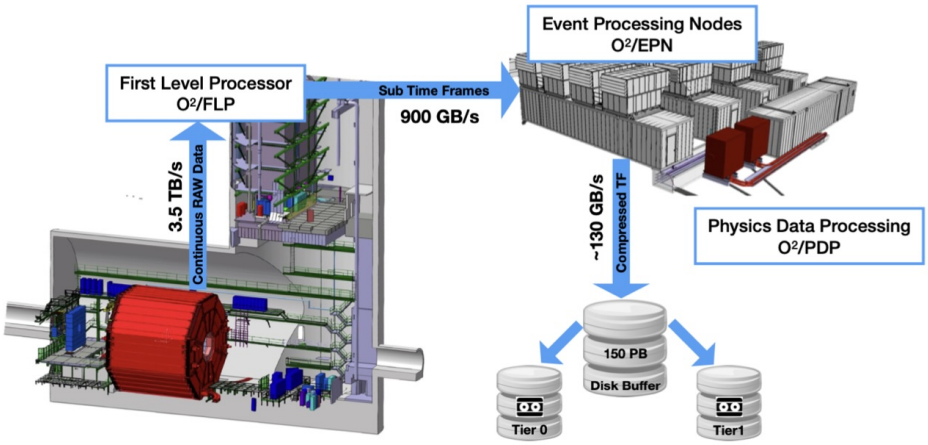

Figure 4.13: schematic view of the organization of the O^2 facility, from the raw data collected by the detector, the processing online and offline, until the storage [59].

Aside from hardware updates as explained in sections 4.3, 4.2 and 4.1, the continuous readout needs to minimize the cost and the requirements of the data processing and storage systems, implying the maximal reduction and compression of the data volume as early as possible during the data flow.
The innovative designed computing facility [67, 66] is called Online-Offline (O^2) (chapter 6 in [57]). It is a high throughput system organized in several reconstruction steps synchronously with the data tacking (online) and asynchronously (offline), as it is schematically shown in figure 4.13.

The online steps are performed by the First Level Processors (FLPs) and Event Processing Nodes (EPNs), respectively composed of 250 and 1500 computing nodes, each one with two 32-core CPUs and 8 GPUs.
The data flow is organized in Time Frames that are transferred from the detectors to the O^2 system via optical readout links and then multiplexed into the FPLs I/O system. FPL takes the raw data from optical links and partially compresses them by a factor of 2.5; data are merged and split into sub-Time Frames using an arbitrary reference clock. FLPs carry out a preliminary clusterization, masking, and calibration of data, and then the produced sub-Time Frames are buffered in memory and sent to EPN.
EPN performs the Time Frame aggregation, the event and track reconstruction for each detector using an early calibration. Data volume is fully compressed by a further factor 8, producing a 90 GB/s throughput to data storage (60 MB/s each EPN). Particular attention is given to TPC, which produces the greatest amount of data. For this reason, an online cluster finding and a first full fast-tracking are essential for TPC data compression. At the end of the synchronous stage, reconstructed data are stored in the Compressed Time Frame (CTF). The CTF consists of processed data from all active

detectors, temporarily stored to be ready for asynchronous reconstruction.
The calibration and matching are finalized in the asynchronous step, achieving the required data quality; then data are permanently stored locally using the finest global calibration (asynchronous pass, *apass*). A second type of reconstructed data is generated: the Analysis Object Data (AOD), which includes essential information on the reconstructed event, such as primary and secondary vertex reconstruction, track finding and fitting, tracks kinematic parameters, along with clusters and signal amplitudes from particle-counting detectors.
AOD files are available on the ALICE Grid and permanently stored on disks in the O^2 facility or Tier 0/1 data centers. Tier 0 and 1 take part in the asynchronous reconstruction: data are systematically re-calibrated, reprocessed, and re-filtered; then, the final AODs are sent to the Analysis Facility, where the analysis is run. Tiers can also perform Monte Carlo and detector simulations
Before starting a new data-taking period, the asynchronous processing of the data collected during the previous period - including calibration and re-reconstruction - must be completed. All CTF data will be removed from O^2 and Tier 1 disk buffers to make space for new data. Any unprocessed data will remain stored on tape until the next long shutdown, during which it can be reprocessed.
The storage facility acts as an interface between O^2 and the Grid.

Chapter 5

p−p and p−d correlation functions in pp collisions

The goal of this work is the measurement of the correlation function for (anti)proton and (anti)deuteron by using the femtoscopy technique discussed in chapter 3, with particular attention to the optimization of the particle identification technique for (anti)protons and (anti)deuterons, in preparation for the measurement on the full dataset of pp collisions in Run 3. The correlation function can be used to infer information about the particle emitting region, the source, and the type of interaction among the particles of interest.
The measurement of the correlation in momentum of proton-proton as well as proton-deuteron pairs is instrumental to understanding the formation mechanism of deuteron and helium-3 in hadronic collisions and in constraining the coalescence model (see chapter 1.3). Protons and deuterons interact through the strong and the Coulomb forces, and the interaction potential, built up from the fundamental QCD principles as discussed in section 2.2, is employed and validated in the correlation analysis.

The analysis discussed in this thesis is based on data collected with the ALICE detector in 2022 during the LHC Run 3 (see section 5.1.1). A key aspect of this measurement is the identification of protons and deuterons (and their corresponding antiparticles) with a high purity, combining the information from the TPC and the TOF, as discussed in section 5.1.3. The purity of the sample is crucial in femtoscopic analysis because the presence of contamination would produce distortions in the particle source, being the source size specific for each particle species, and in the correlation itself (see chapter 3). The tracks are selected according to criteria examined in section 5.1.2; the identified and selected tracks are coupled in pairs to compute the correlation functions for proton−proton and proton−deuteron, following the procedure explained in section 5.2. To perform the particle identification, the track selection and the pair production, a new algorithm is written inside the O^2 analysis framework (see section 4.4). The result, namely the proton−proton and proton−deuteron correlation functions are presented in

section 5.3. The proton−proton correlation is fitted with CATS to extract the source size, and results are discussed in comparison to existing measurements in pp collisions at 13 TeV ([68], see section 3.3) and 13 TeV at high multiplicity [54]. The proton−deuteron correlation function is instead discussed in relation to the recently published measurement in high multiplicity pp collision at $\sqrt{s} = 13$ TeV by ALICE [56].

5.1 Analysis details

5.1.1 Datasets

For the study presented in this thesis, I analyzed data from pp collisions at the collision energy $\sqrt{s} = 13.6$ TeV collected during Run 3 at LHC. I worked on a dataset consisting of more than 1.15 billion events collected at low interaction rate. The used sub-sample represents the 0.2% of the total collision sample collected in 2022, but the low interaction rate ensures a better reconstruction quality and calibration of the TPC, especially in relation to space charge distortions that mostly affect the tracking performance.
As ALICE operates in a triggerless continuous readout mode in Run 3, minimum bias pp collisions to be analysed are selected offline as discussed in section 4.
Because a deuteron is expected to be produced every 10^3 protons in pp collisions at the LHC [69], the signal of p−d pairs is rare. In order to cope with the large number of collisions to be inspected, the data are filtered in two steps to select the events of interest at the analysis level, to fasten the analysis and to optimize data storage. The initial data skimming is achieved by implementing pre-selection criteria on events and tracks. Stricter selection criteria are then applied on stored tracks to optimize and finalize the measurement of the correlation function.

5.1.2 Event and track pre-selection

To select events and tracks for this analysis I developed a new analysis algorithm, accepted as a new part of the official ALICE O^2 analysis framework. My algorithm performs the first skimming step on events and tracks over the full dataset.
Events are selected by requiring the coincidence of FT0-A and FT0-C signals and the coincidence of the measured collision time with the expected time of the bunch crossing. In addition, events are rejected if the position of the reconstructed primary vertex v_z along the beam axis is more distant than 15 cm from the nominal interaction point. In figure 5.1 the distribution of the primary vertex position v_z for the selected events is shown. After the first event selection, the sample employed in the analysis has 1153 million events.
Tracks are selected only if the traverse momentum is $0.4 < p_T < 5$ GeV/c.

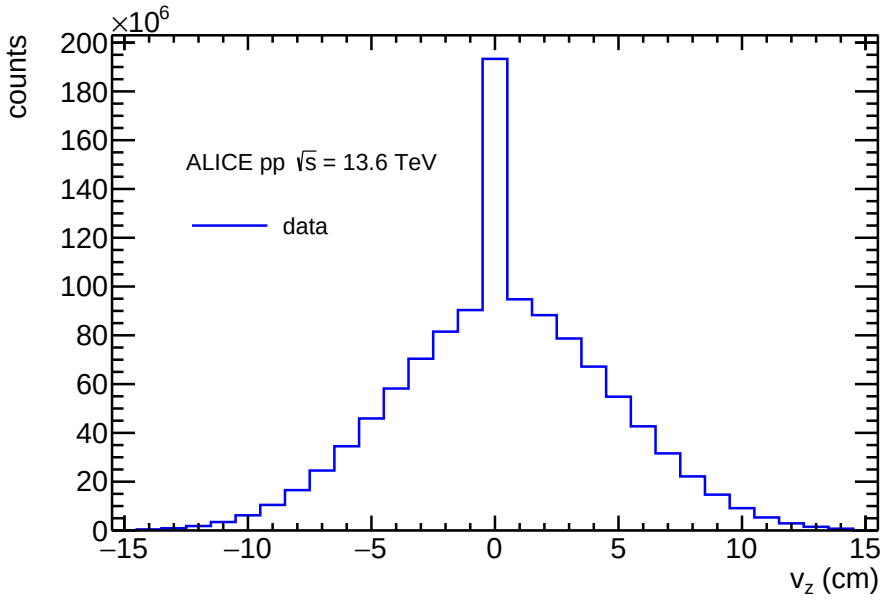

Figure 5.1: Position of the collision vertex v_z along the beam axis for each selected collision with respect to the interaction point. If v_z is greater than 15 cm the event is rejected.

The selection of tracks is based on the information of the ITS and the TPC. A cluster is defined when a charged particle crosses a detecting pad producing a signal that is associated to a track. Clusters are the starting point for the track reconstruction and therefore, the selection of well-reconstructed tracks for the analysis is based on the number of clusters associated with a track and the information on the goodness of that association. In this respect, only tracks with a χ^2 per number of clusters in the ITS smaller than than 36 and a χ^2 per number of clusters in the TPC smaller than than 4, are kept after the pre-filtering.
Moreover, tracks are selected using a variable called Distance of the Closest Approach (DCA_{xy}) in the transverse (xy) plane, which represents the projection on the transverse plane of the geometrical distance between the reconstructed track and the reconstructed collision point, called primary vertex. For the pre-filtering I require $|\mathrm{DCA}_{xy}| < 0.12$ cm, meaning that I selected mostly primary tracks that point the collision vertex while reducing contamination from secondary particles.

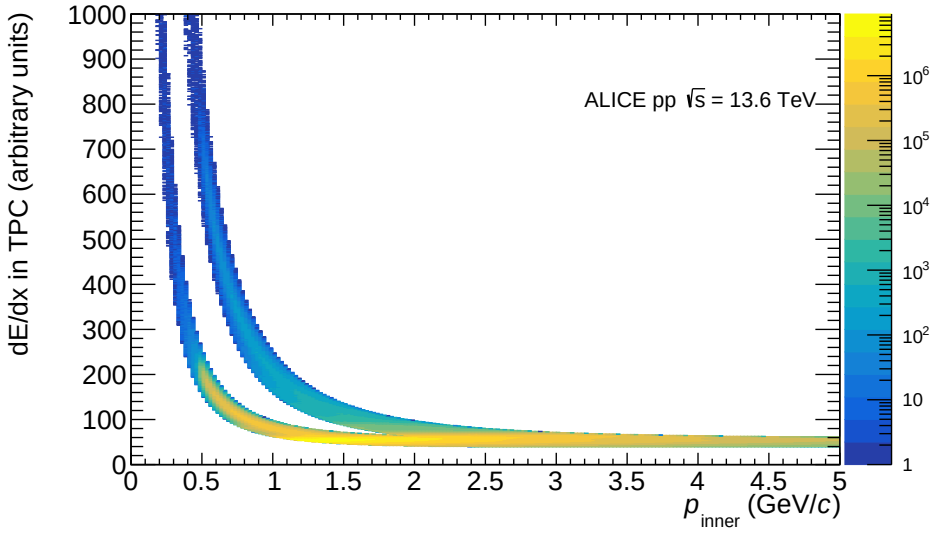

Figure 5.2: Energy loss in the TPC for selected tracks, identified as protons and deuterons within 4σ from the signal expected in the TPC for the selected particle species.

5.1.3 Proton and deuteron identification

To perform the particle identification (PID), a variable called n_σ, is used. It is defined as:

$$n_\sigma = \frac{X_{meas} - X_{exp,i}}{\sigma} \tag{5.1}$$

namely as the difference between the signal X_{meas} measured by the detector and the expected signal $X_{exp,i}$ for a given mass hypothesis with $i = p, d, e, K...$, over the expected resolution of the detector σ. This variable is defined for the TPC and the TOF, and, depending on the detector, the numerator is the difference of time of flights in the case of the TOF, and of energy losses in the case of the TPC. PID based on this variable considers that tracks that fall outside a given n_σ range are rejected because their probability to belong to the selected species is too low. In the pre-selection step, only tracks with $\left|n^{TPC}_{\sigma,p}\right|$ or $\left|n^{TPC}_{\sigma,d}\right|$ lower than 4 are stored. In the pre-selection no information from the TOF is used.
After the first selection, the sample employed in the analysis has 3.5 billions tracks associated to an (anti)proton or an (anti)deuteron. The energy loss in the TPC for the stored tracks is reported in figure 5.2. Comparing this result with the TPC signal in figure 4.6, the selected tracks are consistent with their identification as protons and deuterons.

The PID selection criteria aim at obtaining a sample of (anti)protons or (anti)deuterons

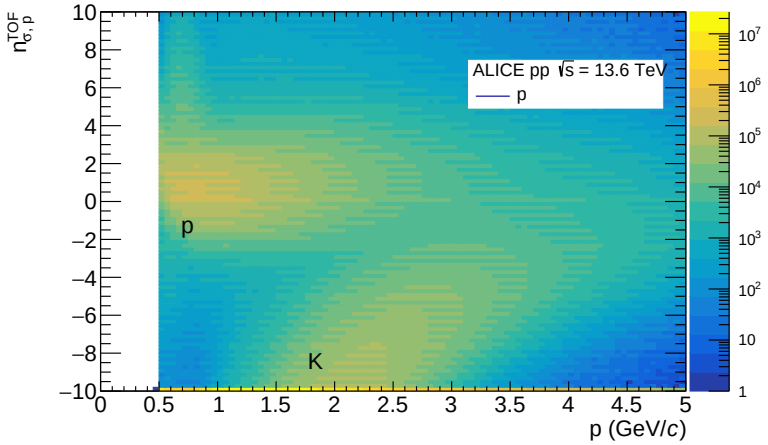

Figure 5.3: The $n_{\sigma,p}$ distribution as a function of momentum for the TOF and proton hypothesis. Similar distribution can be obtained for antiprotons.

as pure as possible and at avoiding the contamination, mainly due to the presence of kaons in the case of (anti)protons, or of (anti)protons in the case of (anti)deuterons, that smear the pure signal. Particles and antiparticles, with opposite electric charge, are distinguished depending on their bending inside the magnetic field. In the case of protons, the $n_{\sigma,p}^{TOF}$ before any PID selection is reported in figure 5.3. The signal from true protons is localized around the $n_{\sigma,p} = 0$. Figure 5.3 justifies also the choice to select tracks with momentum $p < 2.6$ GeV/c. Indeed, from high momentum tracks the contamination from kaons is larger and this signal is not distinguishable from the pure one. This behavior is due to the TOF detection principles and the distribution of the TOF signals in momentum (see figure 4.11). Similar plot is obtained also for antiprotons. A similar reasoning is also applied for the TPC and justifies the selection of tracks with $\left|n_{\sigma,p}^{TPC}\right| < 3$.
Based on the plots in figure 5.3, the TPC is used standalone for $p < 0.75$ GeV/c, while for higher momentum also the TOF is required. For protons, the track is selected only if $\left|n_{\sigma,p}^{TPC}\right| < 3$ and simultaneously -2.5 $< n_{\sigma,p}^{TOF} < 4$. For antiprotons, the track is selected only if $\left|n_{\sigma,p}^{TPC}\right| < 3$ and simultaneously $\left|n_{\sigma,p}^{TOF}\right| < 3$. The distribution in $n_{\sigma,p}^{TPC}$ and $n_{\sigma,p}^{TOF}$ and momentum p of selected tracks associated to protons or antiprotons is in figure 5.4.

To select the pure sample of (anti)deuterons the main issue is the contamination that comes mostly from (anti)protons. The distributions of deuteron and antideuteron tracks in $n_{\sigma,d}^{TOF}$ before any PID selection is reported in figure 5.5. To obtain an (anti)deuteron sample that is as pure as possible, particles identified as (anti)deuterons are rejected if also compatible with the (anti)proton hypothesis within 5σ in the TPC or in the TOF. Based on plots in figure 5.5, the TPC is used standalone up to $p_T = 1.3$ GeV/c, and only

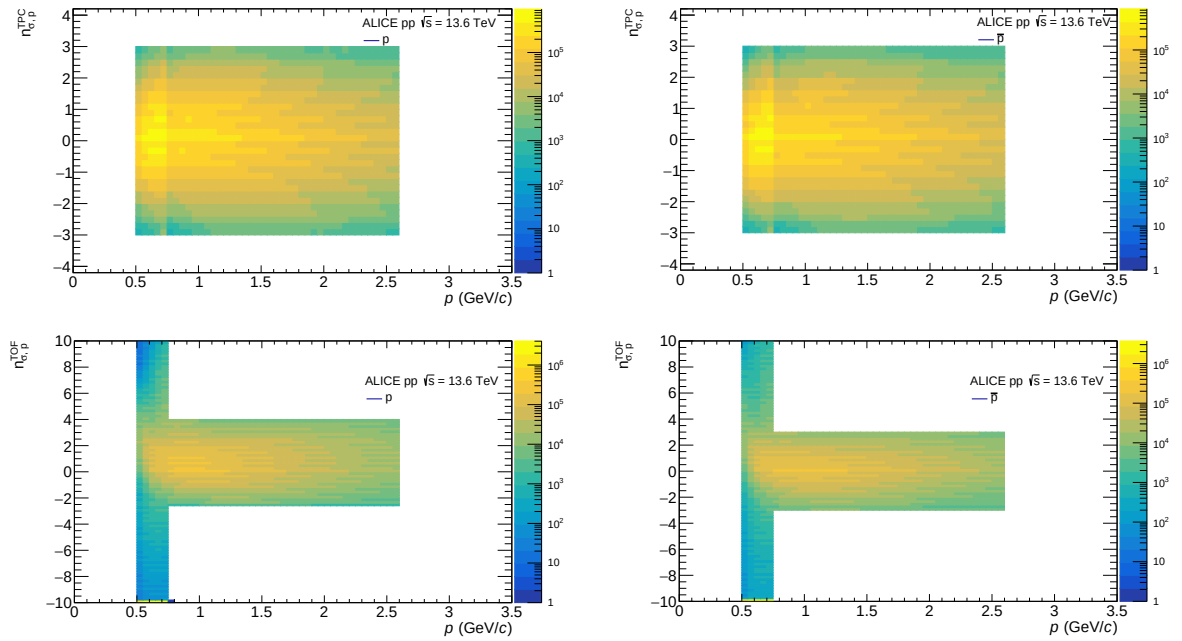

Figure 5.4: The $n_{\sigma,p}$ distribution for protons (left) and antiprotons (right) in the TPC (up) and the TOF (down). For p <0.75 GeV/c only positive tracks with -2.5 < $n_{\sigma,p}^{TPC}$ < 4 or negative tracks with $\left|n_{\sigma,p}^{TPC}\right|$ < 3 are selected; while for p >0.75 GeV/c only tracks with also $\left|n_{\sigma,p}^{TOF}\right|$ <3 are selected.

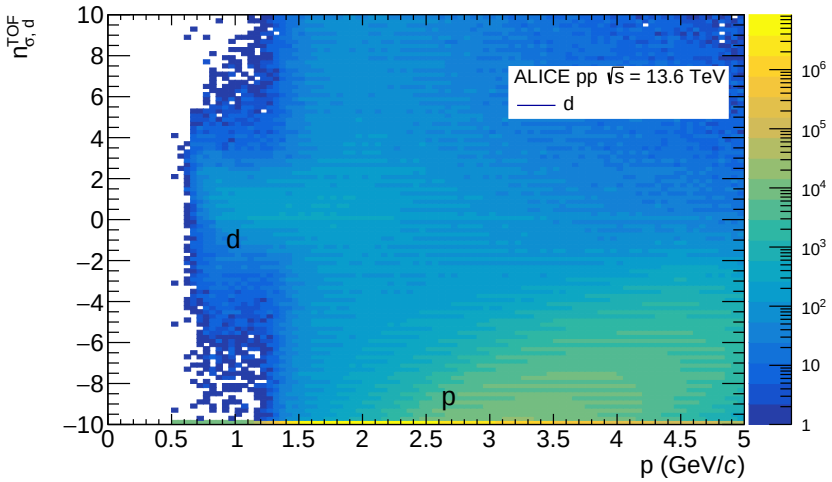

Figure 5.5: The $n_{\sigma,d}$ distribution as a function of momentum for the TOF and deuteron hypothesis. Similar distribution can be obtained for antideuterons.

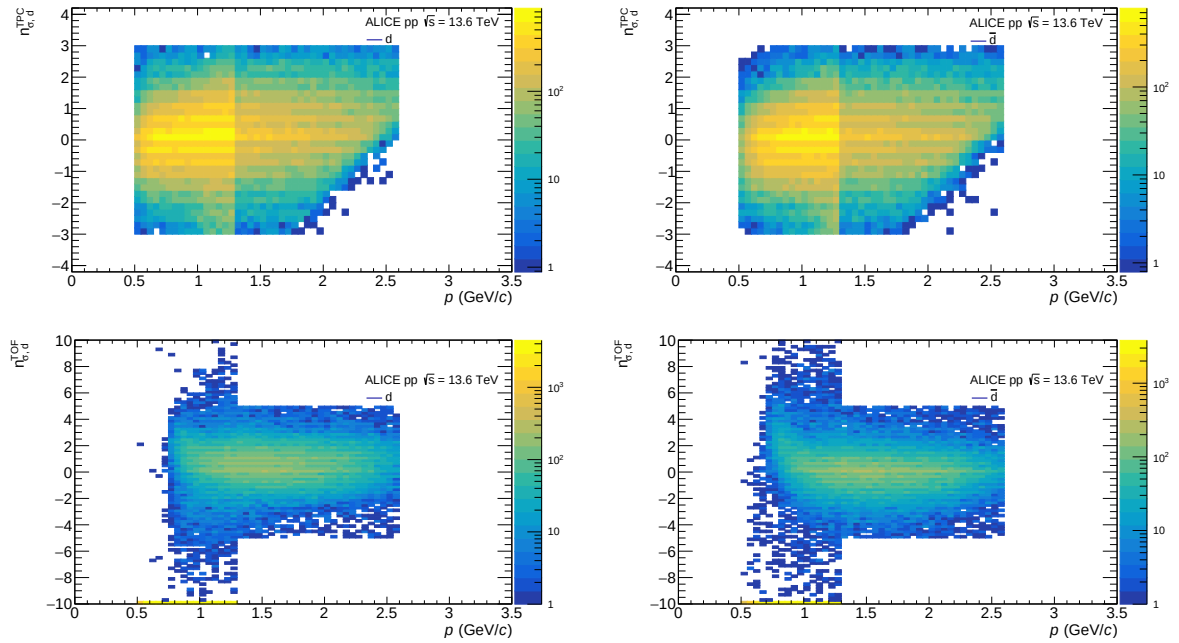

Figure 5.6: The $n_{\sigma,d}$ distribution for deuterons (left) and antideuterons (right) in the TPC (up) and the TOF (down). For $p < 1.3$ GeV/c only tracks with $\left|n_{\sigma,d}^{TPC}\right| < 3$ are selected; while for $p > 1.3$ GeV/c only tracks with also $\left|n_{\sigma,d}^{TOF}\right| < 5$ are selected.

tracks with $\left|n_{\sigma,d}^{TPC}\right| < 3$ are selected as (anti)deuterons. For particles with $p > 1.3$ GeV/c, the TPC and the TOF signals are combined and tracks are selected as (anti)deuterons if $\left|n_{\sigma,d}^{TPC}\right| < 3$ and $\left|n_{\sigma,d}^{TOF}\right| < 5$ simultaneously. The distribution in $n_{\sigma,d}^{TPC}$ and $n_{\sigma,d}^{TOF}$ of selected tracks associated to deuterons or antideuterons is in figure 5.6.

All the PID criteria applied for (anti)protons and (anti)deuterons are summarized in table 5.1.
In the selected sample there are 78.2 million protons and 66.3 million antiprotons over the total number of stored tracks. Instead, the deuteron sample is composed by 123446 deuterons, and 98597 antideuterons.
The lower abundance of antiparticles than particles is due to the presence of secondary protons and deuterons (hereafter called "secondaries") that are produced by knock-out reaction of primary particles hitting the detector material. Antiparticles cannot be produced by these reactions since the detector is made of matter, thus the antiparticle samples do not contain secondaries from material.
After applying these selection criteria, the resulting sample is pure enough to meet the goals of the preliminary analysis in this work.

	p	$\bar{\text{p}}$	d	$\bar{\text{d}}$
n_σ^{TPC}	$\left\|n_{\sigma,p}^{TPC}\right\| < 3$	$\left\|n_{\sigma,p}^{TPC}\right\| < 3$	$\left\|n_{\sigma,d}^{TPC}\right\| < 3$	$\left\|n_{\sigma,d}^{TPC}\right\| < 3$
$p_{threshold}$ (GeV/c)	0.75	0.75	1.3	1.3
n_σ^{TOF}	-2.5 $< n_{\sigma,p}^{TOF} <$ 4	$\left\|n_{\sigma,p}^{TOF}\right\| < 3$	$\left\|n_{\sigma,d}^{TOF}\right\| < 5$	$\left\|n_{\sigma,d}^{TOF}\right\| < 5$

Table 5.1: PID criteria for p, $\bar{\text{p}}$, d, and $\bar{\text{d}}$. For momentum $p > p_{threshold}$, the TPC and the TOF information are required simultaneously. Instead, for $p < p_{threshold}$ only the TPC is used.

5.1.4 Refined track selection

Track selection and PID have been adjusted for each particle species in order to maximise the number of selected tracks and minimize the contamination from different species in the analysed sample.
After the preliminary filters, the track selection is further refined and strict criteria are introduced. Tracks are selected inside the central pseudorapidity region $|\eta| < 0.8$ and the momentum p range is restricted from 0.5 GeV/c to 2.6 GeV/c, to avoid misidentified particles that smear the pure signal at high momentum.
The pseudorapidity range selected is below the acceptance range of the TPC, which extends up to $|\eta| < 0.9$. However, this specific range has been chosen to ensure a high matching efficiency between the TPC and the TOF, while avoiding any edge effects that may appear at the detector's acceptance limit of $|\eta| < 0.9$.
The DCA_{xy} and DCA_z are used to select primary tracks by applying the selection reported in table 5.2. For deuteron, the applied selection on DCA_{xy} is stricter than in the case of protons to exclude spurious signals that appeared only in the deuteron distribution at low momenta.
The TPC plays a crucial role in tracking, and the quality of the reconstruction procedure is quantified by the number of crossed TPC pad rows n_{crossed} and the number of findable TPC clusters n_{findable}. More precisely, a signal in a TPC pad row associated with a track is referred to as a cluster. However, due to the limited efficiency, not all the pad rows that are crossed by a track give a signal and, in general, the number of crossed pad rows is greater than the number of clusters. To obtain the correct number of crossed rows, a pad without a signal is added to the total number of cluster if its contiguous pad rows on both sides have recorded a signal. In general, the higher is the number of findable clusters and of crossed rows, the higher is the quality of track reconstruction. This is why tracks with a value of $n_{\text{crossed}}/n_{\text{findable}}$ lower than 0.83 are rejected.
A summary of all the track selection criteria is in table 5.2.

Figures 5.7 and 5.8 are the distributions in momentum p (left) and transverse momentum p_T (right) for (anti)protons and (anti)deuterons, respectively. The momentum

Selection criterion	Value
Pseudorapidity	$\|\eta\| < 0.8$
Momentum p (GeV/c)	$0.5 <$ p < 2.6
Number of findable TPC clusters	$n_{\text{findable}} > 90$
Number of crossed TPC pad rows	$n_{\text{crossed}} > 70$ (out of 159)
Crossed TPC rows / Findable TPC clusters	$n_{\text{crossed}}/n_{\text{findable}} > 0.83$
Distance of closest approach in the xy-plane	$\|\text{DCA}_{xy}\| < 0.12$ cm
	$\|\text{DCA}_{xy}\| < 0.012$ cm (for deuterons)
Distance of closest approach in the z-direction	$\|\text{DCA}_z\| < 0.12$ cm
	$\|\text{DCA}_z\| < 0.012$ cm (for deuterons)

Table 5.2: Track selection criteria used in the analysis.

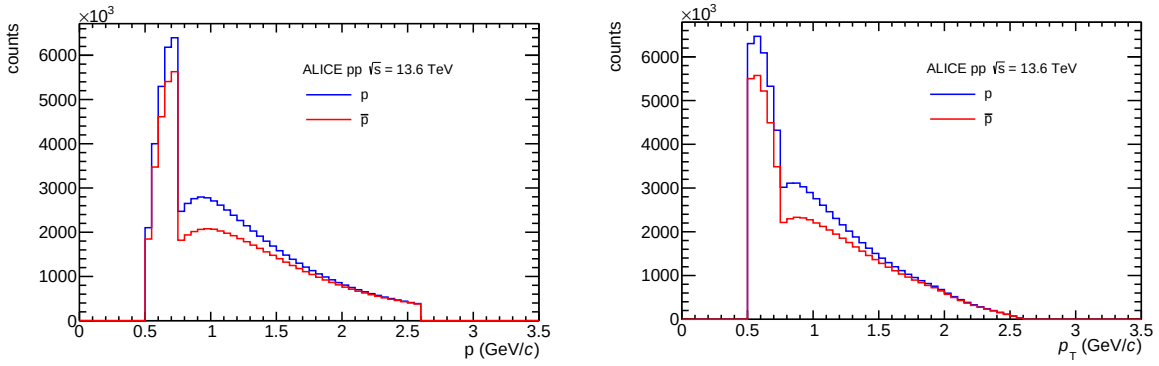

Figure 5.7: Momentum p (left) and transverse momentum p_T (right) distributions for selected tracks associated with protons (blue) and antiprotons (red).

of the track is measured in the ITS and the TPC, then the track is propagated to the TOF. As seen in the distributions in figure 5.7 and 5.8, the number of charged particles decreases as the momentum increases. This is because high energy particles are more weakly produced during the collision. A drop is visible both for p and p_T distributions at p= 0.75 GeV/c for (anti)protons and at p= 1.3 GeV/c for (anti)deuterons, because for higher p the combination of the TPC and the TOF signals is required in the selection.

In figure 5.9 and 5.10 the distributions of the particle pseudorapidity η (left) and of the azimuthal angular coordinate ϕ (right) for selected tracks associated to (anti)protons and (anti)deuterons, respectively, are shown. Both η and ϕ of the track are estimated at the vertex, then the track is propagated to the TOF. These distributions are useful to check dead zones in the TOF, correspondent to the dips in figure 5.9 or 5.10. Depending on the bending of the magnetic field particles and antiparticles hit the TOF differently and their distributions in ϕ are slightly shifted to each other. The η distribution exhibits

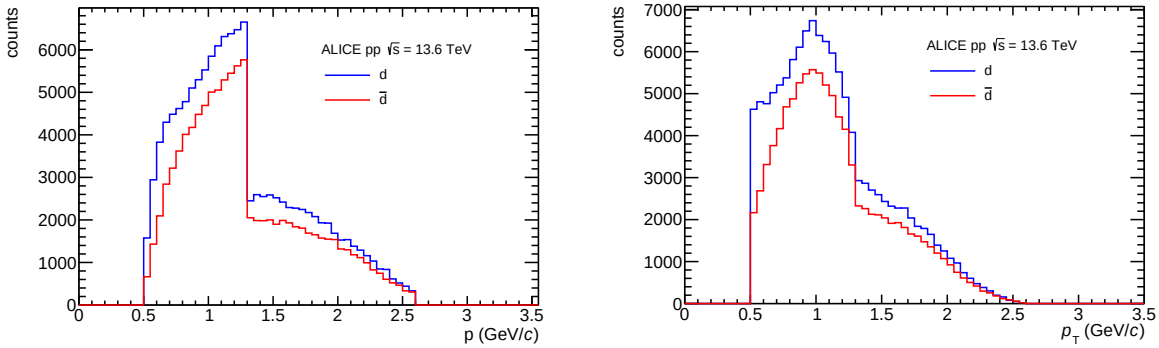

Figure 5.8: Momentum p (left) and transverse momentum p_T (right) distributions for selected tracks associated with deuterons (blue) and antideuterons (red).

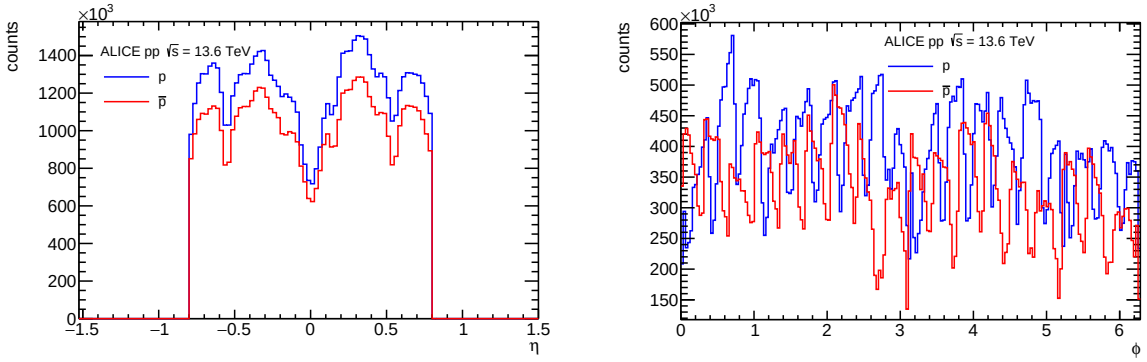

Figure 5.9: Pseudorapidity η (left) and azimuthal angle ϕ (right) distributions for selected tracks associated with protons and antiprotons.

a depression for $\eta = 0$, in correspondence to the cathode of the TPC. In principle, for an ideal detector, the two distributions should be symmetric with respect to zero, but their real behavior points out the asymmetry of the ALICE detector along the beam axis due to the operational conditions (dead zones, inefficient channels, tracking calibration, etc).

Tracks with $|DCA_{xy}| < 0.12$ cm are selected if associated with protons, antiprotons, or antideuterons. A stricter criterion is applied only for deuterons, selecting tracks with $|DCA_{xy}| < 0.012$ cm, to exclude secondaries. Antideuterons have a larger selection range in DCA_{xy} than deuterons because they cannot have secondary origin neither from primary particle decays, nor from material interactions. Similar criteria are applied to select tracks in $|DCA_z|$. The $|DCA_z| < 0.12$ cm is required for protons, antiprotons, and antideuterons, and $|DCA_z| < 0.012$ cm for deuteron only.

The distributions of DCA_{xy} and DCA_z for (anti)protons and (anti)deuterons are shown in figures 5.11 and 5.12, respectively. At low momentum, the presence of secondary par-

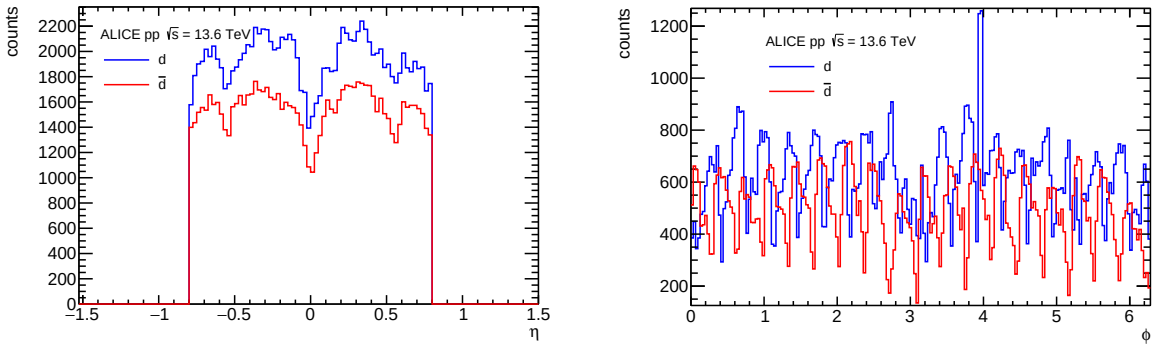

Figure 5.10: Pseudorapidity η (left) and azimuthal angle ϕ (right) distributions for selected tracks associated with deuterons and antideuterons.

ticles, with the production point distinguishable from the collision vertex and broader DCA_{xy}, is more abundant than at higher p, where the distribution of primary tracks is narrow.

5.2 The correlation function

The candidate (anti)protons and (anti)deuterons are employed to calculate the correlation function according to equation 3.8. Indeed, the distributions in relative momentum measured in the PRF k^* of track pairs obtained from the same event (SE(k^*)) and mixed events (ME(k^*)) are calculated as discussed in the following. Then the correlation function $C(k^*)$ is obtained as the normalized ratio of SE(k^*) over ME(k^*).
The track pairing is performed using a new algorithm developed inside the O^2 analysis framework for the purposes of this and other analyses within the ALICE Bologna group. The algorithm works with pairs of identical particles, like p−p or $\bar{\mathrm{p}} - \bar{\mathrm{p}}$, as well as non-identical particles, like p−d or $\bar{\mathrm{p}} - \bar{\mathrm{d}}$.
For each good track that has been identified according to track selection and particle identification (discussed in sections 5.1.3 and 5.1.4), the momentum p, the energy $E = \sqrt{p^2 + m^2}$, the pseudorapidity η, and the azimuthal angle ϕ are stored along with the collision index and the vertex position along the beam axis. Particles are then combined in pairs: to obtain the SE(k^*) distribution, tracks are paired if they have the same collision index, *i.e.*, they belong to the same event, while for the ME(k^*) distribution, each selected particle from one event is paired to each particle from any of the other events with similar multiplicity (for at maximum multiplicity difference of 50 tracks) and position of the vertex (for at maximum vertex position difference of 2 cm).

The correlation function is affected also by the track reconstruction performance: one

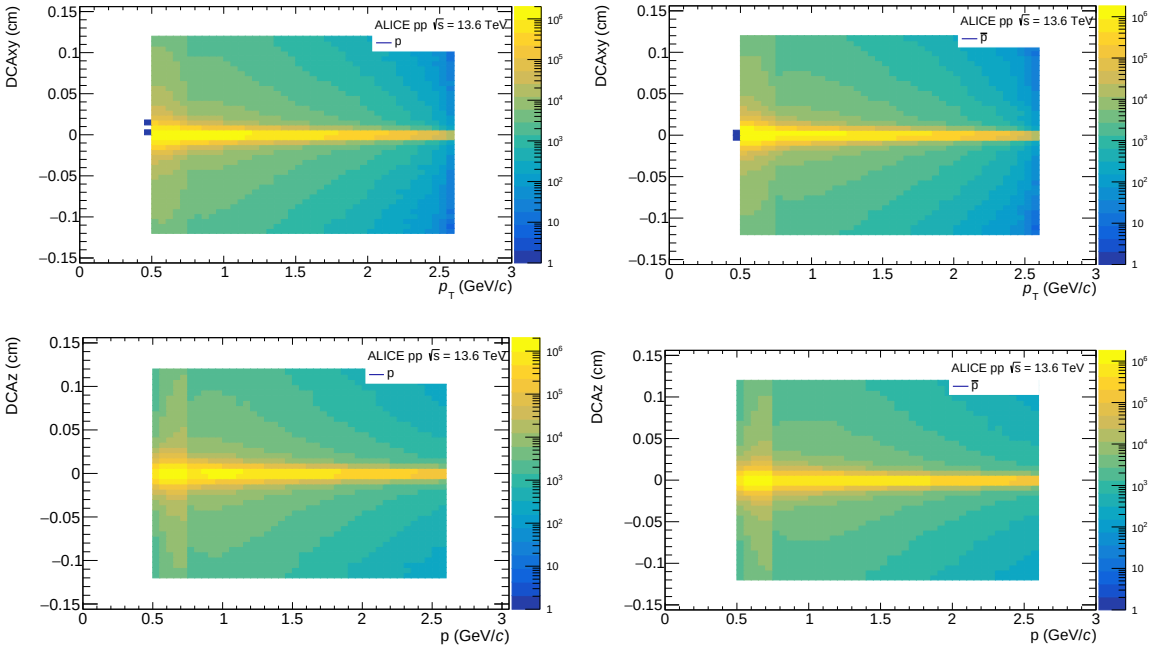

Figure 5.11: DCA_{xy} (up) and DCA_z(down) distributions for selected tracks associated with protons (left) and antiprotons (right).

track can be reconstructed as two — this effect is called "splitting", or two tracks could be reconstructed as one — this effect is called "merging". If one track is reconstructed as two, these two reconstructed tracks will be very close to each other in space with almost the same kinematic characteristics. This effect will lead more pairs in the low k^* region, and to an overestimation of the correlation function in that region. On the other hand, two tracks can be reconstructed as one if they are very close to each other with almost the same kinematic characteristics. In this case less pairs would be in the low k^* region, which will lead to an underestimation of the correlation function in that region. To avoid the splitting and the merging effects in the correlation function, close tracks are not used to build pairs. Two tracks are considered as close if:

$$\begin{aligned} \Delta\eta &= (\eta_1 - \eta_2) < 0.02 \\ \Delta\phi^* &= (\phi_1^* - \phi_2^*) < 0.02. \end{aligned} \tag{5.2}$$

The condition is expressed in terms of the difference in η ($\Delta\eta$) and in ϕ ($\Delta\phi^*$) between two tracks under consideration, labeled with indices 1 and 2. The star (*) in ϕ^* indicates that the azimuthal angle of the track is evaluated at the TPC radius fixed at 1.6 m. The track distribution in $\Delta\eta$ and $\Delta\phi^*$ is examined at three different TPC radii: 1.2 m, 1.4 m, 1.6 m and 1.8 m. The TPC radius that results in the least loss of tracks and effectively rejects splitting and merging effects is chosen.

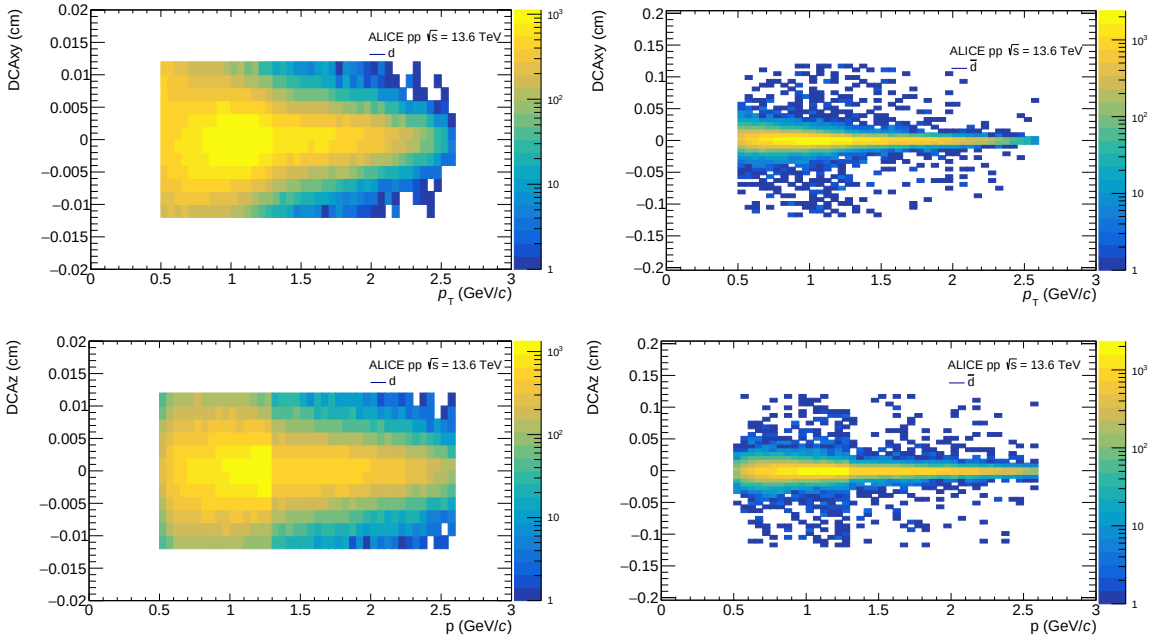

Figure 5.12: DCA_{xy} (up) and DCA_z(down) distributions for selected tracks associated with deuterons (left) and antideuterons (right).

	p−p	$\bar{p}-\bar{p}$	p−d	$\bar{p}-\bar{d}$
SE pairs	3871084	2914748	12187	7449
ME pairs	683.9 million	506.4 million	1149300	732796

Table 5.3: Same Event (SE) and Mixed Event (ME) number of pairs.

The relative momentum k^* of the pair is calculated from the energy-momentum four vectors of the tracks. Relativistic Lorentz transformations are applied on the four-momentum of the track using the ROOT::TMath::Boost class in ROOT. Then, the relativistic relative momentum k^* in the pair rest frame is evaluated as the difference between the two boosted four-momenta of the coupled tracks.
The SE(k^*) and ME(k^*) pairs distributions are shown in figure 5.13 for p−p and $\bar{p}-\bar{p}$. Figure 5.14 shows the SE(k^*) and ME(k^*) pairs distributions for p−d and $\bar{p}-\bar{d}$.
The number of obtained pairs of p−p, $\bar{p}-\bar{p}$, p−d, $\bar{p}-\bar{d}$ for SE and ME is in table 5.3.

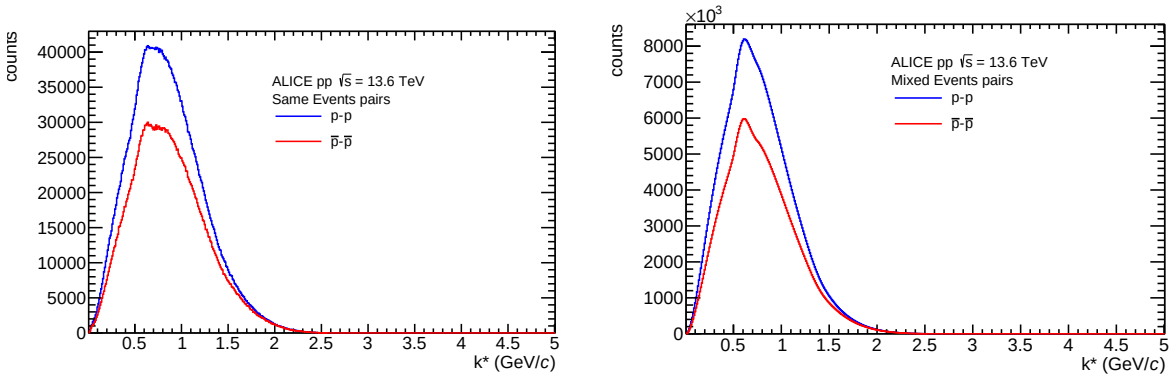

Figure 5.13: Pair relative momentum k^* distribution for pairs from the same event (right) and mixed event (left). The proton−proton pair distribution (blue) is compared with the antiproton−antiproton pair distribution (red).

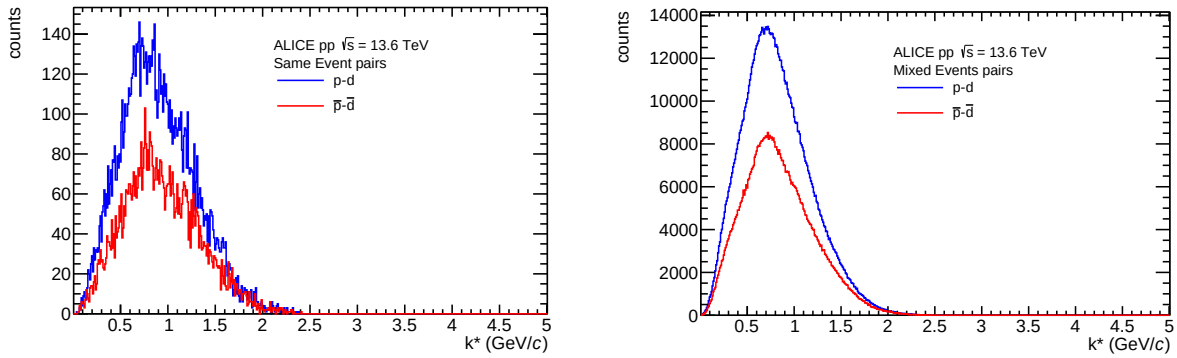

Figure 5.14: Pair relative momentum (k^*) distribution for pairs from the same event (right) and mixed event (left). The proton−deuteron pairs distribution (blue) is compared with the antiproton−antideuteron distribution (red).

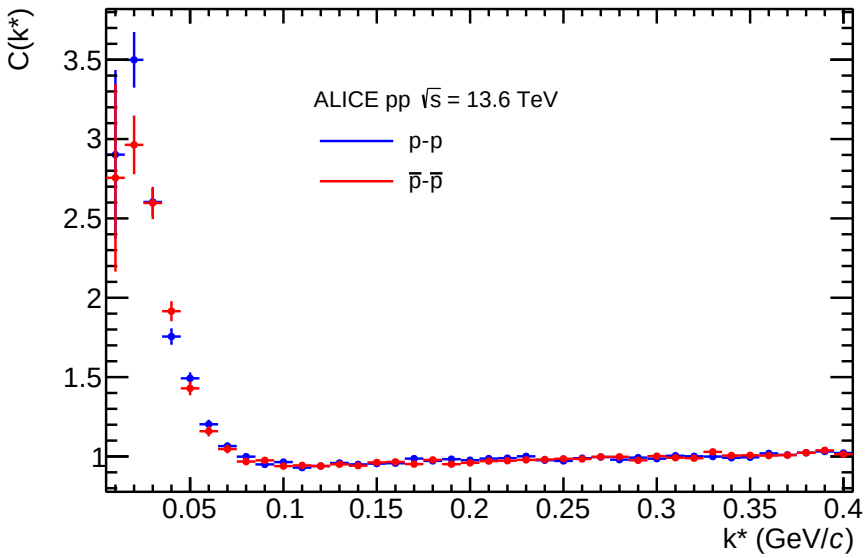

Figure 5.15: Correlation function for proton−proton pairs (blue) and antiproton−antiproton pairs (red) obtained from the normalized ratio of the same event and mixed event distributions (figure 5.13).

5.3 Results

5.3.1 p−p and $\bar{\text{p}} - \bar{\text{p}}$ correlation and source radius

The correlation function is obtained as the normalized ratio of SE(k^*) and ME(k^*), separately for p−p (positive charge correlation) and $\bar{\text{p}} - \bar{\text{p}}$ (negative charge correlation), and shown in figure 5.15. The correlation function is normalized by scaling it with the ratio between the integrals of the SE(k^*) and the ME(k^*) calculated in the range $0.2 < k^*(\text{GeV/c}) < 0.6$. This range falls outside the region where the femtoscopic signal is, correspondent to $k^* < 0.2$ GeV/c; therefore, the correlation function is expected to be flat in $0.2 < k^*(\text{GeV/c}) < 0.6$.
The obtained correlation functions for positive and negative charges are comparable, meaning that the interaction among particles is the same as among antiparticles, as expected from the strong interaction theory. This is also verified by comparing the ratio of the positive and negative charge correlations, resulting consistent with unity within the uncertainties up to very high momenta, as visible in figure 5.16.
The SE(k^*) for p−p and $\bar{\text{p}} - \bar{\text{p}}$ are added, as well as the ME(k^*), obtaining the total SE(k^*) and ME(k^*). The total correlation function is calculated by dividing the total SE(k^*) over the total ME(k^*). After the division, the correlation function is normalized by scaling it with the ratio between the integrals of the total SE(k^*) and ME(k^*) in the

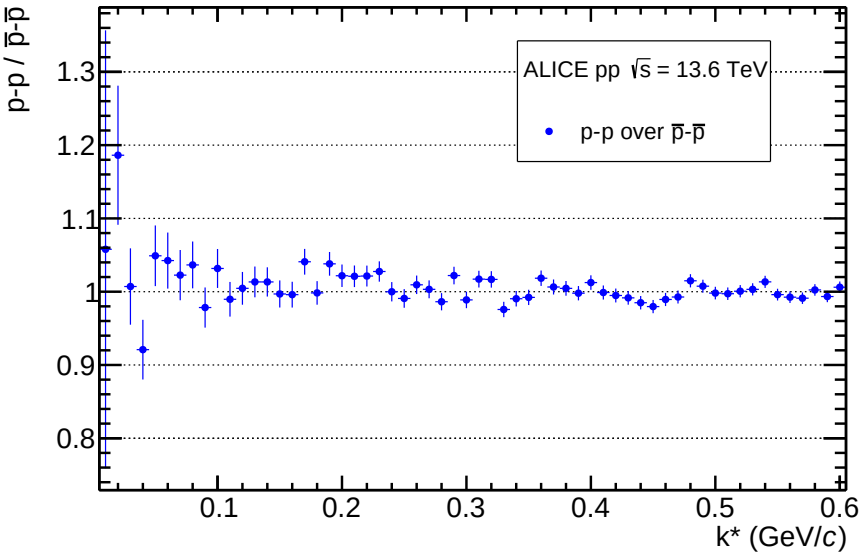

Figure 5.16: Ratio of proton−proton over antiproton−antiproton correlation functions shown in figure 5.15.

k^* range discussed above. The total correlation function is shown in figure 5.17 (black points).
The experimental total correlation function is fitted in the range $0 < k^*(GeV/c) < 0.2$ to the theoretical one, using the CATS framework (see section 3.3).
In the fit, the hypothesis of the one dimensional Gaussian source is assumed. The theoretical correlation function is numerically computed by CATS using the Argonne ν_{18} potential plus the Coulomb potential to describe the strong nucleon-nucleon interaction and the electromagnetic force.
In this fit, momentum resolution and purity corrections are not applied. These must be performed using Monte Carlo simulations, as it will be discussed in section 5.3.3.
As discussed in section 3.3, the fraction of genuine proton-proton pairs $\lambda_{genuine}$ in the experimental $C(k^*)$ (equation 3.10) is a fixed parameter in CATS. To take into account possible contamination due to feed-down particles, secondaries from the material, and misidentified particles, in this analysis $\lambda_{genuine}$ is fixed to 60%. This value results from the scanning over different values of $\lambda_{genuine}$ of the χ^2/ndf of the fit, and the $\lambda_{genuine}$ value that minimizes the χ^2/ndf is chosen. This value differs from the one used in the sample of pp collisions at $\sqrt{s} = 13$ TeV in Run 2 (figure 3.3), because here the corrections are not yet applied, contrary to the case of the Run 2 analysis.
The source radius extracted from the fit as a free parameter is

$$r_0 = 1.069 \pm 0.014 \text{ fm} \tag{5.3}$$

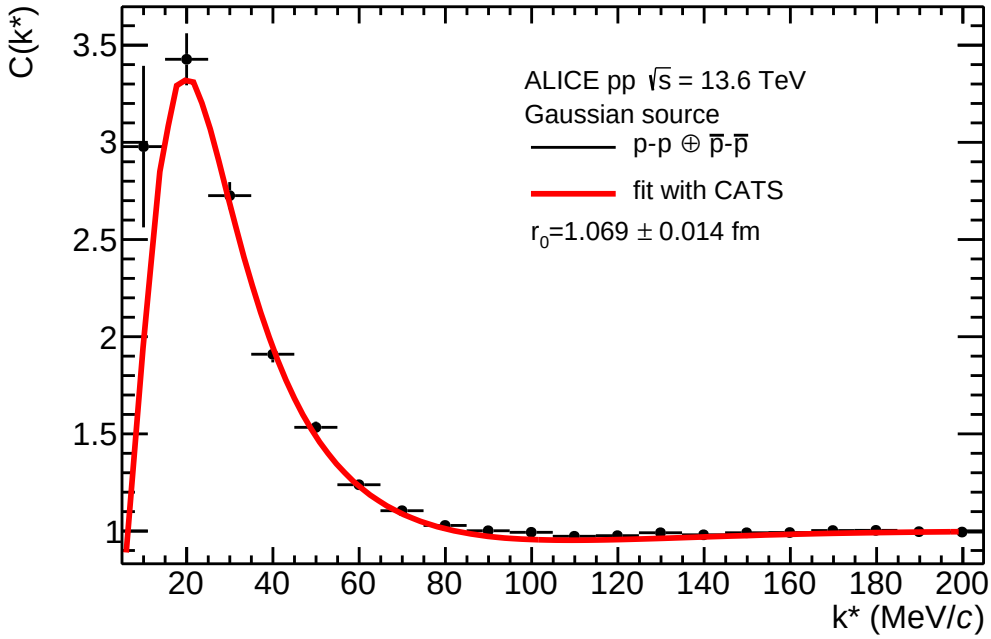

Figure 5.17: Correlation function for proton−proton and antiproton−antiproton extracted in pp collisions at $\sqrt{s} = 13.6$ TeV. The result is fitted using CATS (red line), assuming a one dimensional Gaussian source and using the Argonne ν_{18} plus the Coulomb potential to describe the proton−proton interaction. The source radius r_0, extracted as a fit parameter, is equal to 1.069 ± 0.014 fm.

with a $\chi^2/ndf = 50.78/19 = 2.67$. CATS uses a linear baseline to correct non-femtoscopic effects, but to increase the precision of the fit, a second order polynomial correction is applied, and then the corrected function is fitted with CATS using a flat baseline and fixing the slope a at 0 and the normalisation b at 1, usually both free fit parameters in CATS. It is to be noted that the choice of the baseline shape is arbitrary and thus is a potential source of systematic uncertainty.
The extracted source size is very close to the previous result obtained from the data sample of pp collisions at $\sqrt{s} = 13$ TeV, here shown in figure 3.3. However, the fraction of impurities included in the $\sqrt{s} = 13.6$ TeV sample, as well as the missing momentum resolution correction, strongly affects the final correlation function and the source size. Including more contamination (equivalent to fix the $\lambda_{genuine}$ to a lower value) the extracted source radius is bigger, and the peak in the correlation function is higher, as in the case of the correlation function in figure 5.17 with respect to that in figure 3.3.

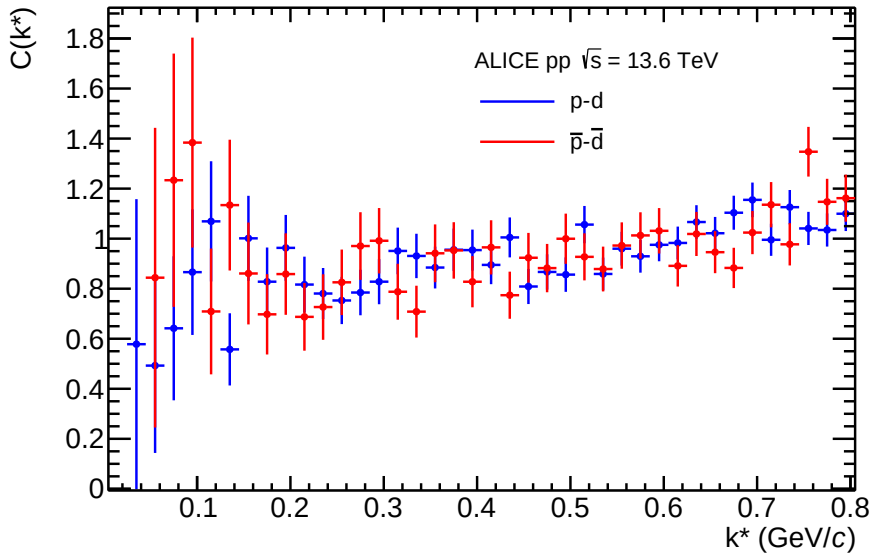

Figure 5.18: Correlation function for proton−deuteron pair (blue) and antiproton−antideuteron pair (red) obtained from the normalized ratio of the same event and mixed event distributions of pairs (figure 5.13). The uncertainties are larger than in figure 5.15, because of the lower number of pairs (see also table 5.3).

5.3.2 p−d and $\bar{\mathrm{p}} - \bar{\mathrm{d}}$ correlation

The proton−deuteron correlation function is obtained following a similar strategy as for the proton−proton case. Same event and mixed events distributions in figure 5.14 are divided and normalized in $0.4 < k^*(\mathrm{GeV}/c) < 0.8$ to compute the p−d (positive charge correlation) and $\bar{\mathrm{p}} - \bar{\mathrm{d}}$ (negative charge correlation) correlation functions, compared in figure 5.18.

The ratio of the positive (p−d) over the negative ($\bar{\mathrm{p}} - \bar{\mathrm{d}}$) charge correlations is in figure 5.19. Comparing this to the plot in figure 5.16, the uncertainties in this case are much bigger, but the ratio of positive and negative charge correlations is still consistent with unity within the uncertainties, even with large fluctuations.

The statistical uncertainties are essentially determined by the size of the deuteron sample, as deuteron is rarer than proton. To increase the deuteron sample, the analysis will be repeated in the future using the full sample of pp collisions at $\sqrt{s} = 13.6$ TeV. One could attempt using looser track and PID selections, though at the risk of reducing the purity of the sample. As the selections used in this preliminary analysis proved to be satisfactory, the preferred solution will be to increase the number of pp collisions analysed rather than modifying the selections.

This result, yet preliminary, represents the first attempt to measure the proton−deuteron

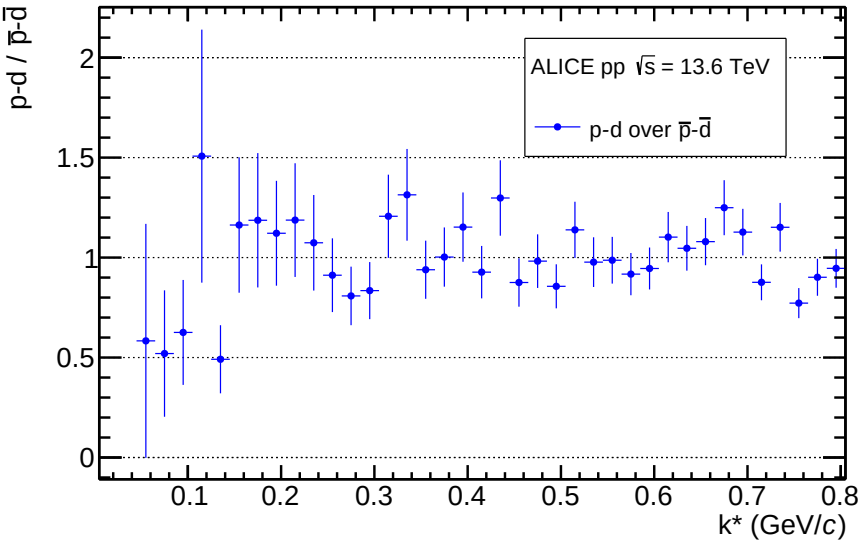

Figure 5.19: Ratio of proton−deuteron over antiproton−antideuteron correlation functions showed in figure 5.18.

correlation in minimum bias pp collisions at $\sqrt{s} = 13.6$ TeV. Summing the positive and the negative charge correlations in figure 5.18, the total proton−deuteron correlation function is obtained, as shown in figure 5.20.

The shape of the p−d correlation function measured in this analysis can be compared with the measurement performed in high multiplicity pp collisions at $\sqrt{s} = 13$ TeV in [56], reported in figure 5.21. It is worth also pointing out that whereas the genuine p−d interaction is expected to be the same in different collision systems and energies, the source is different. Measurements at different energies are required to extract information about the source.
In figure 5.21, the measured and theoretical correlation functions are compared. Differences between the model and the measured correlation function are expressed in term of number of standard deviations, in the lower panel of figure 5.21.
In [56], the proton−deuteron correlation is studied using different theoretical models for the interaction among particles in the pair, considering the nuclear interaction at work in the p-(np) system. This includes the Argonne ν_{18} two-nucleon potential plus the Urbana IX three-nucleon (NNN) [70] contribution and the Coulomb potentials. The most successful agreement of the theoretical correlation function with data is obtained when the p−d system is modeled as a three-body system, considering the total pair wave function (red curve). The correlation function is also calculated using a pionless EFT at NLO (pink curve). The blue curve, correspondent to the contribution of

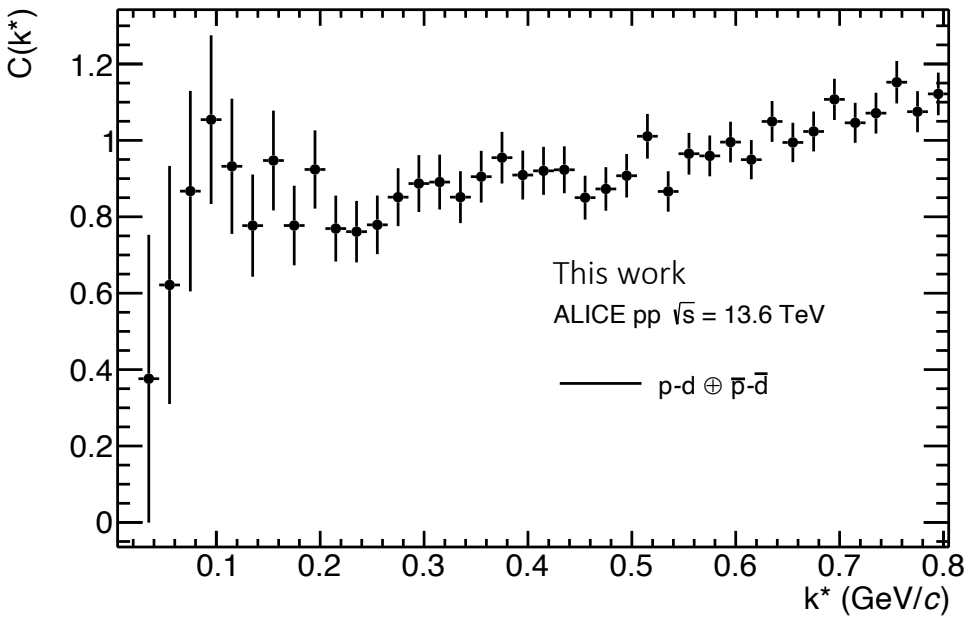

Figure 5.20: Total proton−deuteron experimental correlation function in pp collisions data at $\sqrt{s} = 13.6$ TeV.

the s-wave only, does not describe properly the experimental correlation function for $50 < k^*$ (MeV/c)< 150, while the pink curve is in good agreement with the experimental data only for $k^* < 100$ (MeV/c).

The fit of the p−d correlation function in figure 5.20 is beyond the scope of this work, as in order to extract the source radius for the p−d pair, a deeper investigation of the three-body interaction is required. In addition, prior to the fit several correction will be implemented as the next steps of the analysis.

5.3.3 Next steps: corrections

Comparing the experimental correlation measured with the $\sqrt{s} = 13.6$ TeV sample (figure 5.17) and the published result for p−p correlation with the $\sqrt{s} = 13$ TeV sample (figure 3.3), some corrections must be implemented in the final analysis to be consistent. To proceed like this Monte Carlo (MC) simulation must be used in the corrections. As Monte Carlo simulations that reproduce the realistic tracking and PID performance of ALICE in the data sample employed for the analysis have become available recently, this study will be performed as a next step for the analysis.

The measured correlation function is affected by detector effects smearing the real

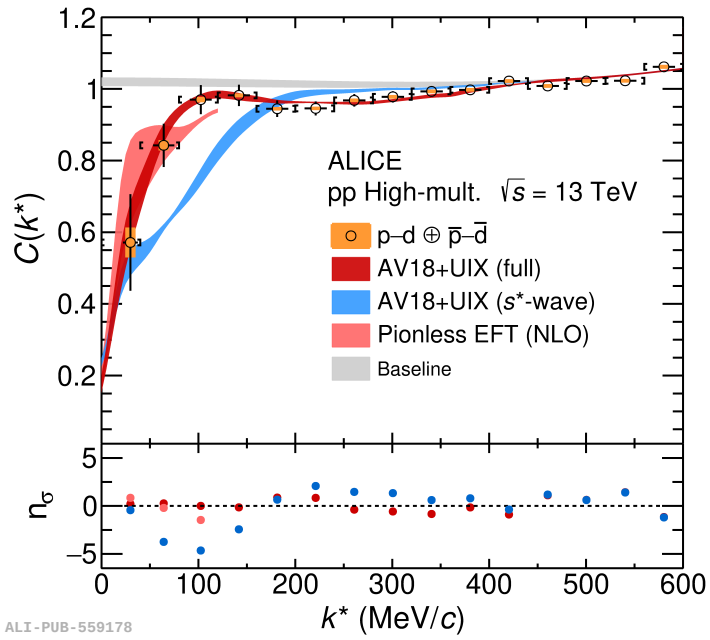

Figure 5.21: Proton deuteron correlation function measured by ALICE in high multiplicity pp collisions at $\sqrt{s} = 13$ TeV [56]. The experimental correlation is compared to the theoretical correlation functions using different potentials to model the three-body interaction. The lower panel shows the difference between the measured and calculated correlation functions in number of standard deviations.

particle momenta especially in the small k^* region. The experimental result must be re-scaled, correcting it in order to consider real detector effects and the limitation in resolution. To this end the correlation function and the detector effects must be simulated based on a simulated particle momenta distribution extracted from the MC. The corrected experimental correlation function with momentum resolution correction would have lower peak, and larger width with respect to the uncorrected one, so it should be closer to the previously published result.

Through MC simulation, the purity of the sample can be estimated (true particles/ true particles + misidentified). In the case of (anti)protons pair correlation, the (anti)particle of interest can be misidentified with kaons that smear the pure signal. The proton can ha secondary origin in the decay of Λ or Σ baryons, or in the material of the detector. The antiproton instead is produced by antibaryons decay (like $\bar{\Lambda}$) but not from the material. Even if the PID is accurate, the presence of misidentified smearing particle in the sample in not avoidable. The correction for purity means that the experimental uncorrected correlation function is related to the corrected one though the purity fraction. Being this corrective factor always lower than one, this correction would lower the correlation function points above the unity, and rise the points above the unity, thus the peak. No changes are expected in the non femtoscopic region.

In the case of proton−deuteron correlation, correction for momentum resolution and purity must be implemented following the same approach discussed for the proton−proton correlation. The purity correction aims at avoiding contamination in the sample due to the presence of secondaries produced in weak or strong decaying resonances, misidentified particles and secondaries produced in the material. The following contributions have to be included:

$$p{-}d = p{-}d{+}p_{\Lambda}{-}d{+}p_{\Sigma^+}{-}d{+}\tilde{p}{-}d{+}p{-}\tilde{d}{+}p_{\Lambda}{-}\tilde{d}{+}p_{\Sigma^+}{-}\tilde{d}{+}\tilde{p}{-}\tilde{d}{+}p_M{-}d{+}p_x{-}d_M \quad (5.4)$$

where p_{Λ} and p_{Σ^+} are (anti)protons produced in Λ or Σ baryon decays, $\tilde{p}$ and $\tilde{d}$ are misidentified (anti)particles and p_M, d_M are particles produced in the material. p_x can represent any kind of proton previously introduced. The deuteron cannot have a secondary origin from weak or strong decays due to its mass, but it can be produced in the detector material. The antideuteron cannot have secondary origin neither from primary particle decays, nor from material interactions.

5.3.4 Final remarks

The proton−proton and the proton−deuteron correlation functions are rather different. Both exhibit a drop at very low k^* due to the Coulomb repulsion among the positively charged particles in the pairs. Protons are fermions and they feel the Pauli blocking that imposes that two or more identical fermions can not be in the same quantum state. Thus, the proton−proton pair correlation function is described by the quantum statistical mechanics plus the Coulomb and strong interactions, resulting in a peak

for $k^* < 50$ MeV/c that drops to zero for $k^* \to 0$.
On the other hand, deuterons are bosons, and being non-identical particles, protons and deuterons can be in the same quantum state without any limitation from quantum statistical mechanics. The interaction among protons and deuterons is due to Coulomb and strong interactions.
Notably, the most recent studies presented in [56] indicate that the study of the p−d correlation can provide access to the genuine three-body interaction. The results obtained with the work presented in this thesis are therefore promising and set the basis for the measurement of the p−d correlation function using pp collision data from the ongoing LHC Run 3.

Conclusions

The work presented in this thesis is a preliminary analysis to measure proton−proton and proton−deuteron pair correlations in pp collisions at $\sqrt{s} = 13.6$ TeV using the ALICE detector at the LHC. To carry out the analysis, a new framework has been developed within the official analysis framework of ALICE. The new algorithm optimizes the particle identification of (anti)protons and (anti)deuterons and produces the coupling of the identified tracks into pairs.
As a result of the analysis, the experimental correlation functions of proton−proton and proton−deuteron have been obtained. The measured proton−proton correlation function was fitted using CATS, a dedicated software that solves numerically the Schrödinger equation for the particle pair starting from the choice of an appropriate interaction potential, which in this case was the Argonne ν_{18} potential plus a Coulomb interaction term. The fit of the theoretical correlation function to the measured one returned the radius of the proton source. The measured radius is $r_0 = 1.069 \pm 0.014$ fm, compatible within the uncertainties with the ALICE measurament in pp collisions at $\sqrt{s} = 13$ TeV. It is to be noted that the fit performed did not consider yet momentum resolution corrections, systematic uncertainties, and purity correction, which are based on Monte Carlo simulations and must be considered to improve the accuracy of the fit and the precision of the radius measurement. The proton−deuteron correlation function was measured with high uncertainties and statistical fluctuations because of the small deuteron sample in the analysed collision sample. However, the shape of the correlation is consistent with the very recently published proton−deuteron correlation obtained for $\sqrt{s} = 13$ TeV pp collisions.
Given the present statistical uncertainties, a fit to the correlation function for p−d is premature. In addition, such a fit would require a deeper theoretical understanding of the three-body interaction that is beyond the purposes of the work presented in this thesis.
The promising result of this work established the basis for extending this analysis to the entire pp dataset available from the ongoing LHC Run 3. Based on its good performance, the final analysis will employ the new framework developed in the scope of this thesis. Nevertheless, this work offered the opportunity to begin the implementation of the new analysis framework and to set the optimal selection criteria for the final analysis. All

the corrections not considered in this thesis because of time limitations would be fully included in the final analysis.
This work is part of the ERC-founded CosmicAntiNuclei project, which aims to validate coalescence models and predict the expected signal and background rates for dark matter light antinuclei by improving the current modeling of the formation mechanisms. To this end, the source radius obtained from the correlation analysis carried out in this work may be instrumental for modeling nucleosynthesis in high-energy interactions.

Acknowledgements

This work results from a journey that, over the last year, has immersed me in the heart of scientific research. In addition to being the conclusion of my life as a student at the University of Bologna, this thesis marks the beginning of my adventure as a researcher.

This result would not have been possible without the invaluable support and guidance of my supervisor, Professor Francesca Bellini. She introduced me to scientific research and guided my personal growth.

I would extend my sincere gratitude to all the researchers of the Alice Bologna group, who welcomed me into the group and taught me a lot in recent months.
In particular, I would like to thank Doctor Nicolò Jacazio for his precious assistance and emotional support throughout this journey.
A sincere thanks also goes to Doctor Neelima Arwaal, whose support was invaluable during the most challenging moments.
I am immensely grateful to my fellow doctoral students in the ALICE group, with whom I shared my days in the office. Special thanks are reserved for Gleb, my research partner, who shared this experience with me for almost a year and imparted invaluable insights from the initial stages to the final results.

My passion and curiosity for science and physics have accompanied me since childhood, when I browsed the great atlases of the sky, dreaming of the stars from the balcony of my house. For this, I have to thank my family for fueling my growing curiosity about the world and allowing me to explore, always encouraging me to strive for excellence.

Today, my life as a student draws to a close, but my greatest aspiration is to remain an eternal learner, and I am sure my future will be marked by continuous challenges. The last five years have been incredible but full of hard moments. I sincerely thank my friends who stood by me, unwavering in their support, enriching the time we spent together with their invaluable affection. Thank you to Liviana, Ludovica, Andrea, Vittorio, Mauro, Stefano, and Alessia.
Finally, but certainly not least, I want to express my deep appreciation to Andrea, who has never left and has always been able to offer me precious and concrete help in all phases of this not-easy journey.

Bibliography

[1] "Precision measurement of the mass difference between light nuclei and anti-nuclei," *Nature Physics*, vol. 11, no. 10, pp. 811–814, 2015.

[2] "Le redshift des nébuleuses extragalactiques," *Helvetica Physica Acta, Tome 6, p. 110-127*, vol. 6, pp. 110–127.

[3] F. Zwicky, "Republication of: The redshift of extragalactic nebulae," *General Relativity and Gravitation*, vol. 41, no. 1, pp. 207–224, 2009.

[4] E. Pécontal, T. Buchert, P. Di Stefano, Y. Copin, and K. Freese, "Review of observational evidence for Dark Matter in the universe and in upcoming searches for dark stars," *European Astronomical Society Publications Series*, vol. 36, pp. 113–126, 2009.

[5] M. Roos, "Dark Matter: The evidence from astronomy, astrophysics and cosmology," *arXiv preprint arXiv:1001.0316*, 2010.

[6] V. C. Rubin, "The rotation of spiral galaxies," *Science*, vol. 220, no. 4604, pp. 1339–1344, 1983.

[7] M. Bartelmann, "Gravitational lensing," *Classical and Quantum Gravity*, vol. 27, no. 23, p. 233001, 2010.

[8] D. Clowe, M. Bradač, A. H. Gonzalez, M. Markevitch, S. W. Randall, C. Jones, and D. Zaritsky, "A direct empirical proof of the existence of dark matter," *The Astrophysical Journal*, vol. 648, no. 2, p. L109, 2006.

[9] NASA, "NASA finds direct proof of Dark Matter," retrieved on August 21, 2006. [Online]. Available: https://www.nasa.gov/mission_pages/chandra/multimedia/photos06-096.html

[10] S. Giagu, "WIMP dark matter searches with the ATLAS detector at the LHC," *Frontiers in Physics*, vol. 7, 05 2019.

[11] N. Topchiev, A. Galper, V. Bonvicini, I. Arkhangelskaja, A. Arkhangelskiy, A. Bakaldin, S. Bobkov, O. Dalkarov, A. Egorov, Y. V. Gusakov *et al.*, "High-energy gamma-ray studying with GAMMA-400," *arXiv preprint arXiv:1707.04882*, 2017.

[12] N. Fornengo, L. Maccione, and A. Vittino, "Dark matter searches with cosmic antideuterons: status and perspectives," *Journal of Cosmology and Astroparticle Physics*, vol. 2013, no. 09, p. 031, 2013.

[13] M. Aguilar, L. A. Cavasonza, G. Ambrosi, L. Arruda, N. Attig, F. Barao, L. Barrin, A. Bartoloni, S. Başeğmez-du Pree, J. Bates *et al.*, "The Alpha Magnetic Spectrometer (AMS) on the international space station: Part II—Results from the first seven years," *Physics reports*, vol. 894, pp. 1–116, 2021.

[14] D. Hooper, I. Cholis, T. Linden, and K. Fang, "HAWC observations strongly favor pulsar interpretations of the cosmic-ray positron excess," *Physical Review D*, vol. 96, no. 10, p. 103013, 2017.

[15] A. Oliva. (2023) Search for anti-nuclei with AMS-02. EMMI2023. Bologna. [Online]. Available: https://indico.gsi.de/event/15762/contributions/69261/attachments/42627/59510/EMMI2023%20-%20Search%20for%20anti-nuclei%20with%20AMS-02%20-%20A.%20Oliva.pdf

[16] J. Cooley, T. Lin, W. H. Lippincott, T. R. Slatyer, T.-T. Yu, D. S. Akerib, T. Aramaki, D. Baxter, T. Bringmann, R. Bunker *et al.*, "Report of the topical group on particle dark matter for Snowmass 2021," *arXiv preprint arXiv:2209.07426*, 2022.

[17] J. Beatty, A. Nelson, A. Olinto, G. Sinnis, A. Abeysekara, L. Anchordoqui, T. Aramaki, J. Belz, J. Buckley, K. Byrum *et al.*, "Snowmass Cosmic Frontiers 6 (CF6) working group summary–The Bright Side of the Cosmic Frontier: Cosmic probes of fundamental physics," *arXiv preprint arXiv:1310.5662*, 2013.

[18] L. Šerkšnytė *et al.*, "Reevaluation of the cosmic antideuteron flux from cosmic-ray interactions and from exotic sources," *Phys. Rev. D*, vol. 105, no. 8, p. 083021, 2022.

[19] D. Maurin, R. Taillet, F. Donato, P. Salati, A. Barrau, and G. Boudoul, "Galactic cosmic ray nuclei as a tool for astroparticle physics," 12 2002.

[20] P. Von Doetinchem, K. Perez, T. Aramaki, S. Baker, S. Barwick, R. Bird, M. Boezio, S. Boggs, M. Cui, A. Datta *et al.*, "Cosmic-ray antinuclei as messengers of new physics: status and outlook for the new decade," *Journal of cosmology and astroparticle physics*, vol. 2020, no. 08, p. 035, 2020.

[21] C. Pinto, "Light (anti)nuclei production in high-energy nuclear collisions at the LHC with ALICE," 2020.

[22] F. Bellini and A. P. Kalweit, "Testing coalescence and statistical-thermal production scenarios for (anti-)(hyper-) nuclei and exotic QCD objects at energies available at the CERN Large Hadron Collider," *arXiv preprint arXiv:1807.05894*, 2018.

[23] N. Sharma, J. Cleymans, B. Hippolyte, and M. Paradza, "Comparison of p−p, p−Pb, and Pb−Pb collisions in the thermal model: Multiplicity dependence of thermal parameters," *Physical Review C*, vol. 99, no. 4, p. 044914, 2019.

[24] A. Andronic, P. Braun-Munzinger, K. Redlich, and J. Stachel, "Decoding the phase structure of QCD via particle production at high energy," *Nature*, vol. 561, no. 7723, pp. 321–330, 2018.

[25] A. Andronic and P. Braun-Munzinger, "Hadron yields in central nucleus-nucleus collisions, the statistical hadronization model and the QCD phase diagram," in *Criticality in QCD and the Hadron Resonance Gas*, 1 2021.

[26] R. Scheibl and U. Heinz, "Coalescence and flow in ultrarelativistic heavy ion collisions," *Physical Review C*, vol. 59, no. 3, p. 1585, 1999.

[27] S. Acharya, J. Adam, D. Adamová, J. Adolfsson, M. M. Aggarwal, G. A. Rinella, M. Agnello, N. Agrawal, Z. Ahammed, N. Ahmad *et al.*, "Production of deuterons, tritons, ^{3}He nuclei, and their antinuclei in pp collisions at $\sqrt{s}$= 0.9, 2.76, and 7 TeV," *Physical review C*, vol. 97, no. 2, p. 024615, 2018.

[28] ALICE Collaboration, "The ALICE experiment-A journey through QCD," *arXiv preprint arXiv:2211.04384*, 2022.

[29] L. P. Csernai and J. I. Kapusta, "Entropy and Cluster Production in Nuclear Collisions," *Phys. Rept.*, vol. 131, pp. 223–318, 1986.

[30] F. Bellini and A. Kalweit, "Testing production scenarios for (anti-)(hyper-) nuclei with multiplicity-dependent measurements at the LHC," *arXiv preprint arXiv:1907.06868*, 2019.

[31] K. Blum and M. Takimoto, "Nuclear coalescence from correlation functions," *Physical Review C*, vol. 99, no. 4, p. 044913, 2019.

[32] F. Bellini, K. Blum, A. P. Kalweit, and M. Puccio, "Examination of coalescence as the origin of nuclei in hadronic collisions," *Physical Review C*, vol. 103, no. 1, p. 014907, 2021.

[33] ALICE Collaboration, "Two-pion Bose-Einstein correlations in *pp* collisions at $\sqrt{s}$ = 900 GeV," *Phys. Rev. D, hep-ex 1007.0516, 10.1103/PhysRevD.82.052001*, vol. 82, p. 052001, 2010.

[34] J. Adam *et al.*, "Centrality dependence of pion freeze-out radii in Pb-Pb collisions at $\sqrt{s}_{NN}$ = 2.76 TeV," *Phys. Rev. C*, vol. 93, no. 2, p. 024905, 2016.

[35] G. Ecker, "Quantum chromodynamics," *2005 European School of High-Energy Physics, e-print hep-ph/0604165*, 4 2006.

[36] F. Wilczek, "Nobel Lecture: Asymptotic freedom: From paradox to paradigm," *Reviews of Modern Physics*, vol. 77, no. 3, p. 857, 2005.

[37] G. Chapline and M. Nauenberg, "Asymptotic freedom and the baryon-quark phase transition," *American Physical Society, Phys. Rev. D, 10.1103/PhysRevD.16.450*, vol. 16, pp. 450–456, Jul 1977.

[38] S. Bethke, "World summary of α_s (2011)," *Nuclear Physics B-Proceedings Supplements*, vol. 222, pp. 94–100, 2012.

[39] K. S. Krane, *Introductory nuclear physics*. John Wiley & Sons, 1991.

[40] S. Aoki and T. Doi, "Lattice qcd and baryon-baryon interactions: Hal qcd method," *Frontiers in Physics*, vol. 8, p. 307, 2020.

[41] T. Inoue and the HAL QCD Collaboration, "Baryon Interactions from QCD on Lattice," *Few Body Syst.*, vol. 62, no. 4, p. 106, 2021.

[42] HAL QCD Collaboration, N. Ishii, S. Aoki, T. Doi, T. Hatsuda, Y. Ikeda, T. Inoue, K. Murano, H. Nemura, and K. Sasaki, "Hadron–hadron interactions from imaginary-time Nambu–Bethe–Salpeter wave function on the lattice," *Phys. Lett. B*, vol. 712, pp. 437–441, 2012.

[43] R. Machleidt and D. R. Entem, "Chiral effective field theory and nuclear forces," *Physics Reports*, vol. 503, no. 1, pp. 1–75, 2011.

[44] D. R. Entem, R. Machleidt, and Y. Nosyk, "High-quality two-nucleon potentials up to fifth order of the chiral expansion," *Phys. Rev. C*, vol. 96, no. 2, p. 024004, 2017.

[45] E. Epelbaum, "Few-nucleon forces and systems in chiral effective field theory," *Progress in Particle and Nuclear Physics, Elsevier*, vol. 57, no. 2, pp. 654–741, 2006.

[46] R. B. Wiringa, V. G. J. Stoks, and R. Schiavilla, "Accurate nucleon-nucleon potential with charge-independence breaking," *Phys. Rev. C*, vol. 51, pp. 38–51, Jan 1995.

[47] R. H. Brown and R. Q. Twiss, "LXXIV. a new type of interferometer for use in radio astronomy," *The London, Edinburgh, and Dublin Philosophical Magazine and Journal of Science*, vol. 45, no. 366, pp. 663–682, 1954.

[48] D. L. Mihaylov, "Analysis techniques for femtoscopy and correlation studies in small collision systems and their applications to the investigation of proton-lambda and lambda-lambda interactions with ALICE," Ph.D. dissertation, Technische Universität München, 2021.

[49] M. A. Lisa, S. Pratt, R. Soltz, and U. Wiedemann, "Femtoscopy in relativistic heavy ion collisions: two decades of progress," *Annu. Rev. Nucl. Part. Sci.*, vol. 55, pp. 357–402, 2005.

[50] L. Fabbietti, V. M. Sarti, and O. V. Doce, "Study of the strong interaction among hadrons with correlations at the LHC," *Annual Review of Nuclear and Particle Science*, vol. 71, pp. 377–402, 2021.

[51] S. Acharya, D. Adamová, J. Adolfsson, M. M. Aggarwal, G. A. Rinella, M. Agnello, N. Agrawal, Z. Ahammed, S. U. Ahn, S. Aiola *et al.*, "p−p, p−Λ, and Λ − Λ correlations studied via femtoscopy in pp reactions at $\sqrt{s}$= 7 TeV," *Physical review C*, vol. 99, no. 2, p. 024001, 2019.

[52] R. Lednicky and V. L. Lyuboshits, "Final State Interaction Effect on Pairing Correlations Between Particles with Small Relative Momenta," *Yad. Fiz.*, vol. 35, pp. 1316–1330, 1981.

[53] R. Lednickỳ, "Finite-size effect on two-particle production in continuous and discrete spectrum," *Physics of Particles and Nuclei*, vol. 40, pp. 307–352, 2009.

[54] S. Acharya, D. Adamová, A. Adler, J. Adolfsson, M. M. Aggarwal, G. A. Rinella, M. Agnello, N. Agrawal, Z. Ahammed, S. Ahmad *et al.*, "Search for a common baryon source in high-multiplicity pp collisions at the LHC," *Physics Letters B*, vol. 811, p. 135849, 2020.

[55] D. Mihaylov, V. Mantovani Sarti, O. Arnold, L. Fabbietti, B. Hohlweger, and A. Mathis, "A femtoscopic correlation analysis tool using the Schrödinger equation (CATS)," *The European Physical Journal C*, vol. 78, no. 5, p. 394, 2018.

[56] S. Acharya *et al.*, "Exploring the strong interaction of three-body systems at the LHC," *CERN-EP-2023-181, arXiv:2308.16120 nucl-ex*, 8 2023.

[57] K. Aamodt, A. A. Quintana, R. Achenbach, S. Acounis, D. Adamová, C. Adler, M. Aggarwal, F. Agnese, G. A. Rinella, Z. Ahammed *et al.*, "The ALICE experiment at the CERN LHC," *Journal of Instrumentation*, vol. 3, no. 08, p. S08002, 2008.

[58] B. Abelev, Alice Collaboration *et al.*, "Upgrade of the ALICE experiment: letter of intent," *Journal of Physics G: Nuclear and Particle Physics*, vol. 41, no. 8, p. 087001, 2014.

[59] "ALICE upgrades during the LHC Long Shutdown 2," *arXiv:2302.01238, CERN-EP-2023-009, physics.ins-det*, 2 2023.

[60] I. Ravasenga, "Commissioning and performance of the new ALICE Inner Tracking System in the first phase of LHC Run 3," *arXiv preprint arXiv:2302.00432*, 2023.

[61] R. Münzer, ALICE Collaboration *et al.*, "Upgrade of the ALICE Time Projection Chamber," *Nuclear Instruments and Methods in Physics Research Section A: Accelerators, Spectrometers, Detectors and Associated Equipment*, vol. 958, p. 162058, 2020.

[62] W. Yu, "Particle identification of the ALICE TPC via dE/dx," *Nucl. Instrum. Meth. A*, vol. 706, pp. 55–58, 2013.

[63] F. Sauli, "The gas electron multiplier (GEM): Operating principles and applications," *Nuclear Instruments and Methods in Physics Research Section A: Accelerators, Spectrometers, Detectors and Associated Equipment*, vol. 805, pp. 2–24, 2016.

[64] L. Molnar, for the ALICE Collaboration *et al.*, "Upgrade and physics perspective of ALICE at the LHC," in *Journal of Physics: Conference Series*, vol. 589, no. 1. IOP Publishing, 2015, p. 012014.

[65] ALICE Collaboration, J. Adam, D. Adamová, M. Aggarwal, G. Aglieri Rinella, M. Agnello, N. Agrawal, Z. Ahammed, S. Ahmad, S. Ahn *et al.*, "Determination of the event collision time with the ALICE detector at the LHC," *The European physical journal plus*, vol. 132, pp. 1–17, 2017.

[66] ALICE Collaboration, "Future high-energy pp programme with ALICE," *ALICE-PUBLIC-2020-005, CERN-LHCC-2020-018, LHCC-G-179*, 2020.

[67] P. Buncic, M. Krzewicki, and P. Vande Vyvre, "Technical Design Report for the Upgrade of the Online-Offline Computing System," *CERN-LHCC-2015-006, ALICE-TDR-019*, 4 2015.

[68] ALICE Collaboration, "Study of the Λ-Λ interaction with femtoscopy correlations in pp and p-Pb collisions at the LHC," *CERN-EP-2019-096, arXiv:1905.07209 nucl-ex*, vol. 797, p. 134822, 2019.

[69] S. Acharya *et al.*, "Production of deuterons, tritons, ^{3}He nuclei and their antinuclei in pp collisions at $\sqrt{s} = 0.9$, 2.76 and 7 TeV," *Phys. Rev. C*, vol. 97, no. 2, p. 024615, 2018.

[70] J. Carlson, V. Pandharipande, and R. B. Wiringa, "Three-nucleon interaction in 3-, 4-and-body systems," *Nuclear Physics A*, vol. 401, no. 1, pp. 59–85, 1983.